E.O. Paton Electric Welding Institute of the National Academy of Science of Ukraine
International Association «Welding»

The Paton Welding Journal

01
2024

International Scientific-Technical and Production Journal ◊ Founded in January 2000 (12 Issues Per Year)

Address of Editorial Board
E.O. Paton Electric Welding Institute, 11 Kazymyr Malevych Str., 03150, Kyiv, Ukraine
Tel./Fax: (38044) 205 23 90, E-mail: journal@paton.kiev.ua, patonpublishinghouse@gmail.com
https://patonpublishinghouse.com/eng/journals/tpwj

State Registration Certificate 24933-14873 ПР from 13.08.2021
ISSN 0957-798X, DOI: http://dx.doi.org/10.37434/tpwj

Subscriptions, 12 issues per year:
$384 — annual subscription for the printed (hard copy) version, air postage and packaging included;
$312 — annual subscription for the electronic version (sending issues in pdf format or providing access to IP addresses).

Representative Office of «The Paton Welding Journal» in China:
China-Ukraine Institute of Welding, Guangdong Academy of Sciences
Address: Room 210, No. 363 Changxing Road, Tianhe, Guangzhou, 510650, China.
Zhang Yupeng, Tel: +86-20-61086791, E-mail: patonjournal@gwi.gd.cn

The content of the Journal includes articles received from authors from around the world in the field of welding, cutting, cladding, soldering, brazing, coating, 3D additive technologies, electrometallurgy, material science, NDT and selectively includes translations into English of articles from the following journals, published in Ukrainian:
- Automatic Welding (https://patonpublishinghouse.com/eng/journals/as);
- Electrometallurgy Today (https://patonpublishinghouse.com/eng/journals/sem);
- Technical Diagnostics & Nondestructive Testing (https://patonpublishinghouse.com/eng/journals/tdnk).

CONTENTS

ORIGINAL ARTICLES

*Translated Article(s) from “Automatic Welding”, No. 12, 2023.

**Translated Article(s) from “Electrometallurgy Today”, No. 4, 2023.

***Translated Article(s) from “Electrometallurgy Today”, No. 4, 2023.

DOI: https://doi.org/10.37434/tpwj2024.01.01

INFLUENCE OF COOLING RATE ON MICROSTRUCTURE AND PHASE COMPOSITION OF HAZ OF DUPLEX (DSS) 2205 STEEL IN WET UNDERWATER WELDING

S.Yu. Maksymov[1], G.V. Fadeeva[1], Jia Chuanbao[2], V.A. Kostin[1], A.A. Radzievskaya[1], D.V. Vasilyev[1]

[1]E.O. Paton Electric Welding Institute of the NASU
11 Kazymyr Malevych Str., 03150, Kyiv, Ukraine
[2]Institute of Materials Joining, Shandong University
17923 Jingshi Road, Jinan 250061, China

ABSTRACT

The article shows the results of the analysis of changes in the microstructure and volumetric particles of phase components of HAZ metal in modeling of welding thermal cycles, inherent in wet underwater welding and welding in air, with the use of the Gleeble-3800 system. The value of cooling rate of different areas of weld metal in wet underwater welding and welding in air was determined. It is shown that as a result of cooling impact of water environment, the cooling rate in wet underwater welding is almost by an order higher than that of welding in air ($w_{13/8}$ = 8.21 °C/s — air, in the middle of the weld, and in wet underwater welding it is accordingly $w_{13/8}$ = 81.70 °C/s in the middle of the weld, $w_{13/8}$ = 165.85 °C/s at the beginning of the weld and $w_{13/8}$ = 320.51 °C/s in the weld crater). The change in volumetric particles of phase components of ferrite, austenite and excess phases (chromium Cr_2N nitrides) was determined in the microstructure of HAZ metal depending on the cooling rate. Phase transformations almost completely occur in the high-temperature heat-affected zone (HHAZ) in the temperature range T = 1300–800 °C. Contribution of low-temperature heat-affected zone (LHAZ), temperature range T = 800–500 °C on the change in phase components is negligible. The amount of ferritic and austenitic components and especially the morphology of austenite in the microstructure of HHAZ depend on the cooling rate, as well as the amount of precipitation of excess phases (probably, chromium Cr_2N nitrides)

KEYWORDS: duplex steels, wet underwater welding, input energy, cooling rate, phase composition. austenite, ferrite, microstructure in HAZ, HAZ simulation, thermal welding cycle, Gleeble

INTRODUCTION

The difference in the physical properties of the water environment, first of all, which are 4 times higher than heat capacity and 25 times higher than thermal conductivity compared to air cause a higher cooling rate both in the high-temperature HAZ, which corresponds to the temperature range of 1300–800 °C, and in the low-temperature HAZ, which corresponds to the temperature range of 800–500 °C, relative to other types of welding. Information on the values, that exactly correspond to the cooling rate in wet underwater welding is almost absent in the literature.

ANALYSIS OF EXISTING PROCEDURES FOR DETERMINATION OF INFLUENCE OF THERMAL WELDING CYCLES (TWC) ON HAZ MICROSTRUCTURE. PROBLEM STATEMENT

To obtain data on the structure and dynamics of phase transformations in duplex stainless steels during welding, it is necessary to investigate the temperature range, which according to the pseudobinary diagram of Fe–Cr–Ni (Figure 1) [1] corresponds to the temperature range of 1200 (1300)–800 °C, depending on the chemical composition of the steel. There are several methods to obtain data on the temperature-time dependences in the field of phase transformations.

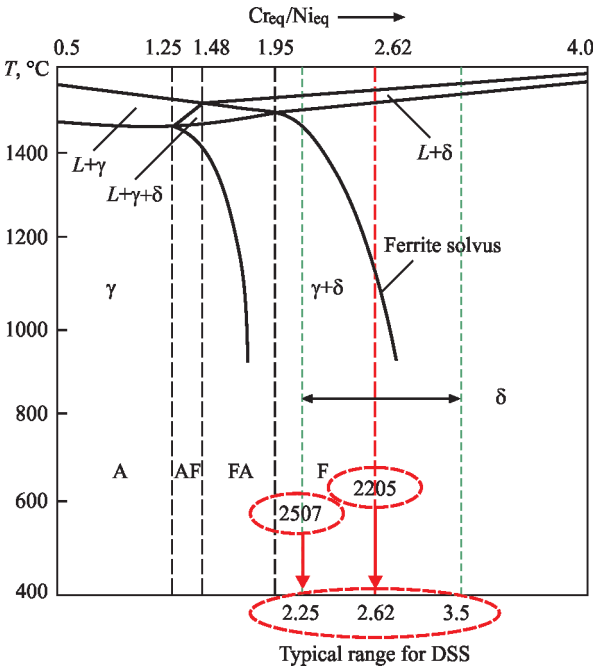

Figure 1. Pseudobinary (Fe–Cr–Ni) diagram, built with the help of the equivalent Cr_{eq}/Ni_{eq} ratio [1]

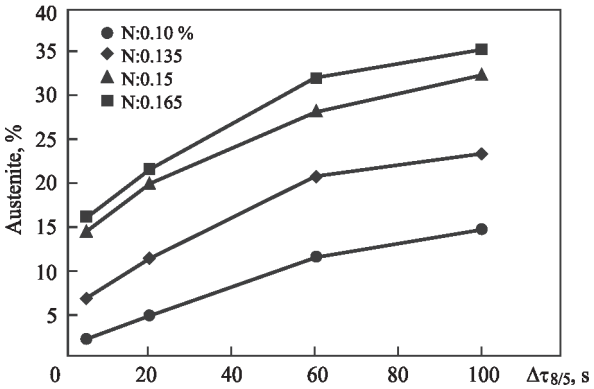

Figure 2. Changes in the content of austenite depending on the time of cooling at different concentrations of nitrogen [6]

One of the methods is a procedure applied to the obtained data on real TWC by recording the temperature and time of the metal being in the temperature range of phase transformations. With the help of thermocouples, the temperature and the time spent in the mentioned temperature range are recorded, to which a certain area of the welded joint is corresponded. Based on these data, the average cooling rate in this range is calculated. The procedure of recording TWC parameters obtained with the help of thermocouples, placed directly in the welding zone or in the HAZ, is very time-consuming and associated with great difficulties, especially when recording TWC in the weld metal. Most often, thermocouples are placed in the HAZ of a welded joint. There are publications where recording of TWC was carried out directly in the weld metal. A new procedure was developed, which uses a combination of thermocouples placed in a pool of a molten weld metal and simultaneously placed on the back side of a weld through drilled holes [2, 3]. This procedure was applied and improved to obtain data on the cooling rates of the weld metal in welding multilayer joints of superduplex 2507 steel [4].

A new heat treatment method has recently been presented, in which a stationary TIG arc affects a disc-shaped specimen. This method allows covering the entire temperature range from room to liquidus temperature in a one specimen, thereby significantly reducing a quantity of specimens required to obtain microstructures corresponding to certain temperatures [5].

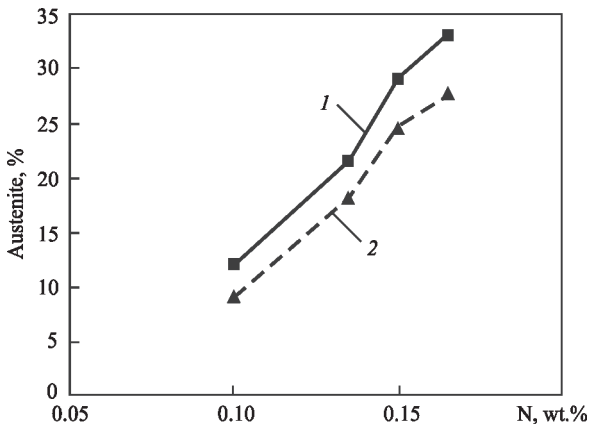

Figure 3. Comparison of austenite content based on the Gleeble simulation (*1*) and nitrogen content [6] in the HAZ microstructure in real welding [6]

The procedure of using systems of different modifications of the Gleeble type is well-known, with the help of which, a number of microstructures necessary for research is simulated.

In [6], modeling of microstructures was carried out with the use of the Gleeble system to assess the effect of cooling time and alloying elements on the HAZ microstructure of duplex stainless steel. In addition, submerged arc welding of steel was performed to compare the HAZ microstructures obtained by simulation with Gleeble and in real welding. Modeling of microstructures in the Gleeble-1500 thermomechanical simulator was performed according to the heat treatment mode. The peak temperature T = 1350 °C, exposure τ = 1 s, and then the time of cooling from the temperature of 800 to 500 °C ($\Delta\tau_{8/5}$) was 5; 20; 60 and 100 s, respectively.

It was determined that the optimal cooling time ($\Delta\tau_{8/5}$) after welding is from 30 to 60 s for duplex stainless steel with the chemical composition: 0.165 % N–5.5 % Ni–22.3 % Cr–3.2 Mo. It is shown that cooling in the temperature range from 800 to 500 °C in the interval of 30–60 s ensures the content of austenite in the HAZ of not lower than 25 %.

Figure 2 shows changes in the austenite content depending on the cooling time and nitrogen concentration.

Analyzing the given data in Figure 2, it can be noted that the concentration of nitrogen has a greater effect on the austenite content than the cooling time $\Delta\tau_{8/5}$.

Figure 3 shows the content of austenite, which is determined in the microstructure during modeling with Gleeble and in the HAZ microstructure in real welding of steels with a different nitrogen content.

The difference in the amount of austenite in the microstructures simulated by Gleeble and real HAZ obtained during welding is relatively small at the similar cooling time. Thus, the cooling time set by Gleeble can be successfully used as a reference point when choosing welding conditions for duplex steels.

When studying the influence of input energy on the evolution of austenite in the simulated HAZ of duplex 2205 steel, experiments on simulation the welding thermal cycle were carried out in the MMS-200 thermomechanical simulator according to simulated welding thermal cycles corresponding to different input energies [7]. The values of input energy are comparable to those used in submerged arc welding. The morphology of austenite precipitation in the HAZ microstructure depending on the input energy and the

effect of the microstructure on the impact toughness were studied. Thermal cycles were simulated according to the levels of input energy. Input energy was determined with the use of mathematical models by $\tau_{8/5}$, where $\tau_{8/5}$ is the cooling time for the specimen from 800 to 500 °C. Different values of $\tau_{8/5}$ 6; 20; 50; 100; 300 and 600 s were taken to obtain different values of heat input, which corresponded to the next values: 6.2; 11.3; 17.8; 25.2; 43.7 and 61.8 kJ/cm. The calculated levels of input energy correspond to real levels in submerged arc welding from low to superhigh input energy. When determining the share of austenite in the HAZ microstructure, the following conclusion was reached after modeling. The content of austenite lower than 20 % corresponds to the input energy of 0.62 kJ/mm and austenite/ferrite ratio of 1:1 is achieved when the input energy is increased to 6.18 kJ/mm. The value of impact toughness changes and correlates accordingly with the morphology of austenite precipitation in the HAZ.

With the use of the Gleeble™-1500 system, a number of microstructures were simulated, representing those available in the HAZ of welded joints of duplex steels [8]. The simulation took place according to the thermal procedure: heating at a rate of 130 °C/s until reaching the peak temperature T = 1300 °C, holding at the peak temperature τ = 1 s and τ = 10 s, then cooling at a rate from 90 to 2.0 °C/s. I.e., the cooling rate from a temperature of 1300 °C was used as a variable. The data obtained as a result of the conducted studies allow assuming that the welding process with low and medium heat inputs, which provide a cooling rate of HAZ in the range from 20 to 50 °C/s, should be the most effective for ensuring the necessary impact toughness of HAZ to –20 °C. This range of cooling rate provides a good balance between the grain size and ferrite/austenite ratio. It was also determined that high cooling rates contribute to both the preservation of ferrite as well as higher deposition of nitrides.

In [9], the study of the cooling time on the microstructure and properties of HAZ in 2507 steel was carried out using the Gleeble™-3800 thermomechanical simulator. The heating rate was 100 °C/s, and the maximum temperature was 1250 °C. The specimens were held for 2 s before cooling. Since the range from 800 to 500 °C was the most uncertain temperature range, and the range from 1200 to 800 °C was a typical range in which the transformation of ferrite into austenite took place, two $\tau_{8/5}$ ranges were chosen — cooling time from 800 to 500 °C and $\tau_{12/8}$ — cooling time from 1200 to 800 °C to study the effect of cooling time on the microstructure and properties of 2507 steel. To analyze and compare the influence of different values of $\tau_{8/5}$ and $\tau_{12/8}$ on HAZ modeling, three groups of cooling parameters were chosen, as given in Table 1.

Table 1. Cooling parameters in temperature ranges

Description of groups	Cooling time in temperature ranges, s	
	$\tau_{8/5}$	$\tau_{12/8}$
1	20; 50; 100; 300	7; 18; 37; 120
2	7; 20; 50; 100	7; 7; 7; 7
3	20; 20; 20	7; 18; 37

As $\tau_{12/8}$ and $\tau_{8/5}$ grew, the content of ferrite decreased and the content of austenite increased, but $\tau_{12/8}$ was a more important cooling parameter that affects the final microstructure of thermal modeling of HAZ of 2507 SDSS. At a ferrite content of about 50 %, $\tau_{8/5}$ was 100 s, whereas $\tau_{12/8}$ was only 37 s. The impact toughness of HAZ grew with an increase in $\tau_{12/8}$, similarly, the resistance to pitting corrosion in the HAZ during welding increased with an increase in $\tau_{12/8}$ and $\tau_{8/5}$, but the effect of $\tau_{12/8}$ was particularly obvious. The most optimal properties were provided when $\tau_{12/8}$ was from 18 to 37 s ($\tau_{8/5}$ = 20 s).

In [6], the cooling time in the temperature range from 800 to 500 °C, $\tau_{8/5}$, was chosen as a variable criterion. In [7], $\tau_{8/5}$ was also chosen, then, according to mathematical models, it was converted to the corresponding values of input energy. The rate of cooling from a temperature of 1300 °C was chosen as a variable parameter in [8]. The authors of [9] also studied the cooling time in two temperature ranges, namely $\tau_{12/8}$ and $\tau_{8/5}$.

The results of extensive research on wet underwater welding of duplex steels and the properties of the produced joints are not found in the literature.

As a result of the analysis of studies [6-9] on the application of thermomechanical simulators of the Gleeble type to study the influence of various criteria on the microstructure and phase balance of HAZ of duplex steels, which in turn affect the main technological properties of duplex steels, such as mechanical properties and corrosion resistance, it can be noted, that almost all studies relate to the parameters inherent during welding in air using various technologies. In addition, there was no work that used a real thermal cycle in wet underwater welding of duplex steels to model HAZ.

Therefore, the aim of this examination was to determine and study the effect of cooling rate on the microstructure and phase composition of HAZ of duplex steels, which is simulated by the Gleeble method, using real welding thermal cycles corresponding to wet underwater welding compared to air welding.

RESEARCH METHODOLOGY AND METHODS

The Gleeble-3800 complex was used to study the influence of cooling rate on the microstructure and

Table 2. Chemical composition of 2205 steel (certificate data)

Number according to EN standard	Designation according to EN standard	Steel grade	Content of elements, wt.%								
			C	Mn	P	S	Si	Ni	Cr	Mo	N
1.4462	Kh2CrNiMoN 22-5-3	2205	0.018	1.936	0.03	0.0008	0.303	4.931	22.146	2.557	0.1515

Table 3. Numerical values of TWC parameters

Specimen number	Temperature range, °C; cooling rate w_{cool}, °C/s; cooling time τ, s			
	1300–800		800–500	
	$w_{13/8}$	$\tau_{13/8}$	$w_{8/5}$	$\tau_{8/5}$
1 — air (middle of the weld)	8.21	60.88	5.02	59.78
2 — water (middle of the weld)	81.70	6.12	50.34	5.96
3 — water (beginning of the weld)	165.85	2.94	100.00	3.00
4 — water (crater)	320.51	1.56	161.29	1.86

phase composition of HAZ of duplex 2205 steel under the action of thermal cycle in wet underwater welding compared to welding in air [10]. It was used to model a number of microstructures that correspond to those formed in the HAZ under the influence of welding thermal cycle. The chemical composition of the studied steel is given in Table 2.

To model thermal cycles, which are inherent to those in wet underwater welding and welding in air, the curves were used obtained experimentally applying thermocouples (Figure 4) [11].

Table 3 shows the values of cooling rates and the time spent by the specimens in different temperature ranges during TWC simulation, which correspond to those presented in Figure 4.

Numerical values of parameters were obtained as a result of differentiation of TWC curves.

HAZ simulation was carried out according to the thermal procedure: heating was carried out at a rate of 100 °C/s to a temperature of T = 1300 °C, holding time at a peak temperature τ = 2 s, during cooling of the specimens, TWC were simulated, which are shown in Figure 4 and according to the data presented in Table 3.

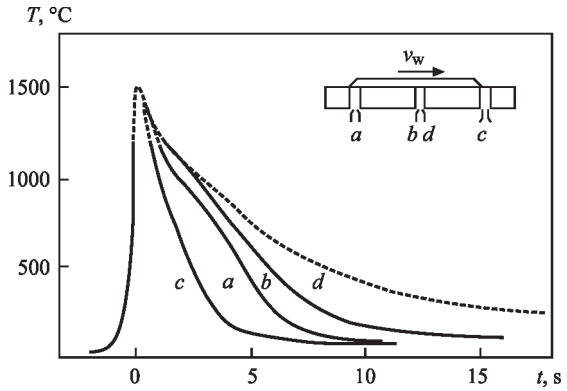

Figure 4. Influence of environment on the nature of welding thermal cycle in different weld areas [11]: *a* — beginning of the weld, specimen No. 3 (water); *b* — middle of the weld, specimen No. 2 (water); *c* — weld crater, specimen No. 4 (water); *d* — middle of the weld, specimen No. 1 (air)

To study the effect of cooling rates and cooling time on the microstructure and phase composition of HAZ, two ranges of cooling rates $w_{13/8}$ and $w_{8/5}$ were chosen, which correspond to the high-temperature HHAZ and low-temperature LHAZ. The same applies to the cooling time in the corresponding ranges, $\tau_{13/8}$ and $\tau_{8/5}$. The temperature range of 1200 (1300)–800 °C, depending on the chemical composition of the metal with a typical range, in which the transformation of ferrite into austenite occurs to the greatest extent during cooling. The temperature range of 800–500 °C was chosen to analyze and compare the influence of different ranges on HAZ microstructure during modeling.

If we analyze the values of TWC parameters given in Table 3, namely, the time spent in the temperature range $\tau_{13/8}$, for different areas of the weld in wet underwater welding, i.e.: the middle of the weld is 6.12 s; the beginning of the weld is 2.94 s; weld crater is 1.56 s, so it is less than 10 s. I.e., no value corresponds to the concept, according to which it is recommended to cool a welded joint in the temperature range of 1200–800 °C within 10 s from the time of achieving the optimal microstructure and properties of the welded metal [12].

After thermal modeling, the specimens were cut out in such a way as to cover all areas of the microstructures formed after TWC modeling. The further studies were carried out using optical microscopy (OM) and analytical scanning electron microscopy (SEM). The content of austenite and ferrite in simulated HAZ specimens was determined with the use of the MIPAR image analysis software.

To reveal the microstructure, electrolytic etching was carried out in a 10 % solution of ammonium sulfate at a voltage of 15 V for 20 to 40 s.

Optical metallography was performed in Versamet-2 (USA) and Neophot-32 (Germany) microscopes. Microhardness was measured in M400 Leco device.

RESULTS AND DISCUSSION. ANALYSIS OF HAZ MICROSTRUCTURES

Figures 5 and 6 show the microstructures in different areas of HAZ simulated at different cooling rates.

When analyzing the microstructures shown in Figures 5 and 6, it should be noted that a change in the shape of austenite grains is observed, the size of austenite and ferrite grains decreases by an average of 1.5 times, especially in a high-temperature HAZ (T = 1300–800 °C). The morphology of austenite precipitation also changes. During cooling, grain-boundary austenite (GBA) begins to be formed on the grain boundaries of δ-ferrite, and then acicular (Widmanstaetten) austenite (WA) nucleates along the grain boundaries of δ-ferrite grains and grows in the middle of the grain. In addition to grain-boundary austenite and acicular (Widmanstaetten) austenite, if there is

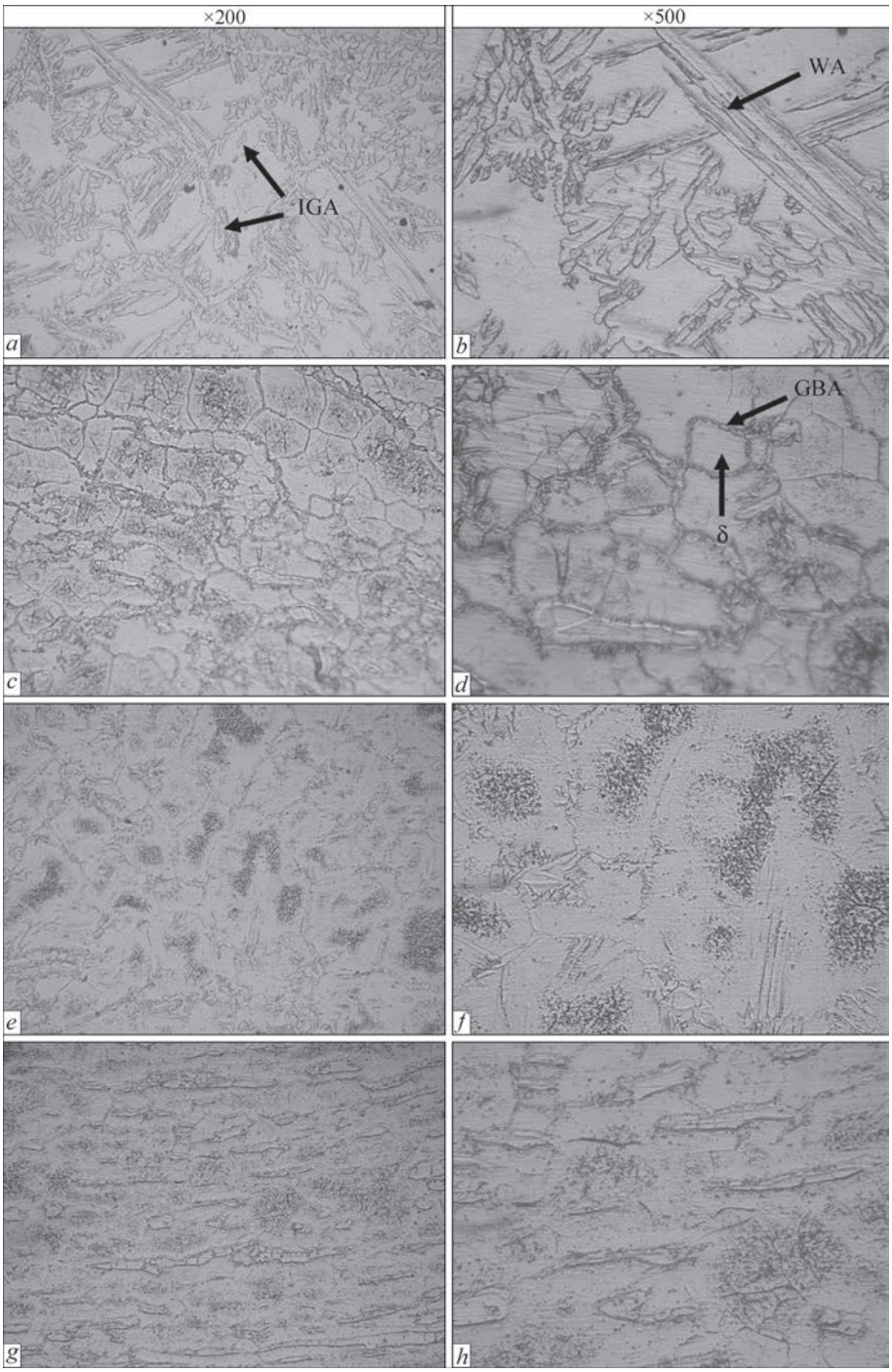

Figure 5. Microstructures of high-temperature HAZ simulated at different cooling rates in the temperature range T = 1300–800 °C: *a*, *b* — specimen No. 1, air, $w_{13/8}$ = 8.21 °C/s; *c*, *d* — specimen No. 2, water — middle of the weld, $w_{13/8}$ = 81.70 °C/s, *e*, *f* — specimen No. 3, water — the beginning of the weld, $w_{13/8}$ = 165.85 °C/s; *g*, *h* — specimen No. 4, water — weld crater $w_{13/8}$ = 320.51 °C/s

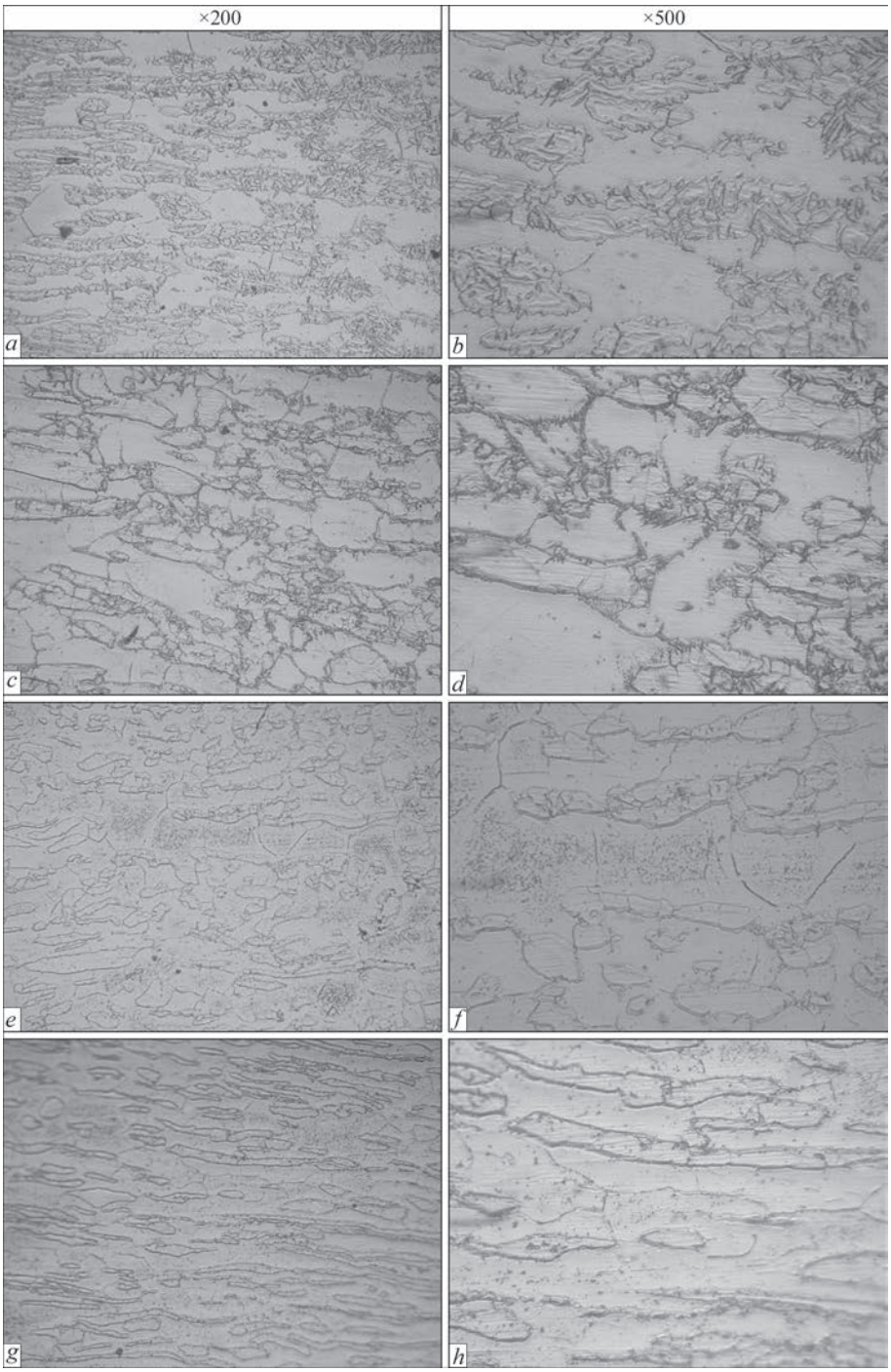

Figure 6. Microstructures of low-temperature HAZ simulated at different cooling rates in the temperature range T = 800–500 °C: *a*, *b* — specimen No. 1, air, $w_{8/5}$ = 5.02 °C/s; *c*, *d* — specimen No. 2, water — middle of the weld, $w_{8/5}$ = 50.34 °C/s; *e*, *f* — specimen No. 3, water — the beginning of the weld, $w_{8/5}$ = 100.00 °C/s; *g*, *h* — specimen No. 4, water — weld crater, $w_{8/5}$ = 161.29 °C/s

enough time for diffusion (depending on the cooling rate), intragranular austenite (IGA) may nucleate and grow in the middle of δ-ferrite grains. Since GBA and WA require less supercooling (which is controlled by the cooling rate) for nucleation and growth compared to IGA, they have more time to grow and thus, they dominate in the final microstructure, especially at a low cooling rate.

In general, the microstructure in HAZ of duplex stainless steel changes as follows: during heating, austenite transforms into ferrite, and ferrite grains grow upon heating to a peak temperature of T = 1300–1350 °C (depending on the chemical composition of metal). This temperature corresponds to the single-phase region of ferrite (Figure 1) [1]. During subsequent cooling with a decrease in temperature, ferrite loses its stability and transforms into austenite in the temperature range T = 1300–500 °C, which corresponds to the two-phase region of austenite and ferrite. The final phase composition of HAZ microstructure is the result after these two processes, namely, heating and then cooling. The final HAZ

Table 4. Size of ferrite grains in the HAZ metal structure depending on the cooling rate

Description of zones	Temperature range, °C	Cooling rate $w_{13/8}$, °C/s			
		8.21	81.70	165.85	320.51
		Grain size h×1, μm			
I — coarse grain zone	1300–800 HHAZ	100–350×150–450	60–130×100–400	125–250×150–300	80–230×120–300
II — normalization zone	1100–800 HHAZ	50–150×100–160	50–100×100–200	50–155×100–200	50–150×100–200

microstructure mainly depends on the cooling stage, which is characterized by the welding thermal cycle. At a cooling rate $w_{13/8}$ = 8.21 °C/s, the presence of all types of austenite is observed, a large amount of grain-boundary austenite, almost along all grain boundaries, as well as intragranular austenite, and acicular (columnar), i.e., Widmanstaetten austenite. The precipitation of excess fine phases was not detected. With an increase in the cooling rate from $w_{13/8}$ = 81.70 to 320.51 °C/s, the morphology of austenite precipitation changes. Precipitation of Widmanstaetten austenite is no longer observed and the amount of intragranular austenite is decreasing. At lower cooling rates, in addition to it, grain-boundary austenite is present, and at a cooling rate $w_{13/8}$ = 320.51 °C/s, almost only grain-boundary austenite is present in the microstructure. With an increase in the cooling rate from $w_{13/8}$ = 81.70 to $w_{13/8}$ = 320.51 °C/s, the precipitation of an excess fine phase is observed, mainly in the coarse ferrite grains, as well as sometimes at the boundaries of austenite and ferrite grains.

When measuring microhardness at a cooling rate $w_{13/8}$ = 8.21 °C/s, the most important is austenite in HHAZ, both acicular (Widmanstaetten), as well as grain-boundary austenite, HV = 3300–5150 MPa. A decrease in the microhardness of austenite occurs with an increase in the cooling rate from $w_{13/8}$ = 8.21 to $w_{13/8}$ = 320.51 °C/s, as in HHAZ (T = 1300–800 °C) as well as in LHAZ (T = 800–500 °C) and is in the range of HV = 3360–4390 MPa. Microhardness of austenite in BM is mainly HV = 2970–3090 MPa, sometimes it reaches HV = 3300–3570 MPa. Such a change in the microhardness of austenite may indicate that the main element that affects the microhardness of austenite is nitrogen. Microhardness of austenite depends on its content content in the lattice. Microhardness of ferrite at all cooling rates is from $w_{13/8}$ = 8.21 °C/s to $w_{13/8}$ = 320.51 °C/s, both in HHAZ (T = 1300–800 °C) as well as in LHAZ (T = 800–500 °C) is almost the same and equals to HV = 2300–2900 MPa. Microhardness of ferrite in the base metal is almost the same HV = 2300–2570 MPa, sometimes it reaches HV = 2970 MPa, i.e., microhardness of ferrite remains unchanged both in HAZ as well as in the base metal.

Table 4 shows the size of ferrite grains in the simulated HAZ.

At all cooling rates, the refinement of ferrite grains in the II temperature zone compared to the I zone is observed. At a cooling rate $w_{13/8}$ = 320.51 °C/s, the size of ferrite grains in HHAZ is the lowest and is equal to 80–230×120–300 μm (I zone), and 50–150×100–200 μm (II zone) (Table 4).

This data reaffirms that the time spent in the temperature range of phase transformations is not the only factor that affects the completeness of phase transformations, as well as depends on the size of ferrite grains, i.e., on the diffusion of both ferrite- as well as austenite-forming elements: nitrogen, nickel, manganese, and primarily on the nitrogen diffusion coefficient, since it is higher than other elements: nickel, manganese, chromium and molybdenum.

PHASE COMPOSITION OF HAZ

Figure 7 shows changes in volumetric particles of phase components, ferrite, austenite and excess phase (probably, precipitation of Cr_2N chromium nitrides) depending on the cooling rate in the simulated HAZ of duplex steel in the temperature range T = 1300–800 °C determined with the use of the MIPAR software for image analysis.

Figure 8 shows microstructures of the simulated HAZ at different cooling rates corresponding to the temperature range T = 1300–800 °C, which were used to determine the phase composition by means of the MIPAR software.

Table 5 shows the values of volumetric particles of phase components of the simulated HAZ at different cooling rates in the temperature range

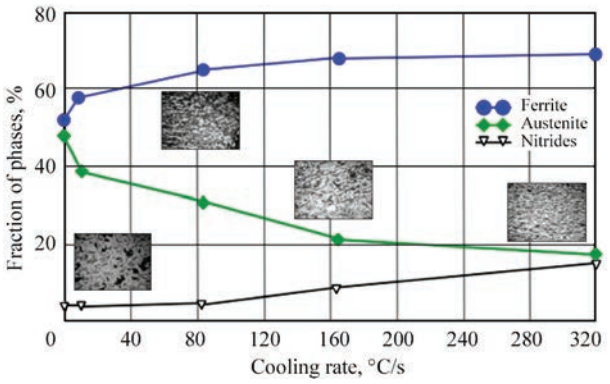

Figure 7. Phase composition of HAZ of duplex steel depending on the cooling rate in the temperature range of 1200 (1300)–800 °C

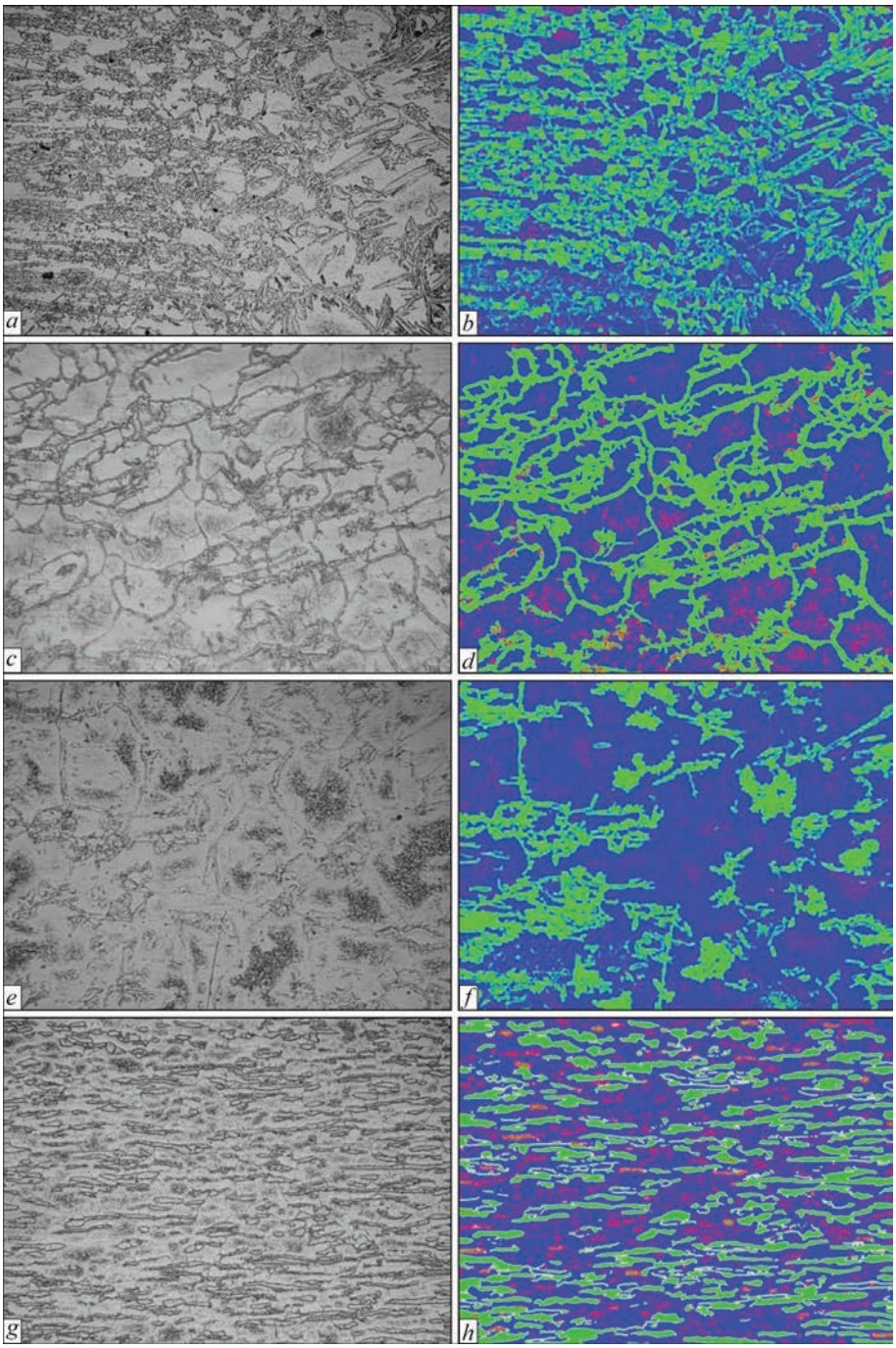

Figure 8. Microstructures (×100) of simulated HAZ at different cooling rates, processed with the use of the MIPAR software: *a*, *b* — specimen No. 1, air, $w_{13/8}$ = 8.21 °C/s; *c*, *d* — specimen No. 2, water — middle of the weld, $w_{13/8}$ = 81.70 °C/s; *e*, *f* — specimen No. 3, water — beginning of the weld, $w_{13/8}$ = 165.85 °C/s; *g*, *h* — specimen No. 4, water — weld crater. $w_{13/8}$ = 320.51 °C/s. Matrix — ferrite; grain — austenite; small inclusions — nitrides

Table 5. Phase composition of HAZ simulated at different cooling rates in the temperature range T = 1300–800 °C

HAZ cooling rate, °C/s	Fraction of phases, %		
	δ, ferrite	γ, austenite	Excess phase (fine)
Base metal	52.000	48.000	–
8.21	57.499	38.674	3.236
81.70	64.644	30.268	3.746
165.85	67.696	20.965	8.606
320.51	68.848	17.733	13.437

T = 1300–800 °C, which were determined with the use of the MIPAR software.

If we compare the phase composition of the microstructures at different cooling rates in the high-temperature range of HHAZ (T = 1300–800 °C), then with an increase in the cooling rate from $w_{13/8}$ = 8.21 to 320.51 °C/s, the content of austenite decreases more than twice, and the content of ferrite, on the contrary, increases by 1.2 times.

The data given in Table 5, indicate that the transformation of ferrite into austenite occurs almost com-

pletely in HHAZ in I and II zones in the temperature range T = 1300–800 °C, and the completeness of the transformation depends on the time spent in this range and on the size of ferrite grains. At the same time, the morphology of austenite precipitation depends to a greater extent on the time spent in this temperature range. At a cooling rate $w_{13/8}$ = 8.21 °C/s, the time spent in the temperature range T = 1300–800 °C is 60.88 s, in the microstructure the presence of all types of austenite is observed: grain-boundary, Widmanstaetten and intragranular. Precipitation of excess phases is not observed. When the cooling rate grows to $w_{13/8}$ = 320.51 °C/s, the morphology of austenite precipitation changes, precipitation of acicular (Widmanstaetten) austenite is not observed anymore and the amount of intragranular austenite decreases. At all cooling rates, grain-boundary austenite is present, and at a cooling rate $w_{13/8}$ = 320.51 °C/s, in the microstructure, mostly only grain-boundary austenite is present. With an increase in the cooling rate from $w_{13/8}$ = 81.70 to 320.51 °C/s, precipitation of tiny excess phases is observed mainly in the coarse ferrite grains, as well as sometimes at the boundaries of austenite and ferrite grains.

The analysis of chemical elements in the high-temperature HAZ (T = 1300–800 °C) revealed precipitation of excess phases with an increased content of chromium in both austenite and ferrite. This is explained by the fact that at a high cooling rate, the transformation of ferrite into austenite does not occur to the full extent, the amount of austenite precipitation decreases, and an excess phase with a higher chromium content is observed in ferrite grains (probably, Cr_2N). At a cooling rate $w_{13/8}$ = 320.51 °C/s in the I zone (T = 1300–800 °C), in ferrite grains, with the use of a scanning microscope (SEM), rod-type inclusions of up to 10 μm in length with a chromium content of 23.2–24.14 % were revealed. Chromium Cr_2N nitrides found in [13] also have a rod-like appearance. This indicates that these are probably Cr_2N chromium nitrides, since the base metal contains 0.1515 % of nitrogen and the carbon content is lower than 0.02 % (0.018 %). Since the process of transformation of ferrite into austenite is a diffusion process, the completeness of the transformation of ferrite into austenite, that is, the final phase composition of HAZ microstructure, depends on the diffusion coefficients of ferrite-forming elements and austenite-forming elements, primarily nitrogen (Table 5, Figure 7).

The obtained data may indicate that the completeness of phase transformations depends not only on the cooling rate and time spent in the temperature range, where the transformation of ferrite into austenite occurs, but also on the size of ferrite grains.

CONCLUSIONS

1. The influence of cooling rate on the microstructure and phase composition in the simulated HAZ of duplex 2205 steel with the use of Gleeble-3800 was studied. Simulated microstructures with cooling rates from $w_{13/8}$ = 8.21 to 320.51 °C/s, as well as from $w_{8/5}$ = 5.02 to 161.29 °C/s showed a change in the phase composition of austenite and ferrite. To the greatest extent, the change in the volumetric particles of phases occurs at the cooling rates $w_{13/8}$ — from 81.70 to 320.51 °C/s, which correspond to the cooling rates in wet underwater welding in the high-temperature HAZ.

2. When the cooling rate $w_{13/8}$ grows from 8.21 to 320.51 °C/s, the volumetric fraction of austenite decreases by 2.18 times (from 38.67 to 17.73 %), the volumetric fraction of ferrite, on the contrary, grows by 1.2 times (from 57.41 to 68.85 %).

3. The content of austenite at the cooling rates from $w_{13/8}$ 81.70 to — 320.51 °C/s, which correspond to the cooling rates in wet underwater welding, decreases from 30.27 to 17.73 %. The main part is formed by grain-boundary and intragranular austenite. At the cooling rates $w_{13/8}$ = 8.21 and 5.02 °C/s, which are inherent during welding in air, all types of austenite are observed: grain-boundary, acicular (Widmanstaetten), and intragranular austenite.

4. The phase transformation of ferrite into austenite occurs mostly in the high-temperature HAZ, in the temperature range T= 1300–800 °C.

5. The completeness of phase transformation of ferrite into austenite depends on the cooling rate, i.e., the time spent in a given temperature range, and also on the sizes of ferrite grains.

6. The amount of excess phase precipitation (probably, chromium Cr_2N nitrides) is directly proportional to the cooling rate and also depends on the amount of the austenitic component. With an increase in the cooling rate, the amount of chromium nitride precipitation almost four times increases, i.e. from 3.24 to 13.44 %.

7. With an increase in the cooling rate, a decrease in the size of ferrite grains is observed.

8. The amount of ferritic component grows with an increase in the cooling rate, but it is not critical and amounts to 68.85 %, i.e., it does not reach 70 %, which is allowed by recommendations and standards. Despite the fact that the cooling rate in wet underwater welding is by an order higher than during welding in air, due to the refinement of the microstructure, a critical increase in the fraction of ferrite is not observed.

9. The obtained data can be used when choosing the modes and a type of weld metal alloying in wet underwater welding.

10. Recommendations for the range of welding input energy values Q = 0.5–2.5 kJ/mm for 2205 steel developed for welding in air and which contribute to obtaining a balanced phase composition of HAZ of duplex stainless 2205 steel, should be subjected to correction in wet underwater welding.

11. The results of studies on the influence of cooling rate on the microstructure and phase composition of HAZ of duplex (DSS 2205) steel simulated by the Gleeble-3800 method correspond only to those TWC and those chemical compositions of the base metal that are used in this study.

REFERENCES

1. Verma, I., Taiwade, R., R.V (2017) Effect of welding processes and conditions on the microstructure, mechanical properties and corrosion resistance of duplex stainless steel weldments — A review. *J. of Manufacturing Processes*, **25**, 134–152.
2. Bermejo, V.M.A., Hurtig, K., Hosseini, V.A. et al. (2016) Monitoring thermal cycles in multi-pass welding. In: *Proc. of the 7th Int. Swedish Production Sym. — SPS-16, (Lund, Sweden, 25–27 October)*.
3. Bermejo, V.M.A., Hurtig, K., Karlsson, L., Svensson, L.E. (2017) A step forward in understanding superduplex multi-pass welds by monitoring thermal cycles. In: *Proc. of the 70th IIW Annual Assembly (Shnghai, China, 28 June 2017).*
4. Bermejo, M.A.V., Daniel, E., Hurtig, K., Karlsson, L. (2019) *A new approach to the study of multi-pass welds microstructure and properties of welded 20-mm-thick superduplex stainless steel*. http://www.researchgate.net/publication/331715232
5. Hosseini, V.A., Karlsson, L., Engelberg, D., Wessman, S. (2018) Time-temperature — precipitation and property diagrams for super duplex stainless steel weld metals. *Weld. World*, **62**, 517–533.
6. Hsienh, R.-J., Liou, H.-Y., Pan, Y.-Ts. (2001) Effects of cooling time and alloying elements on the microstructure of the Gleeble-simulated heat-affected zone of 22 % Cr duplex stainless steels. *J. of Mater. Eng. and Performance*, 10(**5**), 526–536.
7. Wu, T.-h., Wang, J.-j., Li, H.-b et al. (2018) *Effect of heat input on austenite microstructural evolution of simulated heat affected zone in 2205 duplex stainless steel*. DOI: https://doi.org/10.1007/s42243-018-0134-z
8. Lippold, J.C., Varol, I., Baeslack, W.A. (1994) The influence of composition and microstructure on the HAZ toughness of duplex stainless steels at –20 °C. *Welding J., Res. Suppl.* **I**, 75–79.
9. Zhou, Y., Zou, D., Li, K. et al. (2018) Effect of cooling time on microstructure and properties of 2507 super duplex stainless steel welding heat-affected zone. *Mat. Sci. Forum,* **940**, 5358.
10. 10.Grigorenko, G.M., Kostin, V.A., Orlovsky, V.Yu. (2008) Current capabilities of simulation of austenite transformations in low-alloyed steel welds. *The Paton Welding J.,* **3**, 22–24.
11. Hasui, A., Suga, Y. (1980) On cooling of Underwater Welds. *Transact. of the JWS*, 11(**1**). April.
12. Geipl, H. (1989) MAGM-Schweissen von Rorrosions beständign Duplex-Stahlen 22Cr5(9)Ni3Mo. Entfluss von schutzgas-und werfahrenvarianten. Linde – Sonderdruck, **146**, Häll-riegels – kreuth.
13. Hu, Y., Shi, Y., Shen, X., Wang, Zh. (2017) Microstructure, pitting corrosion resistance and impact toughness of duplex stainless steel underwater dry hyperbaric flux-cored arc welds. *Materials*, **10**, 1443, www.mdpi.com/journal/materials

ORCID

S.Yu. Maksymov: 0000-0002-5788-0753

CONFLICT OF INTEREST

The Authors declare no conflict of interest

CORRESPONDING AUTHOR

S.Yu. Maksymov
E.O. Paton Electric Welding Institute of the NASU
11 Kazymyr Malevych Str., 03150, Kyiv, Ukraine.
E-mail: maksimov@paton.kiev.ua

SUGGESTED CITATION

S.Yu. Maksymov, G.V. Fadeeva, Jia Chuanbao, V.A. Kostin, A.A. Radzievskaya, D.V. Vasilyev (2024) Influence of cooling rate on microstructure and phase composition of HAZ of duplex (DSS) 2205 steel in wet underwater welding. *The Paton Welding J.*, **1**, 3–12.

JOURNAL HOME PAGE

https://patonpublishinghouse.com/eng/journals/tpwj

Received: 06.09.2023
Received in revised form: 13.10.2023
Accepted: 16.01.2024

DOI: https://doi.org/10.37434/tpwj2024.01.02

HYBRID LASER-PLASMA WELDING: EFFICIENCY AND NEW POSSIBILITIES (REVIEW)

V.M. Korzhyk[1], V.Yu. Khaskin[1], E.V. Illyashenko[1], S.I. Peleshenko[3], A.A. Grynyuk[1], O.A. Babych[2], A.O. Alyoshin[2], O.M. Voitenko[1]

[1]E.O. Paton Electric Welding Institute of the NASU
11 Kazymyr Malevych Str., 03150, Kyiv, Ukraine
[2]"Foreign Trade Office of China-Ukraine E.O. Paton Institute of Welding" Ltd.
11 Kazymyr Malevych Str., 03150, Kyiv, Ukraine
[3]National Technical University of Ukraine "Igor Sikorsky Kyiv Polytechnic Institute"
37 Prospect Beresteiskyi (former Peremohy), 03056, Kyiv, Ukraine

ABSTRACT

Research papers devoted to development of laser-plasma processes during the last two decades are reviewed. It was found that the current directions of scientific research of the processes of laser-plasma welding are focused mainly on studying the peculiarities of simultaneous impact of constricted arc plasma and laser radiation with wave length of 1.03–1.07 μm (first of all, fiber laser) on steels and alloys, as well as investigations of the physical fundamentals of manifestation of the synergic (hybrid) effect at such an impact and determination of the possibilities of its practical application. It was determined, in particular, that increase of the effectiveness of synergic effect manifestation is related to improvement of the plasma arc burning conditions in the zone of ionized vapour plume, which forms under the impact of focused laser radiation, as well as simplification of laser keyhole formation due to plasma arc pressure.

KEYWORDS: laser-plasma welding, synergic effect, process efficiency, steels, aluminium alloys, industrial application

INTRODUCTION

Ideas of hybrid application of the laser radiation and the electric arc for welding and related processes, proposed by W.M. Steen, became developed in theoretical and practical works of such prominent scientists as U. Dilthey, K. Paul, F. Ridel, I.V. Krivtsun and oth. Modern hybrid welding processes have become accepted by industry to a certain extent. For instance, they are applied in car- and shipbuilding, production of pipes of different diameters, etc. In the opinion of a number of researchers, laser-plasma welding is quite promising among other laser-arc processes. Therefore, the authors propose a review of its state-of-the-art to predict its further development.

PROBLEM DEFINITION

The authors of works [2–4] conducted analytical modeling of the processes of laser-plasma welding and spraying with application of models of integrated coaxial heads. In these works, higher efficiency of the coaxial laser-arc discharge was attributed to occurrence of a combined laser-arc discharge through absorption of the CO_2-laser beam, passing through the center of the arc column, by constricted-arc plasma. Here, the degree of laser radiation absorption by the arc plasma was indicated as a key parameter of discharge control. Such an approach mainly defined the principles of hybrid welding 20–30 years ago. Over the last 10–20 years CO_2 lasers have confidently replaced fiber lasers, the radiation of which practically does not interact with arc plasma [5]. This has significantly changed the way we look at the hybrid laser-plasma process and prospects for its industrial application. Modern approaches to development of welding and related laser-plasma technologies are based on application of radiation with wave length in the range of 1.03–1.07 μm, i.e. of fiber, disc and Nd:YAG-lasers.

PURPOSE AND OBJECTIVES OF RESEARCH

The objective of the work is to analyze the current state of the directions of investigations and industrial applications of laser-plasma welding processes and to assess the efficiency of manifestation of the synergic (hybrid) effect at application of laser radiation with 1.03–1.07 μm wave length.

The following tasks were solved to achieve this purpose:

- establishing modern directions of investigations of laser-plasma welding processes;
- determination of the efficiency of synergic effect manifestation in laser-plasma welding of steels and alloys;
- analysis of laser-plasma process impact on the characteristic welding defects in steels and alloys;
- analysis of the state-of-the-art of industrial application of laser-plasma welding.

ANALYSIS OF LITERATURE SOURCES

Already at the start of the XXI century acad. I.V. Krivtsun stated that the main factor for determination of the nature of metal penetration in combined laser-arc welding is the thermal and dynamic influence of the used heat sources on the weld pool surface. Therefore, he developed a system of equations to describe the process of metal evaporation under the impact of multicomponent plasma forming above the weld pool in laser-plasma welding [6]. Such a system is the base for calculation of the characteristics of thermal and dynamic influence of arc, laser or combined plasma on the welding pool surface in the respective gas-shielded welding processes. His next step was to study the features of metal penetration in laser-arc welding using Nd:YAG-laser [7]. A mathematical model of thermal processes developed for this purpose allowed calculating the penetration profiles at a combined influence of the laser beam and the electric arc on the product, taking into account their interaction on the metal surface. Calculations showed the presence of a synergic (hybrid) effect, which is manifested in a non-additive increase of the volume of metal remelted by laser-plasma process, compared to metal volumes, remelted separately by the laser and plasma processes.

In order to analyze the synergic combination effect, arising during the process, laser-plasma welding can be divided into three zones [8]: I — plasma above the surface; II — weld pool surface and III — interaction occurring directly under the surface. Such factors, as a common welding source, relative position of the laser and plasma sources, as well as the role and influence of welding parameters, have a major impact on the extent of synergic effect manifestation.

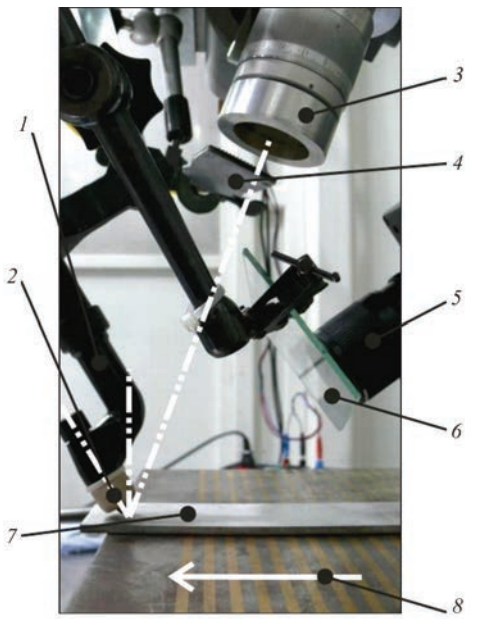

Figure 1. Experimental set-up with separate arrangement of the plasmatron and the laser beam [12]: *1* — plasma torch mounted at angle α = 35° (forward inclined); *2* — plasma nozzle (distance to sample *L* = 2 mm); *3* — laser beam directed at angle β = 20° (backward inclined); *4* — cross-jet (air knife); *5* — high-speed camera; *6* — protective glass; *7* — sample; *8* — direction of work table (sample) movement

In work [9] it is shown that the arc characteristics practically do not change in cases of interaction of "gas CO_2-laser – helium TIG arc" and "disc Yb:YAG-laser – argon TIG arc". The reason is that the inverse bremsstrahlung coefficients differ markedly, because of different electron density of argon and helium arcs and different wave lengths of CO_2 and Yb:YAG lasers. Such a study to a certain extent promotes partial application of the experience of the use of CO_2-laser in hybrid processes with solid-state laser radiation.

Work [10] presents the results of investigation of the synergic effect in hybrid laser–arc welding. Experiments were conducted with Nd:YAG-laser of power P_L = 500 W in combination with standard TIG-welding equipment. Two aspects were studied: heat transfer efficiency and melting efficiency. Heat transfer efficiency was determined by calorimetric measurements, and melting efficiency — by cross-sections of welds produced in different welding modes. Results show that laser-arc interaction does not lead to any noticeable change in heat transfer efficiency, but results in a significant increase in melting efficiency. Non-additive increase of the cross-sectional area of welds produced with addition of two heat sources (laser and arc) is indicative of the presence of a synergic effect and hybrid mode of welding.

Spectral analysis of the hybrid plasma plume and high-speed photographic analysis of the process in hybrid welding revealed the following. First, the principle of the synergy effect consists in that at interaction with the nonconsumable electrode constricted arc the laser transfers the electron energy to a higher level, and creates the conditions for quantum transition. Due to that more photons are emitted, which increase the heat input into the material being welded. The synergic effect is enhanced with increase of laser power and is decreased with the arc current. This effect is proportional to the weld cross-section, particularly in its upper part. Secondly, the amount of spatter at hybrid laser-arc welding is much smaller than in arc welding.

In work [12] a number of investigations of laser-plasma welding were conducted by the scheme in Figure 1. It is proposed to define welding efficiency η_W as a ratio of the theoretical power P_{FZ} required for melting the fusion zone material (*FZ* index), to the total input welding power P_W according to

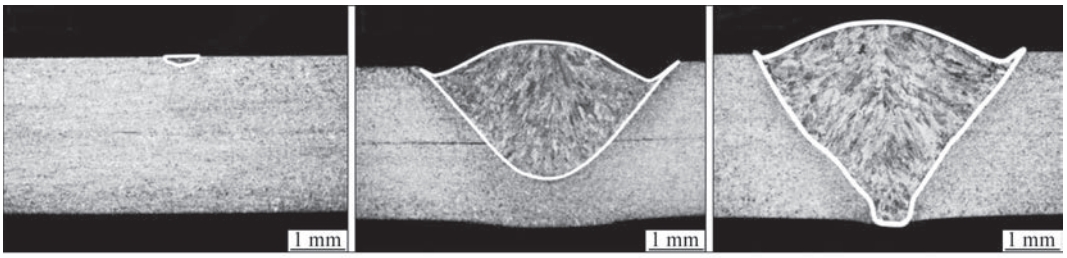

	Laser	Plasma		Laser–plasma
Energy combination efficiency, %	29.5	67.2	+9.9	71.6
Melting efficiency, %	5.8	10.6	+53.4	15.8
Thermal efficiency, %	1.7	7.1	+68.7	11.3

Figure 2. Transverse sections in welding AISI304 steel (δ = 1 mm) by the laser beam (P_L = 200 W, ω_0 = 200 μm), plasma welding (Q_p = 1.8 l/min; d_W = 5 mm) and laser-plasma welding (laser-plasma) (P_L = 200 W, ω_0 = 200 μm, Q_p = 1.8 l/min; d_W = 5 mm) with the respective efficiency values [14]

$$\eta_W = \frac{P_{FZ}}{P_W} = \frac{\rho w_{ch} A_{FZ} \Delta h_{FZ}}{P_W}, \quad (1)$$

where ρ is the density of the material being welded; w_{ch} is the movement speed; A_{FZ} is the cross-sectional area in the fusion zone, and Δh_{FZ} is the required increase of specific enthalpy for melting. Relationship (1) can be considered as the basis for determination of relative welding efficiency, which compares the efficiency of combined laser-plasma process with that of individual processes.

A change in arc voltage at introduction of laser radiation into the plasma-arc process can be one of the causes for improvement of laser-plasma welding efficiency compared to individual processes. In case of aluminium welding, a marked voltage drop in the range from –2 to –3 V is observed at switching on the laser beam. In welding steel under the same conditions of a highly focused laser beam, a moderate increase of arc voltage between 0.15 and 0.6 V was found. Calculations showed [12] that the efficiency of laser-plasma welding can change from 1.5 (for 6082 aluminium alloy) to 2.4 for AISI304 steel.

If the synergic effect of hybrid laser-arc treatment is interpreted as increase of energy transfer from the heat source to the material, then the thermal efficiency η_T of the process corresponds to the ratio of power P_U, which is required for melting the material being welded per a unit of time (without losses), to total applied power P_A [13]. In keeping with equation (2), this value can be divided into melting efficiency η_M (energy consumption within the base material) and energy combination efficiency η_C (energy input from the heat source), using power P_T, transferred from the heat source to the blank [13]:

$$\eta_T = \frac{P_U}{P_A} = \eta_M, \ \eta_C = \frac{P_U}{P_T}\frac{P_T}{P_A} \quad (2)$$

A method and model of efficiency determination were applied in work [14]. While the laser beam of power P_L = 200 W and focal point diameter of 200 μm barely melts the material, the process of plasma welding with arc power of about 2 kW reaches weld penetration through approximately 2/3 of the blank thickness for the applied set of parameters (Figure 2). A combination of both the processes provides complete penetration welding. While energy combination efficiency η_C rises by just ~10 % compared to arithmetic effectiveness of combining energy η_C of individual processes, melting efficiency η_M of the combined process is approximately 1.5 times higher than that of melting η_M of the plasma-arc process. It can be assumed that the heat flow in the weld pool, controlled by the conductive and/or convective transfer mechanisms, changes favourably to create the resulting cross-section of the weld with increased penetration due to more advantageous thermal and/or hydrodynamic boundary conditions. The authors of work [14] propose to regard it as a clear proof of the hypothesis that the secondary, i.e. thermal effects are responsible for synergic advantages of laser-arc treatment efficiency.

In work [15] it was determined that synergic effect manifestation depends on welding speed. At 2 m/min speed of welding AISI304 steel (δ = 4 mm) exceeding of the hybrid penetration cross-sectional area is equal to the sum of areas produced by laser and plasma processes (~2 kW each), and it reaches 30 %, while for 4 m/min speed it is ~20 %. In work [16] the quantitative evaluation of the synergic effect in laser-arc hybrid welding was performed using a dimensionless parameter of melting energy increment ψ:

$$\psi = \frac{S_H - (S_L + S_A)}{S_L + S_A} \cdot 100\%,$$

where S_H, S_L, S_A are the cross-sectional areas of welds in hybrid, laser and arc welding, respectively.

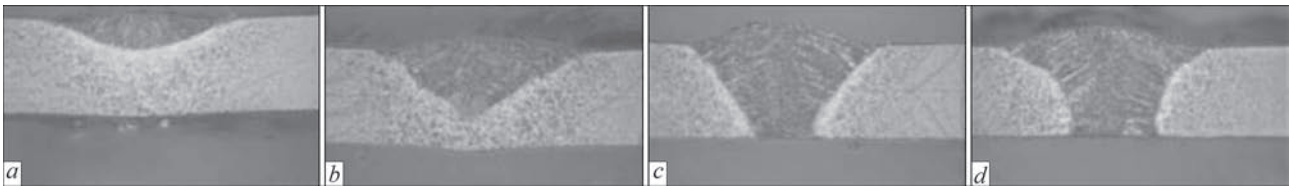

Figure 3. Penetration formation in sheets of S235JR steel 3 mm thick, due to a change of laser radiation power: *a* — 0; *b* — 200; *c* — 330; *d* — 440 W (unchanged parameters: I = 150 A; V = 1000 mm/min; Q_p = 0.8 l/min; L = 8 mm, β = 3°) [17]

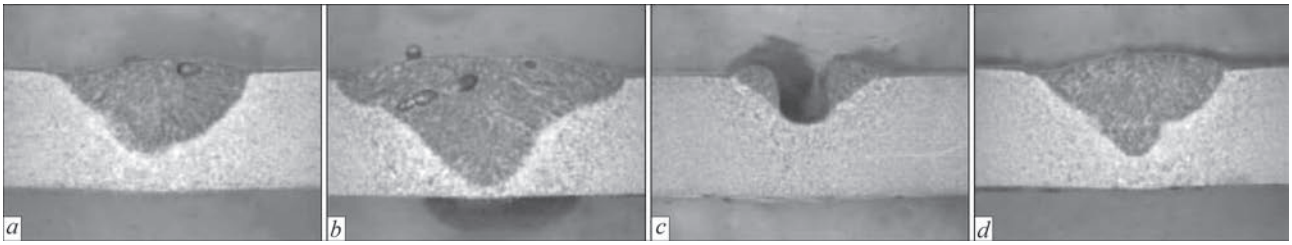

Figure 4. Penetration formation in sheets of S235JR steel 4 mm thick due to a change in laser radiation power: *a* — 0; *b* — 440; *c* — 0; *d* – 440 W and welding speed: *a, b* — 200; *c*, *d* — 250 mm/min (unchanged parameters: I = 150 A; Q_p = 0.4 l/min, L = 8 mm, β = 19°) [17]

The larger ψ value, the stronger is the synergic effect. It was calculated that in hybrid laser-TIG welding ψ = 59.3–83.6 %, and at laser-MIG welding ψ = 1–23 %. It can be anticipated that in case of constricted electric arc application in the hybrid process the synergic effect will be even greater than in laser-TIG welding [17]. For laser-plasma welding using Nd:YAG laser this effect can be evaluated by transverse microsections, given in Figures 3 and 4, in keeping with the specified mode parameters.

For realization of laser-plasma welding processes, the focused laser beam can be aimed at the point of interaction with the material at a certain angle, i.e. by the paraxial scheme (Figure 1) (for instance, [18]), or normal to the surface of the product being welded, i.e. by the coaxial scheme (for instance, [4, 19]). The nonconsumable electrode is usually inclined at a certain (minimal possible) angle to the focused laser beam axis [20]. Filler wire can be fed in the direction towards the plasma jet or not fed at all. Metal and alloy powders can be also used as filler materials [21, 22]. Influence of arc current predominantly ensures upper bead formation, while laser radiation power is responsible for penetration depth.

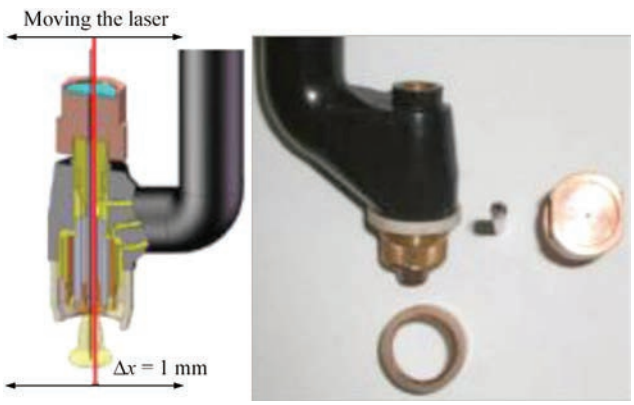

Figure 5. Head for laser-plasma microwelding and cutting of thin metals (radiation power of 100 W, welding current of 40 A) [24]

To achieve the greatest effect from simultaneous application of the laser and plasma, specialists of the Institute for Production Technology together with specialists of the Institute for Material and Beam Technology (Dresden, Germany) developed a hybrid laser-plasma head, designed for up to 100 W radiation power and up to 40 A welding current (Figure 5) [23–26]. During investigation of stainless steel welding by this method it was found [25] that laser beam activation causes an abrupt drop of arc voltage by approximately 1 V (Figure 6, *a*). This phenomenon was observed only in the case of low arc currents. For higher arc currents this effect disappeared (Figure 6, *b*).

In work [26] it was found that under stable arc burning conditions the measured voltage drop after laser beam activation (100 W), is closely related to shifting of the arc impact zone from the position behind the beam focal point to a point irradiated by the laser. In the case of a pure plasma process, the arc is deflected backwards, and the anode region evidently lags behind the arc column axis (Figure 7, *a*). In the case of a variant with laser radiation, this lagging behind becomes smaller, and the arc anode region is stably rooted in the beam focusing zone (Figure 7, *b*). At the same time, an increase of arc voltage by 0.4–0.6 V was observed. The authors of work [26] believe that the main mechanism of arc stabilization should be the surface effect, which is unrelated to changes in arc plasma volume properties, either through direct interaction of laser radiation and arc plasma, or due to a possible change of plasma composition as a result of laser-induced evaporation.

In work [27] a mathematical model was proposed, which showed the potential of laser-plasma process

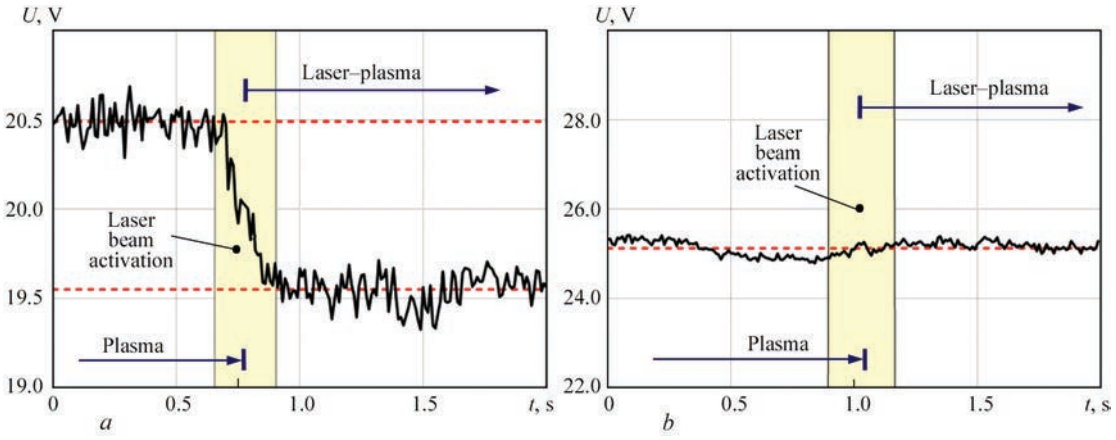

Figure 6. Arc voltage during bead deposition on a plate from AISI304 stainless steel with laser beam support and without it under different welding conditions: *a* — arc current I = 40 A; laser power P = 100 W, welding speed V = 0.75 m/min and sheet thickness δ = 1 mm; *b* — arc current I = 160 A; laser power P = 400 W, welding speed V = 2.00 m/min and sheet thickness δ = 3 mm [25]

in terms of peculiarities of the influence of hybrid thermal cycles on the material microstructure. The model was verified by experiments on laser welding of car body steels. Work [28] describes laser-plasma welding of low-carbon steel plates 6 mm thick at up to 5 kW laser power and up to 150 A arc current, which ensured a 100 % increase of the speed of complete penetration welding or increase of penetration depth by 25–100 %, compared to application of just the laser. It was also found that complete penetration in laser-plasma welding leads to considerable energy losses, because of its release through the keyhole root. All the advantages of the hybrid process are revealed only when the keyhole root is enclosed (in the blank).

Numerical study of the temperature field during 3D printing of thin-walled metal parts by hybrid laser-plasma method shows that the temperature gradient directly determines the grain growth rate in the HAZ of the built-up wall [29]. In work [30] a real-time observation of the parameters of the vapour-gas channel and the weld pool at laser and laser-arc welding was performed. Authors of works [31, 32] showed the good prospects for application of hybrid laser-plasma welding method for joining thin sheet (up to 3–4 mm) stainless steels of austenitic and ferritic grades without filler material application.

In work [33] it was established that in laser-microplasma welding of 7075 alloy (δ = 1.5 mm) the volume fraction of remelted metal defects in the form of pores of 15–25 μm size decreases, compared to microplasma welding, to the level characteristic for laser welding (~5 %). Remelted metal hardness decreases by 15–20 % at HAZ metal hardness close to that of the base metal. For comparison, in the laser process the remelted metal hardness is decreased by ~15 %, and in the microplasma process it is ~30 % (relative to base metal). Obtained data confirm the advantage of the laser-microplasma process, proved in [34]. This method reduces the use of laser energy to 40–50 %, the time of weld pool existence (0.03–0.05 s) becomes close to laser welding, and the risk of alloying element burn-out is eliminated.

The laser-plasma method of material treatment can be used for thermal surface modification, alongside the welding processes, in particular for alloying. In work [35] it is shown that the modes of laser-plasma alloying promote an increase of strength characteristics (by 20 % on average), compared to laser alloying. In work [36] the influence of concentrated energy flows on the materials is considered in the case of laser-plasma hardening, and the possibility of nanostructured layer formation is established. Superthin coatings can be deposited on the part working

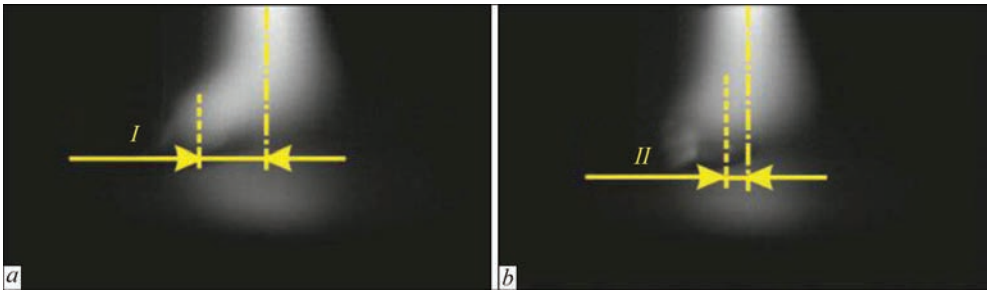

Figure 7. Arc shape before (*a*) and after (*b*) beam activation: I = 40 A; P = 100 W, V = 1 m/min; material is AISI304 stainless steel (δ = 1 mm) [26]

surfaces by an optical pulsed discharge, created by laser-plasma method [37]. In work [38] it is shown that at plate surface exposure to a laser heat source, an intensive subsurface melt flow (~50 cm/s) forms in the molten zone, owing to the dominating impact of the thermocapillary force, generated as a result of a high temperature gradient (~7000 °C/cm) on the metal pool free surface. This flow, directed from the pool axial part towards the melting front, intensifies energy transfer from the pool overheated axial portion to its periphery region, and promotes widening of the melted zone. Influence of convective stirring of the pool on penetration depth is essentially smaller due to a predominantly subsurface melt flow.

DISCUSSION OF THE RESULTS OF LITERATURE SOURCE ANALYSIS

Welding of steels and alloys by highly concentrated heat sources can lead to formation of such characteristic defects as hot cracks, internal pores, softening of the near-weld zone, weld sagging, undercuts and irregular nature of reinforcement bead formation [15, 33, 39]. One of the advanced methods to eliminate the above defects is application of hybrid laser-arc and laser-plasma welding processes [39]. In laser-plasma welding the penetration depth and root bead formation are predominantly ensured by the laser component, and elimination of undercuts and formation of the upper bead are provided by the plasma component [15].

One of the more important aspects of laser welding with deep penetration is formation and containment of the laser vapour-gas channel — the so-called keyhole [40]. The influence of the plasma-component in laser-plasma welding can be assessed by Figure 4, *c*. From this Figure one can see that even in the absence of laser radiation the arc plasma creates a certain sagging due to its own pressure on the weld pool liquid metal, which is a certain keyhole nucleus [17]. It is obvious that in the case of laser radiation penetration to this liquid metal sagging, the conditions for keyhole formation are greatly improved. It can be assumed that formation of the synergic (hybrid) effect in the case of application of laser radiation with λ = 1.03–1.07 μm, occurs both through improvement of laser radiation absorption by liquid metal, molten by the plasma source, and due to formation of weld pool metal sagging under the plasma source impact.

According to the results of high-speed filming described in work [26] (Figure 8), after activation of focused laser radiation, the plasma arc is shortened due to approaching the zone of the laser plume ionized by metal evaporation (i.e. more electrically conductive zone). It promotes a shortening of the plasma arc and arc voltage drop described in work [26]. In the case of plasma arc immersion into the laser keyhole, its elongation can occur, which will lead to a certain increase of arc voltage.

In case of application of laser-plasma powder hybrid welding, energy losses for heat removal into the filler material are eliminated [22]. It promoted introduction of such a technology into shipbuilding [41]. Laser-plasma welding without filler material application is actively used in automotive manufacturing [42]. It is applied for manufacturing tailor welded blanks, overlap welding of zinc-coated steel (with a gap), welding using additional material. Welding of stainless tubes is an example of industrial application of laser-plasma welding without filler material [43].

The future of laser-plasma welding as an independent process is associated with development of an integrated head, which combines two energy sources by a coaxial scheme [42]. One of the examples of such an integrated welding head is the coaxial head shown in Figure 8, *a*, which was developed at the Bremen Institute of Applied Beam Technology (Germany) [44]. This head was later upgraded and fitted with a system of filler wire feed (Figure 8, *b*) [45]. Another example,

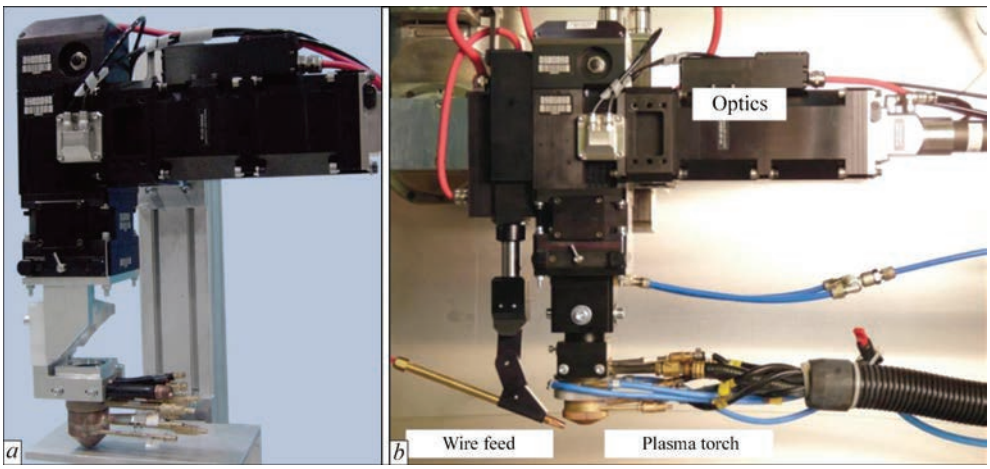

Figure 8. Integrated head for laser-plasma welding: without (*a*) [44] and with (*b*) [45] filler wire feed

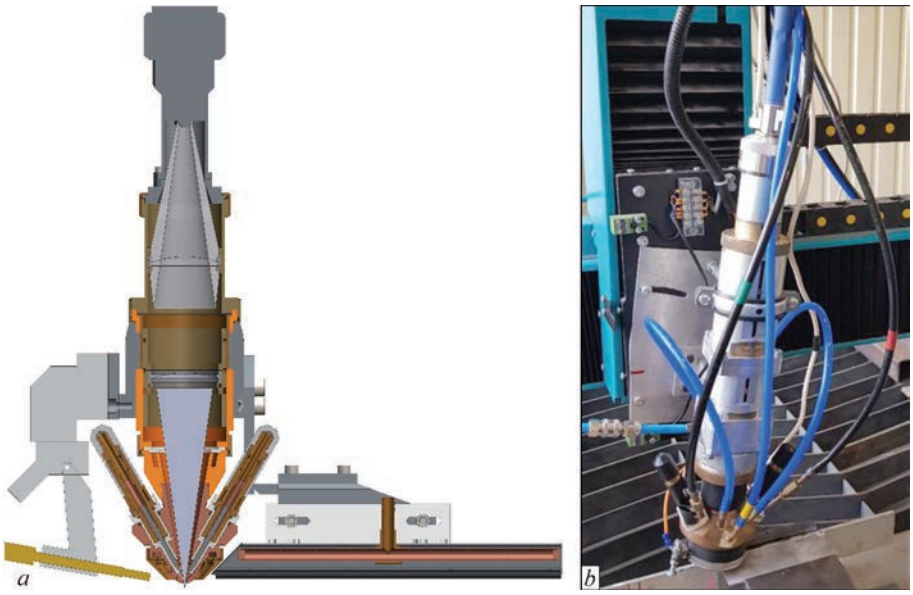

Figure 9. 3D-model (*a*) and appearance (*b*) of the head for laser and laser-plasma welding, developed at PWI [46]

developed at PWI, is the coaxial head for laser-plasma welding (Figure 9) [46].

Conducted analysis of literature data allows defining the following main advantages of the hybrid laser-plasma process, compared to laser one:

- simultaneous use of laser and plasma energy allows reducing the laser power and lowering the equipment cost (estimated up to 40–50 %);
- plasma component of laser-plasma welding allows lowering the requirements to preparation and fitup of the edges to be welded and removing the oxide film (for aluminium alloys);
- improvement of productivity due to increase of welding speed;
- reducing energy consumption of the process due to increase of its efficiency;
- widening of the deposited bead in laser-plasma surfacing and increase of penetration depth in welding due to a change in hydrodynamic flows in the weld pool.

Further prospects for development of laser-plasma welding and related processes are associated with application of fiber lasers (λ = 1.07 μm), as the most accessible ones for a wide range of users [47]. The plasma component characteristics are related to the metal being welded (straight polarity for steels and multipolar asymmetrical current for aluminium alloys) [48]. Compared to laser welding, laser-plasma process promotes lowering of the requirements to edge preparation, and compared to plasma welding it lowers the residual deformations [49]. Considering an increase in productivity, one can anticipate tendencies of separate laser and plasma welding processes being replaced by laser-plasma welding in industry. Due to ensuring rather high speeds (up to 10 m/min and higher), laser-plasma welding can be used for small-scale production of such thin-walled products and structures from steels and alloys, as regular and profile pipes, body elements of automotive and railway transport, products for food and chemical industry, etc.

One can assume that it is rational to predominantly focus further investigations of laser-plasma welding on relative influence of the radiation of fiber laser and constricted arc on steels and alloys. The prospect here is revealing the features, advantages and disadvantages of such a process with the purpose of establishing the limits of synergic effect manifestation, possibilities for enhancing it and ways to further use this effect.

CONCLUSIONS

1. Current directions of investigation of laser-plasma welding processes are focused predominantly on studying the features of simultaneous impact on steels and alloys of the constricted arc plasma and laser radiation with wave length of 1.03–1.07 μm (first of all, fiber laser), as well as studying the physical fundamentals of the synergic (hybrid) effect manifestation under such an impact, and determination of its possible practical applications. It was determined, for instance, that promotion of the synergic effect manifestation is associated with improvement of the plasma arc burning conditions in the zone of ionized vapour plume, which forms under the impact of focused laser radiation, as well as facilitation of laser keyhole formation due to plasma arc pressure.

2. It was proposed to define the effectiveness of the synergic effect manifestation in laser-plasma welding of steels and alloys as the ratio of the theoretical magnitude of power required for melting the weld material, to the total input welding power, or as a ratio of the cross-sectional area of the laser-plasma process weld

to the sum of the cross-sectional areas of welds, made separately by plasma and laser welding. It was established that the efficiency of laser-plasma welding can vary from 1.5 to 2.4.

3. Application of laser-plasma welding allows prevention of such defects characteristic for laser and plasma welding of high-strength steels and alloys as hot cracks, internal pores, near-weld zone softening, weld sagging, undercuts and irregular formation of the reinforcement bead.

4. Industrial application of high-speed laser-plasma welding is associated with reduction of laser energy (to ~50 %, compared with laser welding), lowering of the requirements to preparation and fit-up of the edges to be welded, increase of welding speed, and minimizing the process energy input. This technology has a considerable potential for industrialization in large-scale productions of thin-walled products and structures (first of all, from stainless steels, titanium and aluminium alloys), such as structures from regular and profile pipes, body elements of railway transport, extended welded panels of aviation and sea transport, critical structures of equipment for food and chemical industry, etc.

REFERENCES

1. Steen, W.M., Eboo, M. (1979) Arc augmented laser welding. *Metal Construction*, 11(**7**), 332–335.
2. Gvozdetsky, V. S., Krivtsun, I. V., Chizhenko, M. I. et. al. (1995) *Laser-arc discharge: Theory and application. Welding and Surfacing Rev. 3*, Harwood.
3. Krivtsun, I.V., Chizhenko, M.I. (1997) Principles of calculation of laser-arc plasmatrons. *Avtomatich. Svarka,* **1**, 16–23 [in Russian].
4. Dykhno, I.S., Krivtsun, I.V., Ignatchenko, G.N. (1997) *Combined laser and plasma arc welding torch.* Pat. US 5700989.
5. Quintino, L., Costa, A., Miranda, R. et al. (2007) Welding with high power fiber lasers — A preliminary study. *Materials & Design*, 28(**4**), 1231–1237. DOI: https://doi.org/10.1016/j.matdes.2006.01.009
6. Krivtsun, I.V. (2001) Model of evaporation of metal in arc, laser and laser-arc welding. *The Paton Welding J.,* **3**, 2–9.
7. Krivtsun, I.V. (2001) Peculiarities of penetration of metal in laser-arc welding using YAG-laser. *The Paton Welding J.,* **12**, 29–32.
8. Zhiyong, L., Srivatsan, T.S., Yan, L. et. al. (2013) Coupling of laser with plasma arc to facilitate hybrid welding of metallic materials: A review. *J. Mater. Eng. and Performance*, 22(**2**), 384–395. DOI: https://doi.org/10.1007/s11665-012-0280-6
9. Shikai, Wu, Rongshi, Xiao (2015) Effect of high power CO_2 and Yb:YAG laser radiation on the characteristics of TIG arc in atmospherical pressure argon and helium. *Optics & Laser Technology,* **67**, 169–175. DOI: https://doi.org/10.1016/j.optlastec.2014.10.018
10. Hu, B., den Ouden, G. (2005) Synergetic effects of hybrid laser/arc welding. *Sci. and Technol. of Welding & Joining*, 10(**4**), 427–431. DOI: https://doi.org/10.1179/174329305X44170
11. Zhang, C., Gao, M., Zeng, X. (2019) Influences of synergy effect between laser and arc on laser-arc hybrid welding of aluminum alloys. *Optics & Laser Technology*, **120**, 105766. DOI: https://doi.org/10.1016/j.optlastec.2019.105766
12. Mahrle, A., Schnick, M., Rose, S. et. al. (2011) Process characteristics of fibre-laser assisted plasma arc welding. *Phys. D: Appl. Phys*. **44**, 345502. DOI: 10.1088/0022-3727/44/34/345502
13. Hipp, D., Mahrle, A., Jäckel, S. et. al. (2018) Füssel U. Method for high accuracy measurements of energy coupling and melting efficiency under welding conditions. *J. of Laser Applications*, **30**, 032414. DOI: https://doi.org/10.2351/1.5040615
14. Hipp, D., Mahrle, A., Beyer, E. et. al. (2019) Thermal efficiency analysis for laser-assisted plasma arc welding of AISI 304 stainless steel. *Materials*, **12**, 1460. DOI: https://doi.org/10.3390/ma12091460
15. Korzhyk, V.M., Khaskin, V.Yu., Grynyuk, A.A. et al. (2021) Features of laser-plasma welding of corrosion-resistant steel AISI 304 with laser application. *The Paton Welding J.,* **12**, 9–17. DOI: https://doi.org/10.37434/tpwj2021.12.02
16. Meng, Y., Gao, M., Zeng, X. (2018) Effects of arc types on the laser-arc synergic effects of hybrid welding. *Optics Express*, 26(**11**), 14775–14785. DOI: https://doi.org/10.1364/OE.26.014775
17. Emmelmann, C., Kirchhoff, M., Petri, N. (2011) Development of plasma-laser-hybrid welding process. *Physics Procedia*, **12**, 194–200. DOI: https://doi.org/10.1016/j.phpro.2011.03.025
18. Walduck, R.P. (1999) *Enhanced Laser Beam Welding*. Pat. US 5866870.
19. Dykhno, I., Ignatchenko, G., Bogachenkov, E. (2002) *Combined laser and plasma-arc processing torch and method*. Pat. US 6388227.
20. Kim, C.H., Ahn. Y.H., Kim, J.H. (2011) CO_2 Laser-micro plasma arc hybrid welding for galvanized steel sheets. *Transact. of Nonferrous Metals Society of China*, 21(**1**), 47–53. DOI: https://doi.org/10.1016/S1003-6326(11)61059-5
21. Stelling, K., Lammers, M., Schobbert, H. et al. (2006) Qualification of Nd:YAG and CO_2 laser plasma hybrid welding with filler material powder. *Welding and Cutting*, 5(**6**), 330–334.
22. Stelling, K., Schobbert, H., Kannengiesser, Th. et. al. (2005) Vertical-up and -down laser plasma powder hybrid welding of a high nitrogen austenitic stainless steel. *Welding in the World*, 49(**5–6**), 45–49.
23. Rose, S., Mahrle, A., Schnick, M. et. al. (2013) Plasma welding with a superimposed coaxial fiber laser beam. *Welding in the World*, 57(**6**), 857–865. DOI: https://doi.org/10.1007/s40194-013-0079-6
24. Beyer, E., Standfuss, J. (2012) Innovations in laser welding using high brightness lasers. In: *Proc. of the Conf. on Heriot-Watt IMRC (26th June 2012, Edinburgh)*.
25. Mahrle, A., Rose, S., Schnick, M. et. al. (2013) Laser-assisted plasma arc welding of stainless steel. *J. of Laser Applications*, **25**, 032006. DOI: https://doi.org/10.2351/1.4798338
26. Mahrle, A., Rose, S., Schnick, M. et. al. (2013) Stabilisation of plasma welding arcs by low power laser beams. *Sci. and Technol. of Welding & Joining*, 18(**4**), 323–328. DOI: https://doi.org/10.1179/1362171813Y.0000000109
27. Turichin, G., Lopota, V., Valdaitseva, E. et. al. (2007) Peculiarity of phase transformation kinetics and control of material microstructure formation during laser hybrid welding. *Laser Technologies in Welding and Materials Processing.* Kyiv, PWI, NASU, 126–130.
28. Swanson, P.T., Page, C.J., Read, E. et. al. (2007) Plasma augmented laser welding of 6 mm steel plate. *Sci. and Technol. of Welding & Joining*, 12(**2**), 153–160. DOI: https://doi.org/10.1179/174329307X164283
29. *Fanrong* Kong, Haiou Zhang, Guilan Wang. (2009) Modeling of Thermal-metallurgical Behavior during Hybrid Plasma-la-

ser Deposition Manufacturing. In: *Progress in Electromagnetics Research Sym. (Beijing, China, March 23–27)*, 946–953.
30. Turichin, G.A., Tsybulsky, I.A., Zemlyakov, E.V. et al. (2009) On monitoring system of laser-arc welding. *Metalloobrabotka,* **6**, 46–48 [in Russian].
31. Sidorets, V.N., Bushma, A.I., Khaskin, V.Yu. (2012) Prospectives of application of hybrid laser-plasma welding of stainless steels in machine-building. *Visnyk DDMA,* 28(**3**), 244–246 [in Russian].
32. Krivtsun, I.V., Bushma, A.I., Khaskin, V.Yu. (2013) Hybrid laser-plasma welding of stainless steels. *The Paton Welding J.,* **3**, 48–50.
33. Korzhyk, V., Khaskin, V., Grynyuk, A. (2022) Comparison of the features of the formation of joints of aluminum alloy 7075 (Al–Zn–Mg–Cu) by laser, microplasma, and laser-microplasma welding. *Eastern-European J. of Enterprise Technologies*, 115(**1–12**), 38–47. DOI: https://doi.org/10.15587/1729-4061.2022.253378
34. Krivtsun, I.V., Shelyagin, V.D., Khaskin, V.Yu. (2007) Hybrid laser-plasma welding of aluminium alloys. *The Paton Welding J.,* **5**, 36–40.
35. Markashova, L.I., Shelyagin, V.D., Kushnaryova, O.S. et al. (2015) Effect of technological parameters of laser and laser-plasma alloying on properties of 38KhN3MFA steel layers. *The Paton Welding J.,* **5–6**, 124–129.
36. Repkin, D.A., Melyukov, V.V., Gusakov, A.K. et al. (2013) Determination of action mode by concentrated energy flows on material using inverse problem method. *Vestnik Nizhegorodskogo Un-ta,* 2(**2**), 88–91 [in Russian].
37. Bagaev, S.N., Grachev, G.N., Smirnov, A.L. et al. (2014) Application of laser-plasma method of surface modification of metals for improving of tribotechnical characteristics of internal combustion engine cylinders. *Obrabotka Metallov,* 62(**1**), 14–22 [in Russian].
38. Borisov, Yu.S., Demchenko, V.F., Lesnoj, A.B. et al. (2013) Numerical modeling of heat transfer and hydrodynamics in laser-plasma treatment of metallic materials. *The Paton Welding J.,* **4**, 2–7.
39. Peleshenko, S.I., Khaskin, V.Yu., Korzhyk, V.M. et al. (2022) Features of welding high-strength alloys based on aluminium and beryllium using highly-concentrated heat sources (Review). *The Paton Welding J.,* **12**, 9–18. DOI: DOI: https://doi.org/10.37434/tpwj2022.12.02
40. Svenungsson, J., Choquet, I., Kaplan, A. (2015) Laser welding process – A review of keyhole welding modelling. *Physics Procedia*, 78, 182–191. DOI: https://doi.org/10.1016/j.phpro.2015.11.042
41. Shishov, A.Yu., Tretyakov, R.S., Tretyakov, E.S. (2012) Prospects of development of laser-plasma welding technology for large thick products in shipbuilding using powder filler material. *Inzhenernyj Zhurnal: Nauka i Innovatsii,* **6**, 146–152. https://rucont.ru/efd/274958
42. Page, C. J., Devermann, T., Biffin, J. et. al. (2002) Plasma augmented laser welding and its applications. *Sci. and Technol. of Welding & Joining*, 7(**1**), 10–15. DOI: https://doi.org/10.1179/136217102225001313
43. Yoon, S.H., Hwang, J.R., Na, S.J. (2007) A study on the plasma-augmented laser welding for small-diameter STS tubes. *Int. J. Adv. Manuf. Technol.*, **32**, 1134–1143. DOI: https://doi.org/10.1007/s00170-006-0436-3
44. *Lasertechnik* aktuell (2007) *Bremer Institut für angewandte Strahltechnik Bulletin,* **2**.
45. Möller, F. (2016) *Wechselwirkung zwischen Lichtbogen und Laserstrahl bei Aluminium. Strahltechnik*, **59**, Bremen: BIAS Verlag.
46. Peleshenko, S., Kvasnytskyi, V., Khaskin, V. et. al. (2022) Features of physical and metallurgical processes during welding of thin-walled aluminum alloy structures using laser radiation. *Danish Scientific J.*, **65**, 50–59. DOI: https://doi.org/10.5281/zenodo.7271299
47. Bernatskyi, A., Khaskin, V. (2021) The history of the creation of lasers and analysis of the impact of their application in the material processing on the development of certain industries. *History of Science and Technology*. 11(**1**), 125–149. DOI: https://doi.org/10.32703/2415-7422-2021-11-1-125-149
48. Shelyagin, V.D., Krivtsun, I.V., Borisov, Yu.S. (2005) Laser-arc and laser-plasma welding and coating technologies. *The Paton Welding J.,* **8**, 44–49.
49. Korzhyk, V., Bushma, O., Khaskin, et. al. (2017) Analysis of the current state of the processes of hybrid laser-plasma welding. In: *Proc. of the 2nd Int. Conf. on Mechanics, Materials and Structural Engineering (ICMMSE 2017)*. *Advances in Engineering Research*, **102**, 80–90. DOI: https://doi.org/10.2991/icmmse-17.2017.14

ORCID

V.M. Korzhyk: 0000-0001-9106-8593,
V.Yu. Khaskin: 0000-0003-3072-6761,
E.V. Illyashenko: 0000-0001-9876-0320,
S.I. Peleshenko: 0000-0001-6828-2110,
A.A. Grynyuk: 0000-0002-6088-7980,
O.A. Babych: 0000-0001-5633-5721,
A.O. Alyoshin: 0000-0001-9696-6800,
O.M. Voitenko: 0000-0003-4946-6517

CONFLICT OF INTEREST

The Authors declare no conflict of interest

CORRESPONDING AUTHOR

V.M. Korzhyk
E.O. Paton Electric Welding Institute of the NASU
11 Kazymyr Malevych Str., 03150, Kyiv, Ukraine.
E-mail: vnkorzhyk@gmail.com

SUGGESTED CITATION

V.M. Korzhyk, V.Yu. Khaskin, E.V. Illyashenko, S.I. Peleshenko, A.A. Grynyuk, O.A. Babych, A.O. Alyoshin, O.M. Voitenko (2024) Hybrid laser-plasma welding: efficiency and new possibilities (Review). *The Paton Welding J.*, **1**, 13–21.

JOURNAL HOME PAGE

https://patonpublishinghouse.com/eng/journals/tpwj

Received: 06.09.2023
Received in revised form: 17.11.2023
Accepted: 16.01.2024

DOI: https://doi.org/10.37434/tpwj2024.01.03

IMPACT OF HEAT TREATMENT ON MECHANICAL PROPERTIES OF JOINTS DURING ELECTRON BEAM WELDING OF 2219 ALLOY

V.V. Skryabinsky, V.M. Nesterenkov, M.O. Rusynyk

E.O. Paton Electric Welding Institute of the NASU
11 Kazymyr Malevych Str., 03150, Kyiv, Ukraine

ABSTRACT

Plates of 2219 alloy of 40 mm thickness were joined by electron beam welding. The effect of sequence of welding and heat treatment operations on the mechanical properties of the joints and distribution of hardness in the HAZ were studied. It was established that the plates of 2219 alloy that were quenched before welding and artificially aged after welding, have the highest strength. Aging improves the ultimate strength of the joints from 300–315 to 385–395 MPa, and hardness of the weld and HAZ metal increases by 5–10 *HRB*. In the study of the joint microstructure it was found that a region of high-temperature recovery of the hardened state is located at a distance of about 1.0 mm from the fusion line in the HAZ. It is characterized by an increase in hardness after aging to the level of base metal hardness. Measuring the welding thermal cycles it was found that the maximum heating temperature of this region is about 590 °C. Next the annealing region is located. In this region, a decrease in the metal hardness by 2–3 *HRB* is observed. For welding speed of 20 mm/s, the HAZ width is about 8 mm.

KEYWORDS: electron beam welding, aluminium alloy, welded joints, heat treatment, mechanical properties, ultimate strength

INTRODUCTION

2219 alloy of Al–6Cu alloying system is a heat-hardenable alloy, the maximal mechanical properties of which are achieved after quenching and artificial aging. Due to its excellent mechanical properties, corrosion resistance and weldability, it has been used to produce welded structures for more than 50 years now. However, improvement of welded joint quality and stability of their mechanical properties still remain a relevant task [1, 2]. Nonconsumable electrode argon-arc welding is usually used to join thin blanks of 2219 alloy, and over the recent decades friction stir welding has become widely accepted. Electron beam welding is used to join thick parts.

With any fusion welding process, welded joint strength will be lower than that of the base metal. This is related to the presence of a region of remelted metal and HAZ adjacent to it. Postweld heat treatment of the joints is performed to improve the joint strength.

Mechanical properties of 2219 alloy welded joints depend not only on heat treatment temperature and time, namely on the sequence of quenching, artificial aging and welding performance. Maximal mechanical properties of welded joints are achieved by conducting full postweld heat treatment (quenching and aging). Such an effect of strength increase is observed both for welding of quenched and artificially aged [3], and annealed semi-finished products [4]. In those cases, when large-sizes products are welded, and it is impossible or difficult to quench them, only artificial aging is performed after welding. In work [5] it is shown that postweld artificial aging improves the structure and mechanical properties of welded joints.

In welding aluminium alloys, there is a certain correlation between metal strength and hardness, which, in their turn, are determined by its structure [6]. Artificial aging after welding helps revealing the nature of structural transformations and state of the solid solution in the HAZ in such alloys. The degree of HAZ metal strengthening at artificial aging allows determination of the regions of high-temperature recovery of the quenched state, degree of annealing and presence of low-temperature recovery [7]. Changes in the metal structure in these regions will be visible in microsections, and measurement of welding thermal cycles allows determination of temperatures, at which these changes occur [8].

OBJECTIVE OF THE WORK

The objective of the work is to determine the sequence of quenching, artificial aging and welding operations, at which maximal mechanical properties of welded joints on large-sized products from 2219 aluminium alloy plates are achieved.

MATERIALS AND INVESTIGATION PROCEDURE

The nature of weld formation, hardness distribution in the welded joint cross-section, macro- and microstructure in the metal of the weld and HAZ, as well

Table 1. Chemical composition of 2219 alloy

Weight fraction of chemical elements, %								
Al	Cu	Mn	Mg	Fe	Si	Zn	Zr	Ti
Base	5.8–6.8	0.2–0.4	0.02	0.3	0.2	0.1	0.1–0.25	0.02–0.1

Table 2. EBW mode parameters

Welding speed, mm/s	Accelerating voltage, kV	Welding current, mA	Focus	Scan pattern	Beam scanning amplitude, mm	Beam scanning frequency, Hz
20	60	440	Sharp	Circle	0.5	630

as mechanical properties of the joints were studied. Investigations were conducted on 2219 alloy plates 40 mm thick. State of delivery is T-351 (quenching + mechanical deformation + natural aging). The alloy chemical composition is given in Table 1.

Welding was conducted in UL-209M unit with power supply from ELA 60/60 source with 60 kV accelerating voltage. Welding mode parameters (Table 2) were selected so as to ensure complete penetration of the butt in one pass with formation of weld reinforcement and reverse bead.

Hardness of the weld and HAZ metal was measured by Rockwell instrument with load on the steel sphere $P = 600$ N. Hardness measurements of the metal of the weld and HAZ were conducted on transverse sections for four variants of the sequence of welding and heat treatment operations: *1* — quenching — artificial aging — welding; *2* — quenching — artificial aging — welding — artificial reaging; *3* — annealing — welding; *4* — annealing — welding — artificial aging.

Electron beam is a linear heat source and, therefore, the temperature across the plate thickness is regarded to be stable. In this case, the thermal cycles in EBW of 40 and 10 mm plates will coincide. In order to simplify the experiments, the thermal cycles were recorded at EBW of 2219 alloy plates of 10 mm thickness. An EBW mode was selected, which at welding speed of 20 mm/s, ensured producing a 2 mm wide weld with parallel fusion boundaries.

Temperature on the plate surface was measured by chromel-alumel thermocouples, made from 0.1 mm wires. Thermocouple junctions were caulked into a recess on the plate surface at 2, 4 and 6 mm distance from the weld axis, which at 2 mm weld width was equal to 1, 3 and 5 mm from the fusion line, respectively. Thermocouple readings were recorded by a high-speed recording voltmeter with 100 mm/s speed of tape pulling.

Welded joint structure was revealed by electrolytical polishing and additional chemical etching in 25 % aqueous solution of fluoric acid. The microstructure was examined in an optical metallographic microscope Neophot-32, fitted with Olympus C-500 digital camera.

Mechanical properties of the samples were studied for three variants of the sequence of welding and heat treatment operations: *1* — quenching — artificial aging — welding; *2* — quenching — artificial aging — welding — artificial reaging; *3* — quenching — welding — artificial aging. Artificial aging was conducted at the temperature of 175±5 °C for 19 h with cooling in air.

Ultimate strength was determined by tensile testing of standard round samples with 4 mm diameter of the working part. Impact bend testing was performed on Charpy samples with a notch in the weld metal. Samples for testing were cut out across the weld, placing the weld in the sample center.

INVESTIGATION RESULTS AND THEIR DISCUSSION

Transverse section of a joint of 2219 alloy plates is shown in Figure 1. During welding, formation of weld reinforcement and reverse bead was guaranteed (Figure 2). EBW process proceeded without liquid metal splashing. Slight spatter was observed from the weld root side.

Welding mode ensured producing narrow welds of approximately 2.0 mm width with parallel fusion boundaries. Such a shape of the weld promotes reduction of residual welding deformations of the structure.

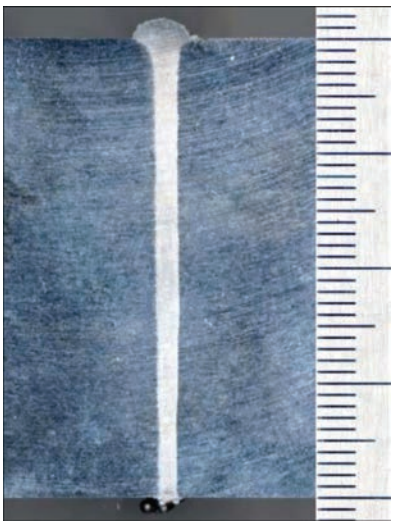

Figure 1. Transverse section of a joint of 2219 alloy plates 40mm thick

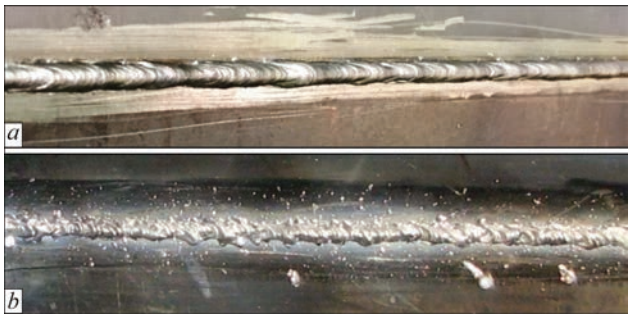

Figure 2. Appearance of the weld of a joint of 2219 alloy plates 40 mm thick from the side of electron beam entrance (*a*) and exit (*b*)

Results of welded joint hardness measurements are shown in Figure 3. Base metal hardness in the quenched and aged states is equal to 96 *HRB*, and weld metal hardness is 73 *HRB*. One can see that metal hardness at 1.0 mm distance from the fusion line is by 1–2 *HRB* higher than that of metal hardness at 2.0–3.0 mm distance from the weld. Artificial aging of the joints after welding increases weld metal hardness by 10 *HRB*, and metal hardness in the HAZ rises by 3–5 *HRB*. After welding, HAZ width is equal to approximately 8 mm.

When welding annealed plates, weld metal hardness (Figure 4) is on the level of base metal hardness (72–73 *HRB*), and the HAZ metal located at 1.0 mm distance from the fusion line shows the highest hardness. When moving away from the fusion line, metal hardness becomes lower. Artificial aging of welded joints strengthens the weld and HAZ metal, and their hardness here increases by 5–10 *HRB*.

Changes in HAZ metal hardness are the consequence of metallurgical processes, proceeding in the metal under the impact of welding thermal cycle. The welding thermal cycles were recorded, in order to determine the temperatures, at which these changes occur. Experimentally obtained characteristic curves of temperature change during heating and cooling under the impact of the welding thermal cycle are shown in Figure 5. Maximal heating temperatures for points located at 2.0, 4.0 and 6.0 mm distance from the weld

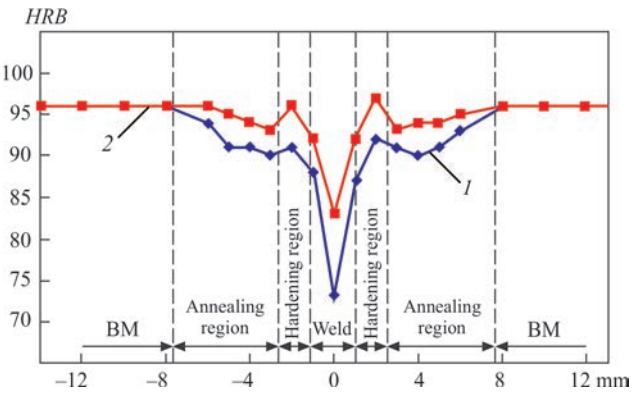

Figure 3. Hardness distribution in the cross-section of joints of quenched and artificially-aged 2219 alloy plates 40 mm thick; *1* — welded joints; *2* — welded joints reaged artificially after welding

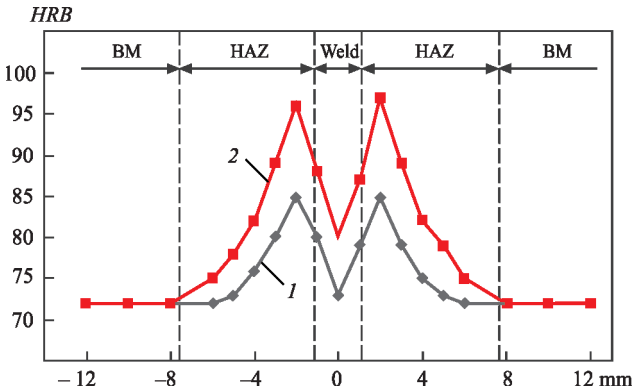

Figure 4. Hardness distribution in the cross-section of joints of annealed 2219 alloy plates 40 mm thick; *1* — welded joints; *2* — welded joints artificially aged after welding

axis (or 1.0, 3.0 and 5.0 mm from the fusion line) were equal to 590, 440 and 300 °C, respectively.

Weld metal microstructure (Figure 6, *a*) is dispersed; it consists of a matrix — aluminium-based α-solid solution and $CuAl_2$ (θ-phase), precipitating along the boundaries and chaotically in the grain bulk. $CuAl_2$ (θ-phase) is the main strengthening phase in alloys of this system. The fusion line (Figure 6, *b*) is well-formed, and no defects were found on the fusion line. HAZ width is up to 10 mm from the fusion line. Low-melting eutectic interlayers form in the HAZ region adjacent to the fusion line. A region of high-temperature recovery of the quenched state is located at 0.5–3.0 mm distance from the fusion line (Figure 3). It is characterized by a hardness increase after aging to base metal hardness level. The annealing region is next. A lowering of metal hardness by 2–3 *HRB* is observed in this region.

The influence of the sequence of welding and heat treatment operations on the mechanical properties of 2219 alloy welded joints was studied. Quenched plates and plates after full heat treatment (quenching and artificial aging) were welded. Quenched plates and part of the plates after full heat treatment were subjected to postweld artificial aging.

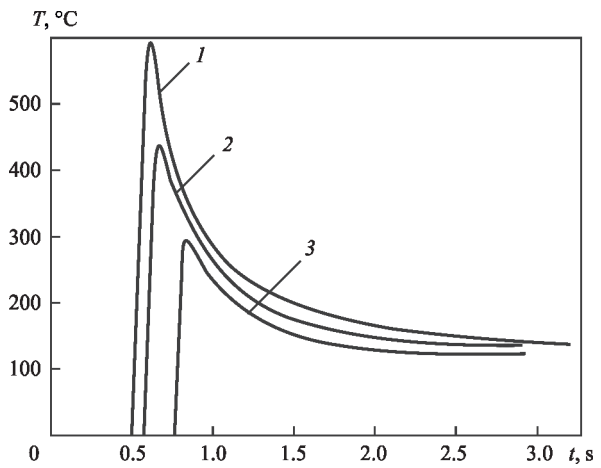

Figure 5. Thermal cycles of points on the surface of 2219 alloy plate at EBW with 20 mm/s speed (*L* — distance from weld middle; *1* — 2 mm; *2* — 4; *3* — 6)

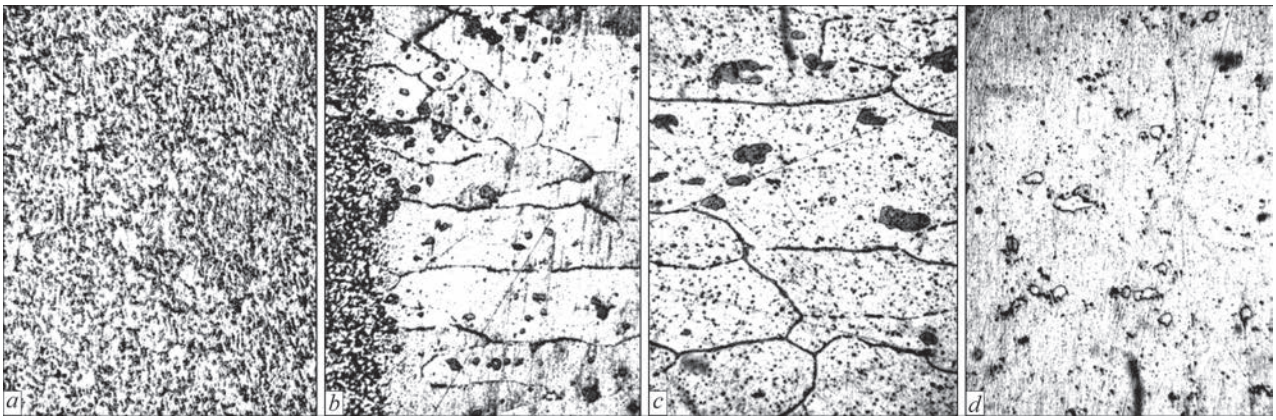

Figure 6. Microstructure of weld (*a*) and HAZ (*b–d*) metal at EBW of 2219 alloy plates (*a* — weld metal; *b* — fusion line; *c* — high-temperature recovery region; *d* — annealing region), (×500, reduced 2 times)

Table 3. Mechanical properties of joints of 2219 alloy plates 40 mm thick in different initial states of base metal and at further heat treatment

Kind of treatment		Ultimate strength, σ_{ult}, MPa	Relative elongation, δ, %	Impact toughness, *KCV*, kgf·m/cm^2
Before welding	After welding			
Quenching and artificial aging	Without heat treatment	300.0–315.0 308.7	3.0–4.0 3.3	4.2–4.7 4.5
Quenching and artificial aging	Artificial aging	357.0–367.5 361.7	2.6–5.7 3.6	1.4–1.7 1.5
Quenching	Artificial aging	385.0–395.0 388.7	3.0–3.0 3.0	2.9–3.2 3.0

Note. The numerator gives the minimal and maximal values from 3 measurements; the denominator gives the average values.

Results of welded joint testing for static tension and impact bending are shown in Table 3.

Electron beam welding is characterized by high rates of heating and cooling of the metal of the weld and HAZ. Such cooling rates in EBW of 2219 alloy will promote formation of copper solid solution in the weld metal. At further artificial aging precipitation of strengthening phases and increase of weld metal hardness occur, respectively.

Hardness increase at 1 mm distance from the fusion line is due to short-time heating of the metal to quenching temperature and rapid cooling. Maximal temperature of metal heating is about 590 °C. This zone is usually called the zone of high-temperature recovery of the quenched state. After conducting artificial aging, metal hardness is increased here up to the level of base metal hardness in the state after quenching and artificial aging. This zone was earlier revealed only in arc-welded joints [7, 8].

Annealing zone, called the low-temperature recovery zone, is located farther from the fusion line. At the beginning of this zone the maximal temperature was 440 °C, and in the middle part it was approximately 300 °C. Hardness of the metal of the weld and high-temperature recovery zone at EBW of heat-treated and annealed plates is the same and independent of the metal initial condition. As one can see from Figures 3 and 4, in welding heat-hardened plates of 2219 alloy the HAZ metal is softened, and in welding of annealed plates, on the contrary, the metal strength in the HAZ becomes higher.

In case of welding plates which have passed the full heat treatment cycle, the ultimate strength of the joints was equal to 300.0–315.0 MPa. It was possible to increase the ultimate strength to the level of 357.0–367.5 MPa, having conducted artificial aging. Here, the impact toughness decreased from 4.2–4.7 to 1.4–1.7 kgf·m/cm^2. Postweld artificial aging operation is more favourable, compared to aging before welding. In this case, the ultimate strength of the joints rises to 385–395 MPa, and impact toughness decreases only slightly to the level of 2.9–3.2 kgf·m/cm^2. Relative elongation changes only slightly here.

CONCLUSIONS

1. At EBW of quenched plates from 2219 alloy the maximal mechanical properties of welded joints are achieved by conducting postweld artificial aging.

2. Artificial aging of welded joints of 2219 alloy plates increases the hardness of weld and HAZ metal by 5–10 *HRB*.

3. When measuring HAZ hardness of 2219 alloy joints produced by EBW, a region of high-temperature

recovery of the quenched state with hardness increase was found at approximately 1 mm distance from the fusion line. After artificial aging the hardness of this region is increased to the level of base metal hardness in the heat-hardened state.

REFERENCES

1. Zhang, D.K., Wang, G.Q., Wu, A.P. et al. (2019) Study on the inconsistency in mechanical properties of 2219 aluminium alloy TIG-welded joints. *J. of Alloys and Compounds,* 777(**10**), 1044-1053. https://www.sciencedirect.com/science/article/abs/pii/S0925838818338568
2. *Tianyi* Zhao, Yue Zhao, Zhandong Wan et al. (2023) "Anneal" softening effect of 2219-T8 aluminum alloy joint during welding and its influence on prediction of welding residual stresses. *J. Mater. Research Technology*, **24**, 5202–5214. https://www.sciencedirect.com/science/article/pii/S2238785423007871
3. Zhang, D.K., Wang, G.Q., Wu, A.P. et al. (2019) Effects of post-weld heat treatment on microstructure, mechanical properties and the role of weld reinforcement in 2219 aluminum alloy TIG-welded joints. https://www.amse.org.cn/article/2019/1006-7191/1006-7191-32-6-684.shtml
4. Chen, Y. C., Liu, H. J., Feng, J. C. (2005) Effect of post-weld heat treatment on the mechanical properties of 2219-O friction stir welded joints. *J. Mater. Sci.,* 41(**1**), 297–299. https://www.researchgate.net/publication/227050248
5. Malarvizhi, S., Raghukandan, K., Viswanathan, N. (2008) Effect of post weld aging treatment on tensile properties of electron beam welded AA2219 aluminum alloy. *Int. J. Adv. Manuf. Technol.,* **37**, 294–301. https://link.springer.com/article/10.1007/s00170-007-0970-7
6. Rabkin, D.M., Lozovskaya, A.V., Sklabinskaya, I.E. (1992) *Metals science of aluminium and its alloys.* Kyiv, Naukova Dumka [in Russian].
7. Lozovskaya, A. V., Chaika, A. A., Bondarev, A. A. et al. (2001) Softening of high-strength aluminium alloys in different methods of fusion welding processes. *The Paton Welding J.*, **3**, 13–17. https://patonpublishinghouse.com/as/pdf/2001/as200103all.pdf
8. Lan-Qiang Niu, Xiao-Yan Li, Liang Zhang, Xiao-Bo Liang, Mian Li (2017) Correlation between microstructure and mechanical properties of 2219-T8 aluminum alloy Joints by VP-TIG welding. *J. Acta Metallurgica Sinica*, 30(**5**), 438–446. DOI: https://doi.org/10.1007/s40195-016-0516-9

ORCID

V.V. Skryabinsky: 0000-0003-4470-3421,
V.M. Nesterenkov: 0000-0002-7973-1986,
M.O. Rusynyk: 0000-0002-7591-7169

CONFLICT OF INTEREST

The Authors declare no conflict of interest

CORRESPONDING AUTHOR

V.V. Skryabinsky
E.O. Paton Electric Welding Institute of the NASU
11 Kazymyr Malevych Str., 03150, Kyiv, Ukraine.
E-mail: skriabinski.vv.555@gmail.com

SUGGESTED CITATION

V.V. Skryabinsky, V.M. Nesterenkov, M.O. Rusynyk (2024) Impact of heat treatment on mechanical properties of joints during electron beam welding of 2219 alloy. *The Paton Welding J.*, **1**, 22–26.

JOURNAL HOME PAGE

https://patonpublishinghouse.com/eng/journals/tpwj

Received: 12.10.2023
Received in revised form: 15.12.2023
Accepted: 17.01.2024

DOI: https://doi.org/10.37434/tpwj2024.01.04

WELDING CURRENT FORMERS USING ARTIFICIAL LONG LINES

O.Ye. Korotynskyi, M.P. Drachenko, A.M. Zhernosekov, I.V. Vertetska

E.O. Paton Electric Welding Institute of the NASU
11 Kazymyr Malevych Str., 03150, Kyiv, Ukraine

ABSTRACT

Application of artificial long lines in arc welding equipment is considered. These lines allow forming pulsed welding currents of a regulated shape. The need for such currents is determined primarily by the objectives of pulsed technologies, where the load current shape ensures the required time law of power input into the technological object. The most characteristic examples of such technologies are pulsed laser welding, laser heat hardening, laser piercing of holes, etc. The possibility of adjustment of amplitude-time parameters of load current pulses in a broad range allows determination and further on ensuring the optimal parameters of pulsed electrophysical processes in order to improve their quality and productivity. Special pulsed current generators are required to create such energy flows, which are described and proposed in the paper.

KEYWORDS: welding current formers, artificial long line, step-down multiphase converter, pilot-arc power source

INTRODUCTION

Artificial long lines (ALL) are currently used to construct pulsed formers of arc welding currents. The need for such currents is determined primarily by the objectives of welding technologies, where the load current pulse shape ensures the required time law of power input into the technological object. The most characteristic examples of such technologies are pulsed laser welding, laser heat hardening, laser piercing of holes, capacitor discharge resistance welding, etc. Possibility of adjustment of amplitude-time parameters of load current pulses in a broad range allows determination and furtheron ensuring optimal parameters of pulsed electrophysical units, in order to improve their quality and productivity. Generation of such currents requires special pulsed current generators (PCG) [1–3].

Proceeding from the abovesaid, the proposed work is devoted to creation and development of versatile pulsed current generators designed to construct welding current formers with high characteristics of energy efficiency and electromagnetic compatibility (EMC) [4].

The objective of this work is substantiation and creation of structures of powerful generators of regulated pulsed currents (GRPC) and their experimental investigation. Electrotechnological generators of regulated pulsed current are required first of all as a tool, which allows experimental investigation of the main parameters of pulsed technological process, including current shape, in order to improve both the process quality and its efficiency. In addition, pulsed technological units with amplitude-time pulse parameters regulated in a broad range are of great interest when working under the conditions of small-scale production with frequent changes of product range and kinds of structural materials. Recently, high-frequency converters operating in the pulse-width regulation mode have been used with success for generation of current pulses of a regulated shape in the pulse duration range from several milliseconds to seconds, at load current levels of several hundred amperes. Such converters use modern power transistors, capable of switching hundreds of amperes of current at frequencies of up to hundreds of kilohertz.

When developing generators of rectangular current pulses of a regulated duration, partial discharge of capacitive storage is most often used, when a fully-controlled power key connects the load to the storage for the time which is equal to pulse duration. A serious drawback of such generators is the energy stored in the device significantly exceeding the energy evolving in the load during the pulse time, as power key malfunction can result in grace accidents, which can lead to load failure. The above disadvantage is overcome, when a fundamentally new type — a homogeneous artificial long line (HALL) is used as storage and forming two-terminal network (FTTN). Here, not only the energy accumulated in the storage is lowered, but also its weight and dimensional characteristics are reduced.

The proposed approach consists in a combined use of ALL-based generators and storages using supercapacitors (SC) having high energy efficiency and electromagnetic compatibility characteristics. It allows creating promising devices for pulsed-arc welding.

METHODS OF INVESTIGATION

The following solutions are mainly used when creating pulsed current generators:

- method of partial discharge of capacitive storage [5, 6];
- ALL application as current formers [7, 8];
- multiphase step-down voltage converters (choppers) with microprocessor control [9, 10].

Figure 1 shows two variants of ALL application for welding equipment. The first variant (*a*) is a series con-

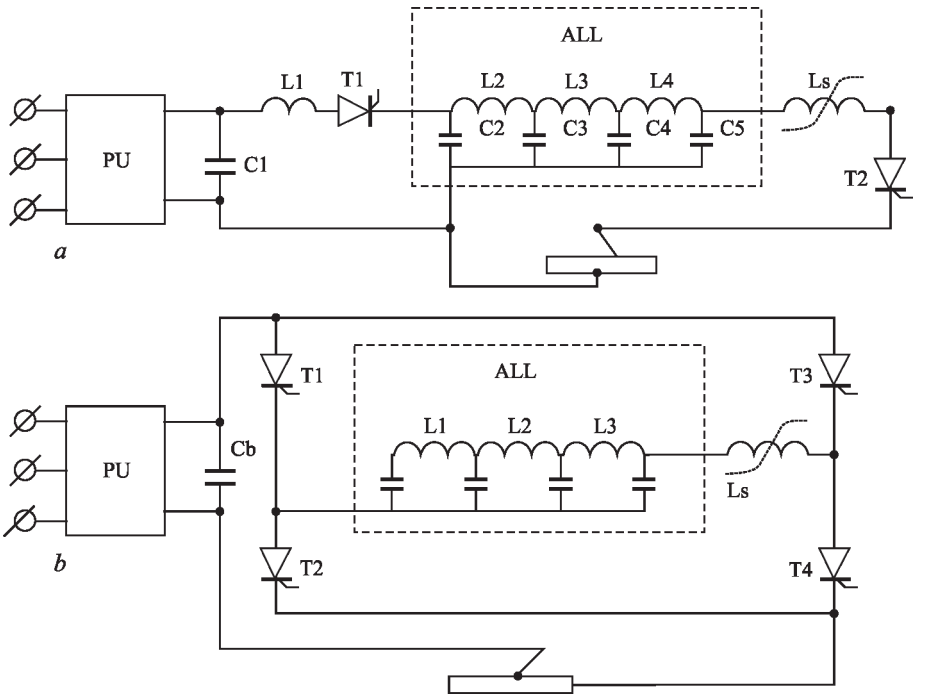

Figure 1. Variants of ALL application (for *a*, *b* description see the text)

nection of three-phase rectifier, charge switch, ALL and switch of its discharge on the load. The second variant (*b*) includes charging rectifier, capacitive storage and bridge inverter, with ALL connected into its diagonal.

Let us analyze ALL operation as part of pulsed welding current sources.

Based on the considered welding systems, a variant of the circuit of inverter-type pulsed current former was proposed. It incorporates ALL shown in Figure 2. A chain of three LC elements is used as current pulse former. The main calculations are used according to works [11, 12]:

$$I_p = (U + U_c - U_a)/2\rho;\ \rho = (L_c/C_c)^{1/2},$$

where I_p is the current pulse amplitude; U is the power source voltage; U is the charge voltage of the forming line; U_a is the voltage across the arc gap; ρ is the wave impedance.

Pulse duration is defined by the following expression:

$$t = 2.2n(L_cC_c)^{1/2},$$

where n is the number of forming line cells; L_c is the inductance of the forming line cell choke; C_c is the capacity of the forming line cell capacitor.

Thus, the duration of the pulse front is determined by the following relationship:

$$t_f \approx 0.61 - (L_c - C_c)^{1/2} = 0.27t/n,$$

and pulse cutoff duration is given by the following expression:

$$t_{end} \approx (0.075n + 2.3)\ (L_cC_c)^{1/2}.$$

An operating mockup of pulsed welding current source was developed and tested according to the diagram in Figure 2 (Figure 3).

Current pulses were generated using the known "skew bridge" circuit, with ALL connected into its diagonal in series with pulse transformer Tr2. Short-circuited ALL output is connected to Tr1 transformer, which is used in the circuit of the former of arc standby current. Here, the standby current is formed in the pauses between working current pulses.

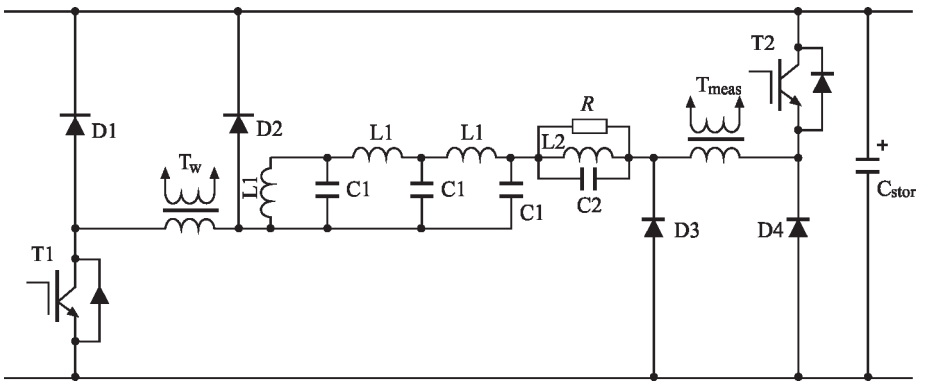

Figure 2. Explanatory diagram of ALL element calculation

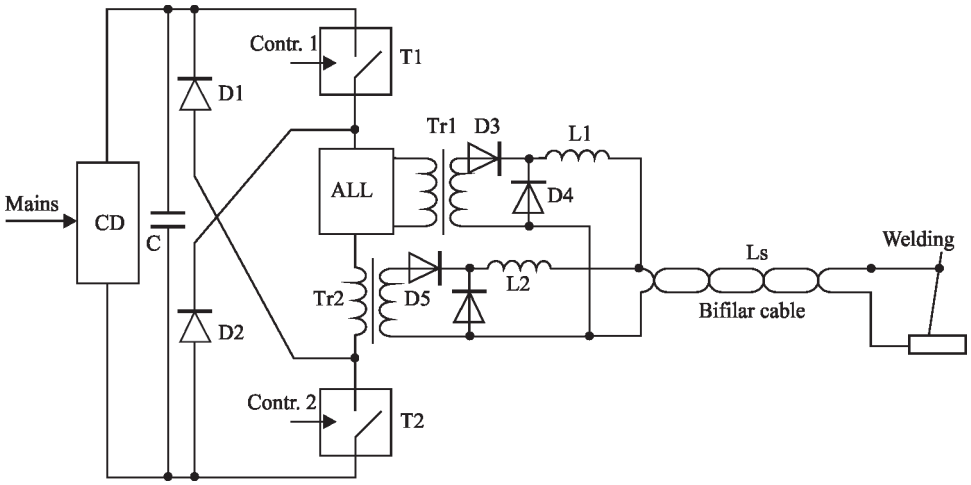

Figure 3. Block diagram of a mock-up of a welding current source based on ALL

As part of the work, a current sensor module was developed on the basis of a bifilar shunt circuit with a high level of in-phase interference suppression.

EXPERIMENTAL STUDIES OF DEVELOPED MOCKUP

The proposed device, the diagram of which is shown in Figure 3, provides a stable arc burning in the dynamic mode, which, in its turn, allows improving the quality of the welded joint and the energy characteristics of the device operation. This source was tested in the mode of welding with pulse modulation of current at the frequencies from 50 to 3500 Hz. Pulse amplitudes were varied from 50 to 100 A. The lower limit of stable welding currents was observed at currents higher than 20 A.

Figure 3 shows the oscillograms of operation of a forward converter incorporating an ALL.

APPLICATION OF STEP-DOWN CONVERTERS AS PULSED WELDING CURRENT FORMERS

Variants of ALL application in step-down voltage converters (SDVC), which can be used in multistation welding complexes, were also studied as part of the performed work. An example of ALL application in step-down

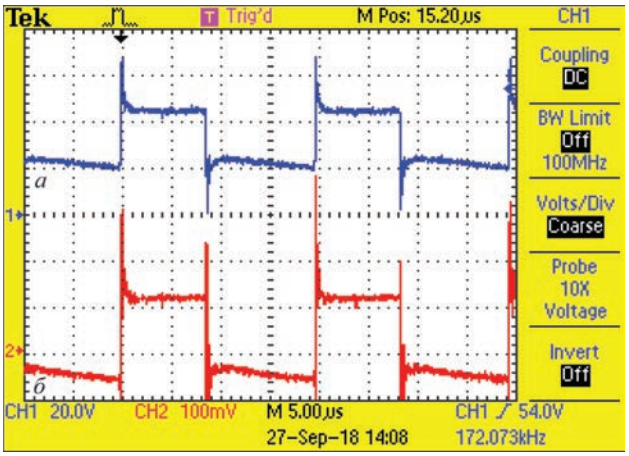

Figure 4. Oscillograms of voltage "*a*" and current "*b*" at the welding device output

voltage converters is shown in Figure 5. Adjustment of the duration and repetition frequency of current pulses is performed by electronic switch on transistor key T2.

The long line is charged from capacitive storage Csc, which is connected to charging device (CD). Monitoring and adjustment of CD charge parameters are performed in keeping with feedback signals, received from current CScd and voltage VScd sensors.

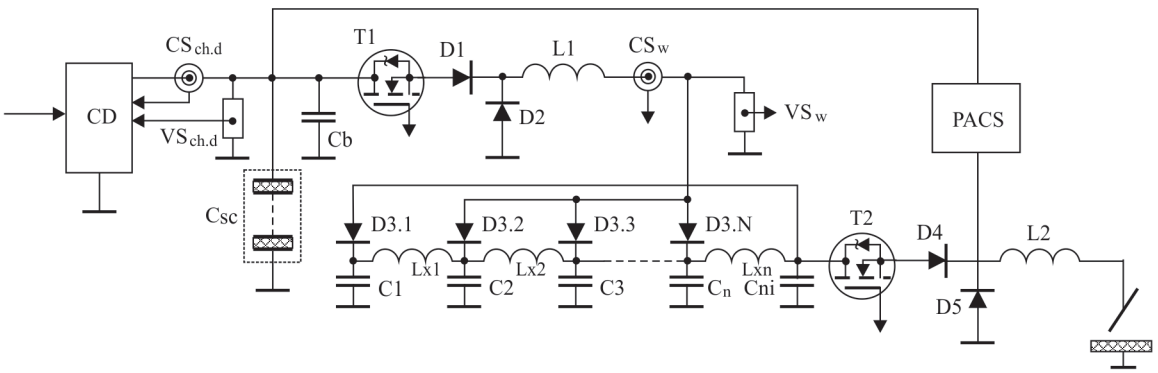

Figure 5. Step-down voltage converter — pulsed current former: CD — charging device of super capacitor battery C_{sc}, $CS_{ch.d}$ and $VS_{ch.d}$ — current and voltage sensors; SCB — super capacitor battery; TI and T2 — solid state transistor switches; D1, D2 — normalizing diodes; D2, D5 — recovery diodes; Cb — battery capacitance; CSlc and VSlc — sensors of ALL charge current and voltage; D3.1–D3.N, Lx1–Lxn, C1–Cn — ALL elements

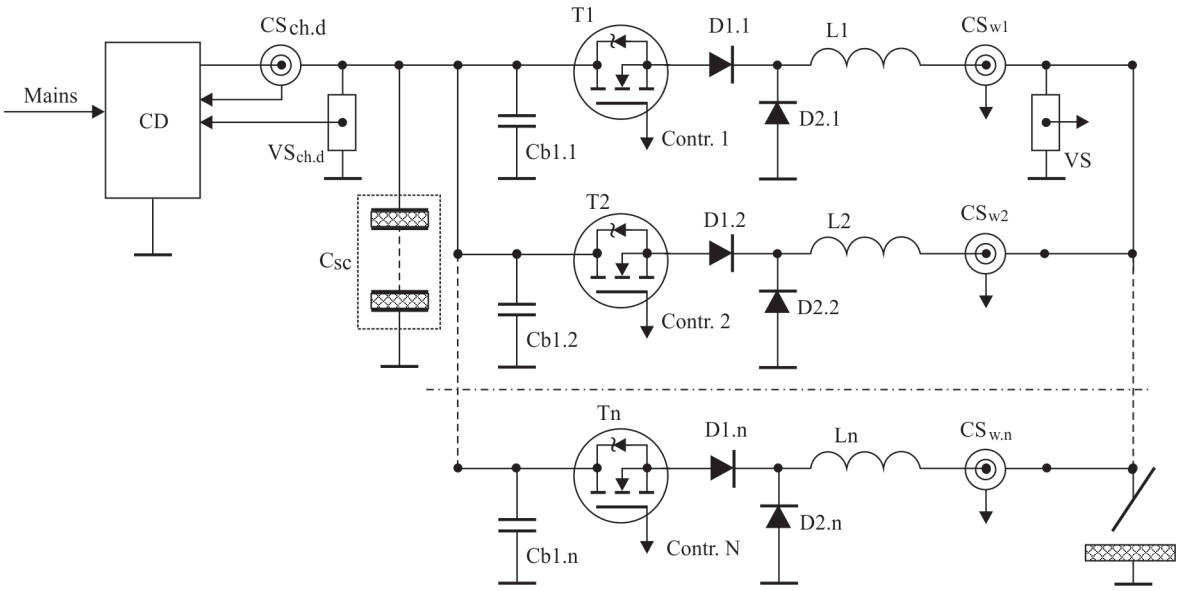

Figure 6. Multiphase SDVC — source of welding current pulses: CD — charging device; $CS_{ch.d}$ and VS_{ch} — sensors of current and voltage of charging device control; SCB — capacitive storage based on super capacitor battery; Cb1.1–Cb1.n — buffer capacitors; T1–Tn — solid state transistor current switches; D1.1– D1.n — normalizing diodes; D2.1 – D2.n — recovery diodes; T1–Tn, D1.X– D1.n, D2.x–D2.n, L1–Ln — elements of step-down converters — welding current pulse formers; $CS_{w.1}$–$CS_{w.n}$, VS_w — sensors of control current and voltage of control system of welding current pulse former

Step-down converter, consisting of TI, D1, D2, L1, performs ALL charging in the constant power mode.

Power monitoring and control are conducted by signals, which are formed by current CScd and voltage VScd sensors.

Pilot arc current source (PACS) operates continuously, and its current is summed up on the load (welding arc) with the main welding current pulses.

A variant with formation of welding current pulses without ALL application, but using a multiphase step-down voltage converter was also considered (Figure 6). Here regulation of the duration, frequency and shape of welding current pulses is performed by synchronous control of transistor switches T1–Tn.

The converter is powered from capacitive storage Csc, which is charged from charging device CD. Monitoring and regulation of SC charge parameters is performed by feedback signals, coming from current CScd and voltage DVcd sensors. In this circuit the mode of operation with interrupted currents in chokes L1–Ln is used to improve the dynamic parameters of current pulses. One of the converter channels is used to generate the arc standby current, and it operates in the mode of continuous current of choke Lo.

Comparative analysis of operation of these devices shows that preference should be given to multiphase converter circuit, as it allows regulation of the time parameters of the amplitude and shape of welding current pulse in a broad range.

CONCLUSIONS

1. Features of operation and application of welding current formers based on artificial long lines to create resource- and energy-efficient power sources for arc welding were considered.

2. Good prospects for their application are shown when powering capacitive energy storages in the mode of dynamic burning of the arc.

3. New circuits of combined power sources based on artificial long lines were proposed, and their experimental study in the range of welding current frequencies of 50–3500 Hz was conducted. Features of artificial long line functioning as part of step-down converters are considered.

4. As shown by experimental studies, these devices are characterized by high values of energy efficiency and electromagnetic compatibility.

REFERENCES

1. Anisimova, T.E., Akkuratov, E.V., Gromovenko, V.M. et al. (1987) High-voltage pulse generator with alternating duration. *Pribory i Tekhnika,* **4**, 45–48 [in Russian].
2. Opre, V. (2008) Generators of current rectangular pulses. *Silovaya Elektronika,* **1**, 56–61 [in Russian].
3. Kazmierkowski, M.P., Krishnan, R., Blaabjerg, F. (2002) *Control power electronics*. USA, Academic Press.
4. Tihanyi, L. (1995) *EMC in Power Electronics.* N.Y., IEEE Press.
5. Allas, A.A., Korotkov, A.Yu., Opre, V.M., Fedorov, A.V. (2001) *Charging device.* RF Pat. 18026. Publ. 10.05.2001 [in Russian].
6. Leonard, W. (1996) *Control of Electrical Drives*. Berlin, Springer.
7. Korotynskyi, O.E., Skopyuk, M.I., Vertetska, I.V. (2021) High-efficient sources for arc welding on the base of capacitive energy storage systems. *The Paton Welding J.,* **3**, 43–48 DOI: https://doi.org/10.37434/tpwj2021.03.08 H
8. Gromovenko, V.M., Opre, V.M., Shchegoleva, N.A. (1997) Charging devices of split capacitive storages. *Elektrotekhnika,* **3**, 46–48 [in Russian].
9. Korotynsky, A.E. (1999) Peculiarities of operation of high-frequency welding inverters on the basis of an artificial long line. *Avtomatich. Svarka*, **1**, 76–77 [in Russian].

10. Mohan, N., Undeland, T.M., Robins, W.P. (1995) *Power electronics: Converters, application and design*. USA, NYJohn Willey&Sons Inc.
11. Chebotaryov, V.I. (2008) *Wave processes in long lines:* Monographies. Kharkov, Izd-vo im. V.N. Karazin [in Russian].
12. Povh, D., Weinhold, M. (2000) *Improvement of power quality by power electronic equipment*. CIRGE. Paper 13/14/36-06. Paris.

ORCID
O.Ye. Korotynskyi: 0000-0002-6461-8980,
M.P. Drachenko: 0000-0002-4485-2403,
A.M. Zhernosekov: 0000-0002-6404-2221,
I.V. Vertetska: 0000-0003-4971-7929

CONFLICT OF INTEREST
The Authors declare no conflict of interest

CORRESPONDING AUTHOR
O.Ye. Korotynskyi
E.O. Paton Electric Welding Institute of the NASU
11 Kazymyr Malevych Str., 03150, Kyiv, Ukraine.
E-mail: epis@ukr.net

SUGGESTED CITATION
O.Ye. Korotynskyi, M.P. Drachenko, A.M. Zhernosekov, I.V. Vertetska (2024) Welding current formers using artificial long lines. *The Paton Welding J.*, **1**, 27–31.

JOURNAL HOME PAGE
https://patonpublishinghouse.com/eng/journals/tpwj

Received: 09.10.2023
Received in revised form: 23.12.2023
Accepted: 15.01.2024

DOI: https://doi.org/10.37434/tpwj2024.01.05

NICKEL SCRAP RECYCLING BY ELECTRON BEAM MELTING METHOD

S.V. Akhonin[1], V.O. Beresos[1], O.G. Erokhin[2], O.O. Kotenko[2], M.I. Medvedev[3], M.G. Lyashenko[4]

[1]E.O. Paton Electric Welding Institute of the NASU
11 Kazymyr Malevych Str., 03150, Kyiv, Ukraine
[2]SC "SPC "Titan" of the E.O. Paton Electric Welding Institute of the NASU"
26 Raketna Str., 03028, Kyiv, Ukraine
[3]Ukrainian State University of Science and Technologies
2 Lazaryan Str., 49010, Dnipro, Ukraine
[4]"DZST" Ltd.
1 Horyanivska Str., Horyanivske Vil., 52035, Dnipropetrovsk Region, Ukraine

ABSTRACT

Experimental-production melting of low-grade nickel scrap was conducted to obtain nickel ingots of not lower than NP2 grade, which are furtheron used to produce semi-finished products in the form of hot- and cold-formed seamless pipes, including capillary, thin-walled and particularly thick-walled pipes, rings, squares, hexagons, etc. It is shown that during electron beam melting a significant removal of impurity elements from the nickel scrap occurred, and metal quality began to correspond to nickel grade not lower than NP2. In order to further study the produced ingot quality, comprehensive research work was performed on manufacturing semi-finished products in the form of elongated soft rods of 40 mm diameter and wire of 3 mm diameter. It was determined that mechanical properties of semi-finished products from EBM nickel fully meet the standard requirements. It is shown that electron beam melting is an efficient method of producing nickel ingots from secondary raw materials, as it allows ensuring a high level of the produced material quality, and the semi-finished product quality fully meets the standard requirements by chemical composition, structure and mechanical properties.

KEYWORDS: electron beam melting, electron beam unit, nickel, melting, ingot, scrap, refining

INTRODUCTION

Nickel belongs to the group of heavy nonferrous metals used both in alloyed steel production and in manufacturing high-tech products in the sphere of aircraft construction, medicine and electronics [1]. Wide application of nickel in different industries is due to its unique properties. Nickel addition to alloys increases their strength, wear resistance, corrosion resistance, heat- and electric conductivity, and improves their magnetic and catalytic properties.

In Ukraine proven reserves of nickel ore deposits are small or depleted, new deposits are insufficiently explored, but the need in such kinds of raw materials is due to increased demand and industrial progress [2]. Thus, nickel production in Ukraine has limited development and it largely depends on price situation in the world market.

Today, the proportion of secondary raw materials during nonferrous metal manufacture is continuously growing. Analysis of tendencies in production and consumption of products from nickel and alloys on its base shows that all the Ukrainian enterprises, operating in this market segment, more and more often use metal scrap as the starting raw material. In the long term it should become the main source of producing many nonferrous metals, in particular, nickel, and its efficient recycling will cover the deficit of balance between consumption and own production. Involvement of secondary raw materials into the metallurgical production cycle is of tremendous economic importance, as it allows rational use of non-renewable natural resources, reducing the technogenic load on the environment, producing metal by simpler and less costly methods.

Therefore, under the conditions of unpredictable changes in the world markets of metallurgical products, the manufacturers of structural elements from nickel and alloys on its base are faced with an acute issue of improvement of production efficiency and ensuring output of high-quality competitive products. Further increase of competitiveness of local products from nickel and alloys on its base due to an essential lowering of the material and energy costs for its production is a complex task. The urgency of solving it for Ukraine is determined both by the need of recycling low-grade local metal scrap from nickel, and by the wish to manufacture final products meeting the world standards, as today strict requirements are put forward in the world markets for the quality of products made from recycled raw materials. Therefore, one of the main stages of ensuring the final product quality is producing a high-quality ingot as the initial billet for further processing. Here, in order to ensure the required level of ingot quality, it is necessary to study in greater detail the influence of both the secondary raw material properties and of the technological parameters of conducting the process. Both the

yield and the quality of the produced metal depend in many respects on a rational organization of this process. Increase of the quality and lowering of the ingot cost can be achieved due to a detailed study of the processes of crystallization and formation of casting defects. The processes of secondary nickel refining at electron beam melting (EBM), which are still insufficiently studied, have an important role here. This is particularly relevant in production of nickel ingots from low-quality scrap, where impurity content can reach high values.

Therefore, a promising route for development of enterprises using nickel in their manufacturing is creation and introduction of high-efficient technologies of producing cleaned nickel, based on secondary raw materials.

A promising direction of modern metallurgy is application of electron beam heat sources for melting, refining, surface treatment and other technological processes [3].

Investigations of the processes of nickel refining to remove impurities by electron beam melting were considered in works [4–7].

EBM is used to produce high-purity ingots of refractory and highly reactive metals and alloys. As to their quality, EBM ingots are superior to the initial material. At EBM of nickel effective removal of gases and other impurities takes place. High vacuum, drop transfer and overheating of the metal pool surface in electron beam melting create favourable conditions for practically complete removal of such impurities as As, Zn, Se, Cl, Fe, P, Mg, etc. [4].

Ingots of EBM nickel have high ductility and are easily deformed at room temperatures [7].

With the purpose of vacuum refining, EBM is performed in a copper water-cooled mould with a cold hearth by horizontal feeding of the material being remelted. Here, charge materials can have the form of ingots, lump charge, rods and various wastes, for instance pressed chips [3].

INVESTIGATION PROCEDURE

Experimental-production melts of low-grade nickel wastes were conducted in production facilities of SC "SPC "Titan" of the E.O. Paton Electric Welding Institute of the NAS of Ukraine" together with "DZST" Ltd. Company, in order to produce nickel ingots of not lower than NP2 grade (not lower than 99.5 wt.% nickel content). These ingots are further on used to produce semi-finished products in the form of hot- and cold-rolled seamless pipes (capillary, thin-walled and particularly thick-walled), rings, squares, hexagons, etc.

Used as the initial charge was low-grade scrap with average nickel content of 98 wt.% (Figure 1), which was subjected to double EBR in electron beam unit UE-208M [8].

The technology of producing ingots in electron beam unit included the following: forming the consumable billet; preparation of the equipment and technological fixtures for melting; melting process and control of the produced ingot quality.

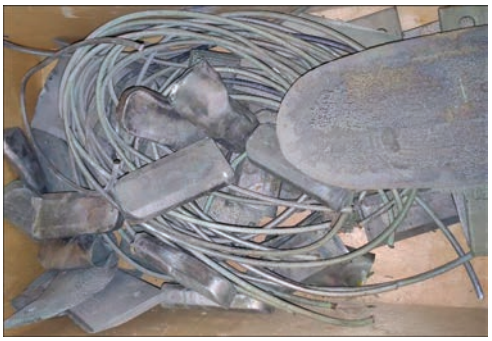

Figure 1. Low-grade nickel wastes

Low-grade nickel scrap was cleaned from surface contamination of different origin, compactly packed into a nonconsumable box and loaded into electron beam unit UE-208M (Figure 2).

The technology of cold-hearth EBM with portioned liquid metal feeding into a water-cooled mould (Figure 3) was used to produce ingots of 150 mm diameter (Figure 4).

The following technological parameters were monitored during melting: accelerating voltage of electron beam guns, beam currents, rate of initial charge feeding into the melting zone, speed of the ingot pulling from the mould, and cooling water temperature.

Numerical values of the technological parameters of melting, used at remelting the nickel scrap, are as follows:

Melting speed, kg/h	50
Height of portions which are poured into the mould at a time, mm	10
Power, kW	
in the mould	25
in the cold hearth	100

Figure 2. Initial charge from low-grade nickel scrap

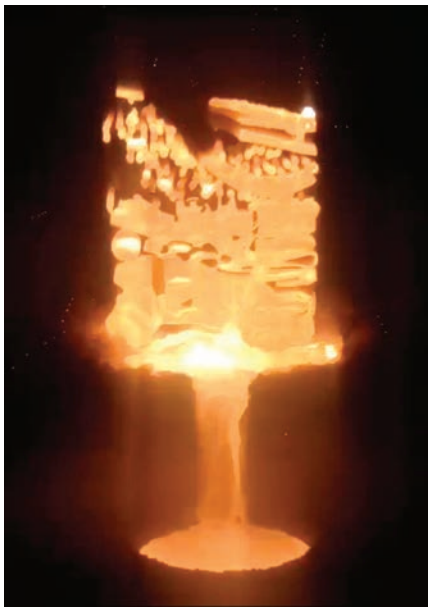

Figure 3. Process of electron beam remelting of nickel

At the end of melting, the shrinkage cavity was removed by gradual lowering of the power of heating the ingot upper end face in the mould.

The side surface of the produced ingots after cooling in vacuum to a temperature below 200 °C is clean, and a higher concentration of impurity elements on the surface in the form of an oxidized or alpha layer is absent (Figure 4). The depth of corrugation-type surface defects is 1–3 mm, defects in the form of tears, cracks or discontinuities are absent.

Metal of the produced ingots was studied to assess the depth of refining of low-quality nickel scrap during EBM. Determination of chemical composition of samples taken by their length from the upper, middle and lower parts was conducted by the method of inductively couple plasma optical emission spectrometry (ICP-OES) in ICP-stpectrometer ICAP 6500 DUO. Results of analysis of the produced ingot metal showed that significant removal of impurity elements from nickel scrap occurred during EBM (Table 1),

Figure 4. EBR nickel ingot of 150 mm diameter

and the metal quality began corresponding to nickel grade not lower than NP2.

Comprehensive research work on manufacturing semi-finished products was conducted at DZST Ltd. for further study of the produced ingot quality. EBM nickel ingots of 150 mm diameter were used to produce soft rods of 40 mm diameter and 3 mm diameter wire (Figure 5).

Produced rods were subjected to heat treatment (HT) by the following mode: heating up to 800 °C temperature in vacuum; soaking for 0.5 h; cooling with the furnace. After HT the rods were machined to the required dimensions. Samples for macrostructural studies were taken from the produced rods. No cracks, delamination, voids, metallic or nonmetallic inclusions were detected in the macrostructure of the produced rods. The macrograin dimensions correspond to 3–4 grain size number to GOST 26492–85.

Mechanical properties of rod metal were determined at the temperature of 20 °C after the conducted heat treatment. Table 2 gives the mechanical properties of drawn soft rods of 40 mm diameter. As one can see from the Table, the mechanical property values of the produced samples fully meet the requirements of GOST 13083–77 [9], which is indicative of the high quality of the metal produced by the developed technology. These data lead to the conclusion that the mechanical properties of semi-finished products from EBM nickel fully meet the standard requirements.

Table 1. Element content in EBR nickel ingot of 150 mm diameter, wt.%

Not more than									
Metal	As	Bi	C	Cd	Cu	Fe	Mg	Mn	P
After double EBR	0.0001	0.0001	0.015	0.0001	0.01	0.04	0.0012	0.0023	0.0001
Norm by DSTU GOST 492:2007	0.002	0.002	0.1	0.002	0.1	0.1	0.1	0.05	0.002

Table 1 (Cont.)

Not more than								Not less than
Metal	Pb	S	Sb	Si	Sn	Zn	Co	Ni+Co
After double EBR	0.0001	0.0043	0.0003	0.006	0.0016	0.0001	0.021	99.90
Norm by DSTU GOST 492:2007	0.002	0.005	0.002	0.15	0.002	0.007	0.2	99.5

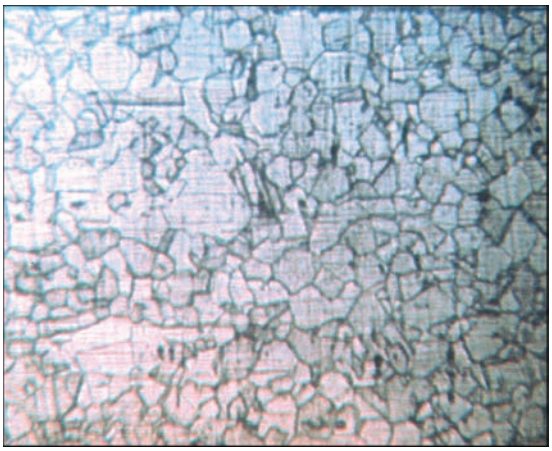

Figure 6. Macrostructure of 40 mm dia rod from EBM nickel of NP2 grade

Table 2. Mechanical characteristics of drawn soft rods of 40 mm diameter

Grade	σ_t, MPa	δ_{10}, %	δ_5, %
EBM nickel NP2	375–390	28–32	37–40
GOST 13083–77	>370	>26	>30

CONCLUSIONS

Thus, by the results of the conducted work, it was shown that electron beam melting is an effective method to produce nickel ingots from secondary raw materials, as it provides a high level of the produced material quality, and the semi-finished product quality fully meets the standard requirements by its chemical composition, structure and mechanical properties.

REFERENCES

1. Grytsai, V.P., Bredykhin, V.M., Chervonyi, I.F. et al. (2010) *Metallurgy of nonferrous metals:* Manual. Pt 5. Book 2, Technology of copper and nickel. Ed. by I.F. Chervonyi. Zaporizhzhiya, ZDIA [in Ukrainian].
2. Pozhuev, V.I., Ivashchenko, V.I., Chervonyi, I.F., Grytsai, V.P. (2007) *Metallurgy of nonferrous metals:* Manual. Pt 1. Ed. by I.F. Chervonyi. Zaporizhzhiya, ZDIA [in Ukrainian].
3. Paton, B.E., Trigub, N.P., Akhonin, S.V., Zhuk, G.V. (2006) *Electron beam melting of titanium.* Kyiv, Naukova Dumka [in Russian].
4. Dmitrenko, A.E., Kozhevnikov, O.E., Pelykh, V.N. (2003) Application of method of electron beam melting for refining of nickel. *Voprosy Atomnoj Nauki i Tekhniki,* **5**, 162–166 [in Russian].
5. Azhazha, V.M., Zejdlits, M.P., Shevchenko, S.V., Amonenko, V.M. (1973) Influence of chemically active elements on properties of nickel of electron beam melting. *Izv. AN SSSR. Metally,* **4**, 157–159 [in Russian].
6. Trigub, N.P., Berezos, V.A., Kornijchuk, V.D., Mosunov, Yu.A. (2011) Producing of high-quality nickel ingots-slabs by electron beam melting. *Advances in Electrometallurgy,* **2**, 78–81.

Figure 5. Semi-finished products from EBM nickel of NP2 grade: *a* — 3 mm wire; *b* — drawn soft rods of 40 mm diameter

7. Movchan, B.A., Tikhonovsky, A.L., Kurapov, Yu.A. (1973) *Electron beam melting and refining of metals and alloys.* Kyiv, Naukova Dumka [in Russian].
8. Akhonin, S.V., Pikulin, A.N., Berezos, V.A. et al. (2019) Laboratory electron beam unit UE-208M. *Sovrem. Elektrometal.,* **3**, 15–22 [in Russian].
9. *GOST 13083–77: Rods from nickel and silicon nickel. Specifications*.

ORCID

S.V. Akhonin: 0000-0002-7746-2946,
V.O. Berezos: 0000-0002-5026-7366,
O.G. Erokhin: 0000-0003-2105-5783,
O.O. Kotenko: 0000-0002-0930-9536,
M.I. Medvedev: 0000-0002-1230-420X

CONFLICT OF INTEREST

The Authors declare no conflict of interest

CORRESPONDING AUTHOR

S.V. Akhonin
E.O. Paton Electric Welding Institute of the NASU
11 Kazymyr Malevych Str., 03150, Kyiv, Ukraine.
E-mail: titan.paton@gmail.com

SUGGESTED CITATION

S.V. Akhonin, V.O. Berezos, O.G. Erokhin, O.O. Kotenko, M.I. Medvedev, M.G. Lyashenko (2024) Nickel scrap recycling by electron beam melting method. *The Paton Welding J.*, **1**, 32–35.

JOURNAL HOME PAGE

https://patonpublishinghouse.com/eng/journals/tpwj

Received: 31.10.2023
Received in revised form: 07.12.2023
Accepted: 16.01.2024

DOI: https://doi.org/10.37434/tpwj2024.01.06

EFFECT OF THE TEXTURE OF FERROMAGNETIC Co–Fe COATINGS ON THEIR DAMPING CAPACITY

O.S. Kremenchutskyi[1], **S.S. Polishchuk**[2]

[1]E.O. Paton Electric Welding Institute of the NASU
11 Kazymyr Malevych Str., 03150, Kyiv, Ukraine
[2]G.V. Kurdyumov Institute for Metal Physics of the NASU
36 Academician Vernadsky Blvd, 03142, Kyiv, Ukraine

ABSTRACT

The effect of the crystallographic texture of Co-Fe coatings produced by the method of electron beam physical vapour deposition (EB PVD) on their damping capacity (DC) has been studied. It is found that the amplitude dependence of DC of a coating with a fiber <111> texture exhibits a prominent maximum, while that of a coating with a multicomponent <100> + <111> + <110> fiber texture shows the blurred maximum which has shifted to the higher amplitude deformations. The effect of both the fiber texture type and the level of internal (residual) stresses in Co–Fe coatings on the amplitude dependence of the DC has been analyzed within the framework of the Smith-Birchak model. It is shown that transition from a single-component to a multicomponent coating texture reduces the maximum value of DC. In contrast, an increase in the internal stresses in the coatings leads to a shift and blurring of the DC maximum. On this basis, it is concluded that the maximum DC for Co–Fe coatings can be achieved provided that they have a fiber <111> texture and a minimum level of internal stresses.

KEYWORDS: EB PVD, coating, Co–Fe alloy, damping capacity, texture, internal stresses

INTRODUCTION

Suppression of resonance vibrations (RV) in products that are exposed to intense vibrations, for example, in blades of gas turbine engines is a prerequisite for preventing their premature failure [1]. The use of highly damping coatings for such products is considered as one of the means of reducing the amplitude of RV in them. The works [2–4] show the possibility of using ferromagnetic coatings that combine high damping capacity (DC) with acceptable mechanical and corrosion properties.

In ferromagnets with BCC lattice, dissipation of mechanical energy is mainly related with the irreversible shift of the boundaries of 90° magnetic domains in the action of dynamic stresses. In [5], a model displaying magnetomechanical attenuation (MMA) of oscillations is proposed, from which it follows that the maximum value of damping is proportional to the magnetostriction of material saturation and the variation of amplitude dependence of DC characteristics is determined by the level and dispersion of residual (internal) stresses, which interfere with the movement of magnetic domain boundaries.

The work [6] shows that the magnitude of magnetostriction in the massive textured material changes depending on the direction of action of external stresses on it. Therefore, it can be expected that DC of coatings of ferromagnetic materials will depend on the type of coatings texture and residual stresses in their volume.

It is known that the microstructure of vacuum condensates is largely affected by the temperature of their deposition, in particular, at deposition temperatures T_d, for which the temperature T_d/T_m = 0.3–0.5, where T_m is the melting point of condensing metal corresponding to the second structural zone [7], which is characterized by a columnar microstructure of the coating. In this case, the thickness of columnar crystallites decreases as the temperature of condensate deposition drops. The example of vacuum condensates of Cu [8] and Ni [9] shows that with a decrease in the thickness of crystallites, their crystallographic texture changes. Moreover, this is accompanied by the transformation of a single-domain structure of the coatings in a multidomain substructure, when columnar crystallites are fragmented as a result of twins' formation in them. Such changes of microstructure in the coatings of ferromagnetic materials can significantly affect the mobility of magnetic domain boundaries and, accordingly, their DC.

The mobility of magnetic domain boundaries is also determined by the dislocation density in the volume of a coating. The work [10] shows that an increase of dislocation density in the Co–20 wt.% Fe coating as a result of sequential plastic deformation by a shock ultrasonic wave leads to shifting the amplitude maximum of a logarithmic decrement of vibrations (LD) and reduction in its height.

Based on the abovementioned, on the example of coatings from Co–Fe alloy, from MMA oscillations obtained under different conditions of their deposition, the effect of texture on the amplitude dependence of DC characteristics of ferromagnetic alloys with BCC lattice was studied.

Ferromagnetic Co–Fe alloy as an object of study was chosen taking into account its high DC in a wide temperature range, which is important in terms of developing damping coatings based on materials of this class and their practical application [11].

EXPERIMENT PROCEDURE

Co–20 % Fe coating of 90–120 μm thickness was deposited by the method of EB PVD on 1.8 mm thick substrates, produced in the form of an elongated trapezoid from the sheet of Ti-6-4 alloy (Figure 1). The coating was produced in the stationary and non-stationary conditions at substrate temperatures of 350–500 °C. In the first case, the substrate was fixed over the evaporator, in the second case it rotated around its longitudinal axis at a speed of 80 rpm in the process of coating formation.

Characteristics of DC of coating material (amplitude dependences of LD) were investigated in the laboratory installation described in [12]. The initial values of LD of the substrate-coating system were measured in the mode of freely attenuated bending oscillations with a frequency of 130–150 Hz. The intrinsic of LD of the coating material were determined by the procedure described in [13], based on the initial data for the specimens with coatings and without them. Such approach allows eliminating nonuniform distribution of deformation on the surface of the specimen, i.e., it represents deformation of the coating material in the approximation of pure bending, and also makes it possible to eliminate the effect of coating thickness on its DC.

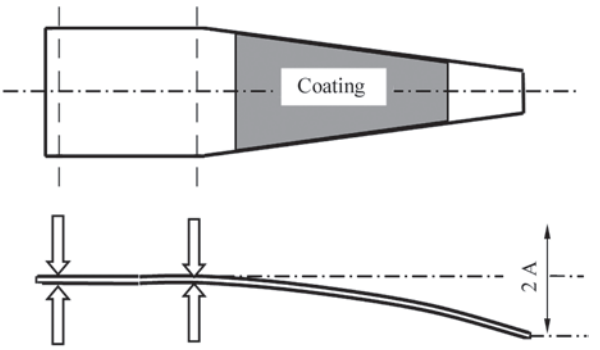

Figure 1. General appearance of substrate of a trapezoidal shape with the Co–20 % Fe coating for the study of DC characteristics of the substrate-coating system

Examination of the coating microstructure was carried out on witness specimens produced in identical conditions of deposition. For this purpose, plates of 5×10 mm of Ti-6-4 alloy were used, which were fixed near the substrate on its holder. Further, these witness specimens were mechanically cut into two parts, from which specimens for electron microscopic and X-ray examinations were made. Trapezoidal substrates with coating were not subjected to any treatment and were used further to determine the characteristics of their DC.

Figure 2 presents the overall appearance of the microstructure and the distribution of chemical elements over the thickness of the witness specimen cross-section. It is seen that the microstructure of the material is homogeneous, and there are no defects on the interface of the substrate with coating that contribute to the reduction of adhesion between them.

For X-ray structural analysis of Co–Fe coatings, the DRON-4M diffractometer in the radiation of the copper anode was used. Figure 3 presents the diffraction patterns of coatings, deposited under different conditions. It is seen that on both diffraction patterns, only maxima of BCC structure are present. Such a fact draws attention, that the ratio of intensities of diffraction peaks changes during the transition from

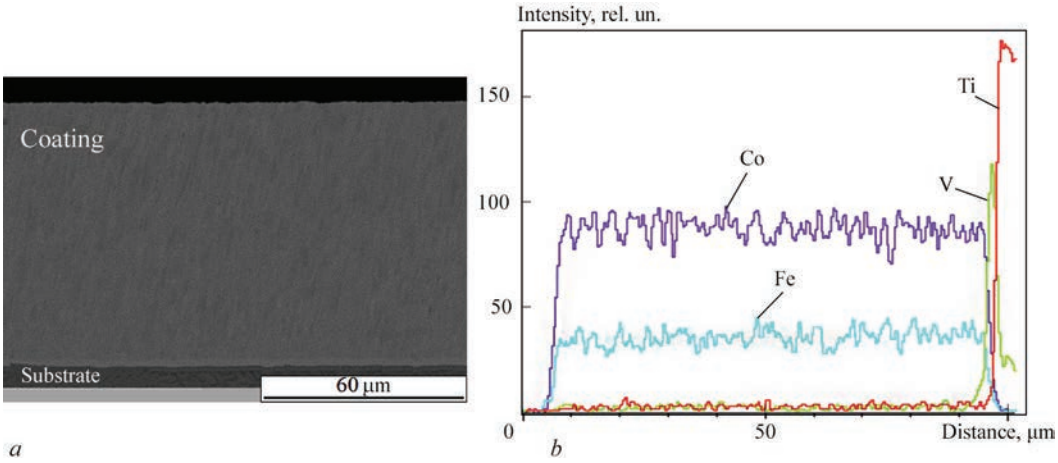

Figure 2. General appearance of microstructure (*a*) and distribution of chemical elements (*b*) according to the thickness of witness specimen cross-section with the Co–20 % Fe coating

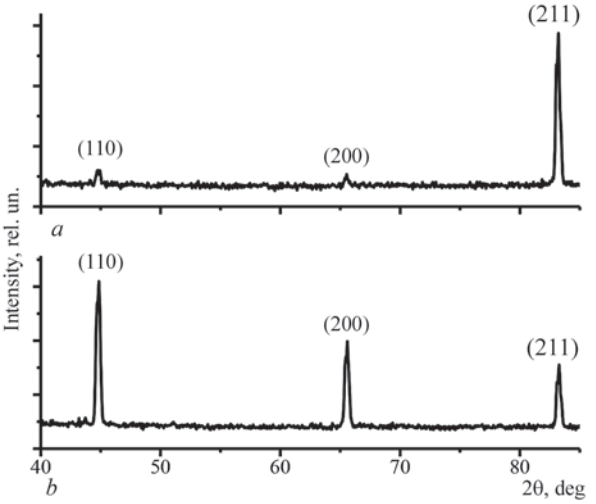

Figure 3. Diffraction pattern of Co–20 % Fe coatings deposited in the stationary conditions (*a*) and during substrate rotation (*b*)

the coatings produced in the stationary conditions and during substrate rotation.

The analysis of the crystallographic texture of the coatings was performed using an X-ray diffractometer DRON-3, equipped with a textured attached device, in CuK_α radiation. The measurements were carried out using a parallel beam geometry at scanning angles from 0 to 80° and from 0 to 360° for α and β, respectively. The data obtained on a nontextual $BaTiO_3$ specimen were used to record the defocusing effect. The analysis of crystallographic texture was carried out by constructing straight and reverse pole figures (PF) by means of the MTEX Matlab software package [14].

DAMPING PROPERTIES OF COATINGS

Figure 4 presents amplitude dependences of LD reflecting DC of substrate-coating systems, obtained in the conditions of stationary and nonstationary deposition of coatings. It is seen that DC of both oscillating systems is several times higher than that of the substrate without coating. Moreover, in the case of coating deposited with a stationary substrate, the level of DC is significantly higher compared to the coating deposited on a rotating substrate.

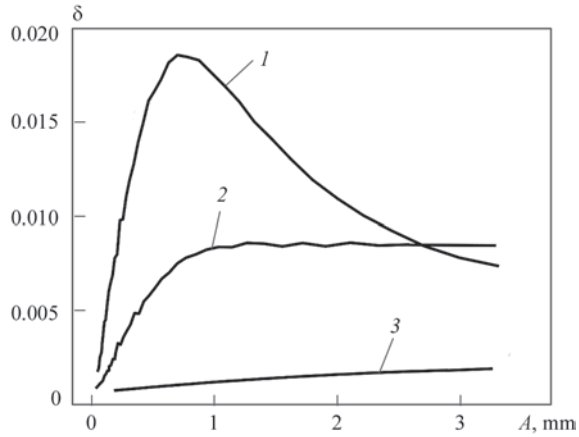

Figure 4. Amplitude dependences of LD for substrates with Co–20 % Fe coatings deposited on a stationary substrate (*1*), substrate during rotation (*2*) and for a substrate without coating (*3*)

Figure 5 presents the calculated amplitude dependences of intrinsic of DC for the coating material produced in the stationary and nonstationary conditions of deposition. It can be noted that the level of DC of the coating produced in the stationary conditions is almost twice higher than that of the coating deposited in the nonstationary conditions. From the comparison of the shape of the curves of amplitude dependences, it is seen that for the coating deposited in the stationary conditions, the rate of decrease of the curve for the descending part of the maximum is sharper.

The height and profile of the MMA maximum are determined by saturation magnetostriction and residual stresses [5]. Taking into account that the magnitude of the magnetostriction of the material depends on its texture [6], it was assumed that the differences in the amplitude dependence curves of DC of Co–Fe coating materials produced under different conditions of their deposition (Figure 5) are predetermined by their different texture.

MICROSTRUCTURE OF COATINGS

The characteristic microstructure of the Co–20 % Fe coating is shown in Figure 6. It is seen that the coating

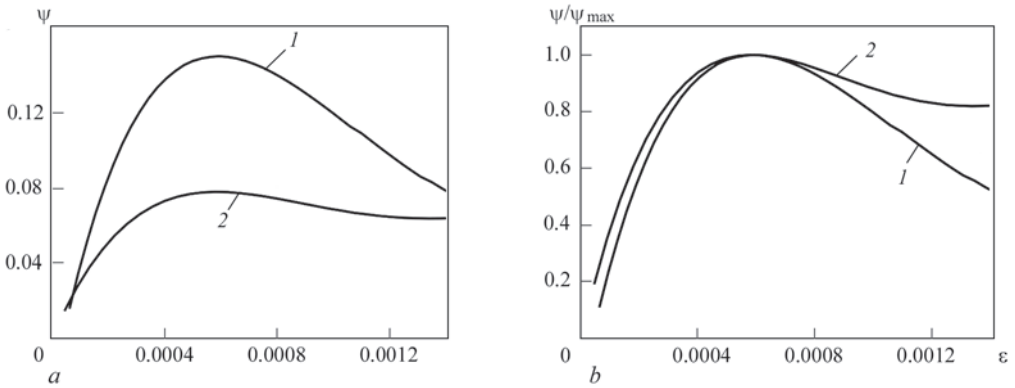

Figure 5. Amplitude dependences of energy loss coefficient (ψ = 2δ, where δ is the intrinsic of LD) of intrinsic (*a*) and values normalized to the maximum (ψ_{max}) (*b*) for Co–20 % Fe coatings deposited in the stationary (*1*) and nonstationary (*2*) conditions

consists of columnar grains oriented perpendicular to the surface of the substrate.

It turned out that such coatings are characterized not only by the elongation of grains in the direction of their growth, but also by the presence of a certain predominant crystallographic orientation. In Figure 7, *a*, PF (110), (100) and (211) are presented, built for the Co–20 % Fe coating, deposited in the stationary conditions. It is seen that the distribution of density of the poles (110) and (100) has a circumferential character. Taking into account the angular distance of the circumferential distributions, it was concluded that this type of pole density distribution can be obtained in the case of fiber texture with a predominant orientation of crystallites in the <111> direction. Figure 7, *b* presents PF of the Co–20 % Fe coating deposited in the nonstationary conditions. It is seen that also in this case, a fiber texture is formed. However, the grains are mainly oriented along the <100> axis, where the maximum pole density is observed in the center of PF.

To evaluate the volume fraction of crystallites characterized by different orientations based on the obtained results on the distribution of pole density, inverse PF were built. Figure 8 presents inverse PF built for the Co–20 % Fe coatings deposited in the stationary and nonstationary conditions. It is seen that in the case of coating deposited in the stationary conditions, the fiber texture is a single-component of <111> type,

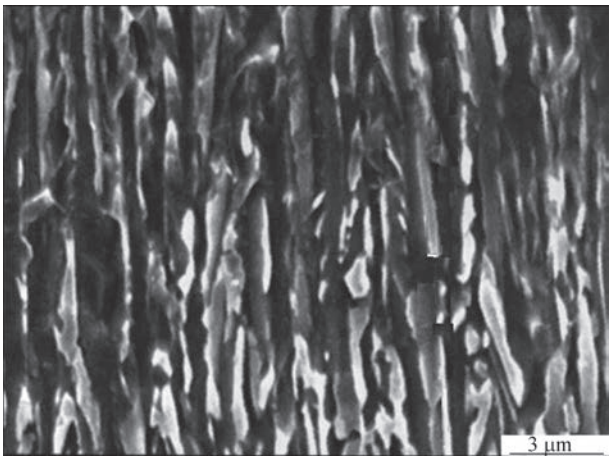

Figure 6. Cross-sectional microstructure of Co–20 % Fe coating etched to reveal grain boundaries

and in a coating produced in the nonstationary conditions, it is a multicomponent <100> + <111> + <110>. Moreover, the volume fractions of the components differ. The largest volume fraction is characteristic of the component of the fiber texture of <100> type and the smallest is typical of <110> component (Table 1).

It is seen that, despite the presence of <111> and <110> components, the <100> texture component is dominant in the multicomponent texture of a coating deposited in the nonstationary conditions. A coating deposited in the stationary conditions has a one-component fiber texture <111>.

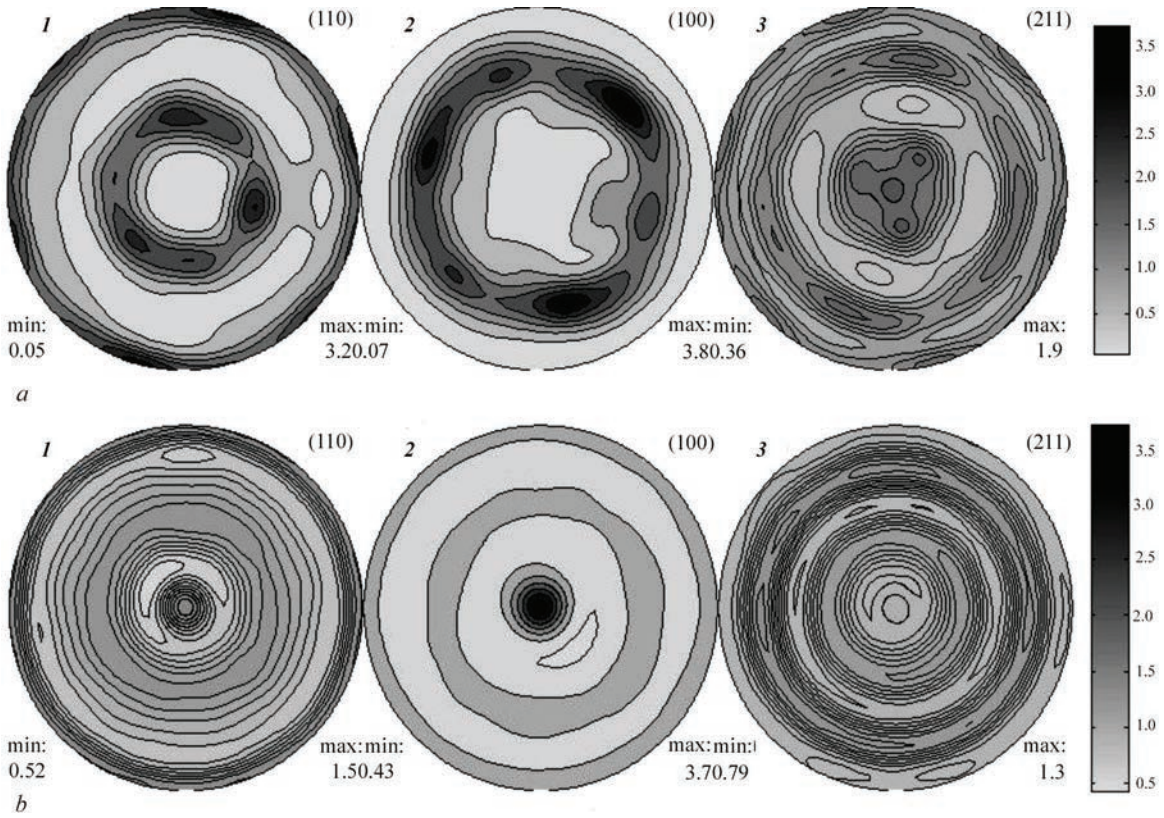

Figure 7. Distribution of pole density for Co–20 % Fe coatings deposited on the surface of a titanium plate in the stationary (*a*) and nonstationary (*b*) conditions: *1* — (110); *2* — (100); *3* — (211)

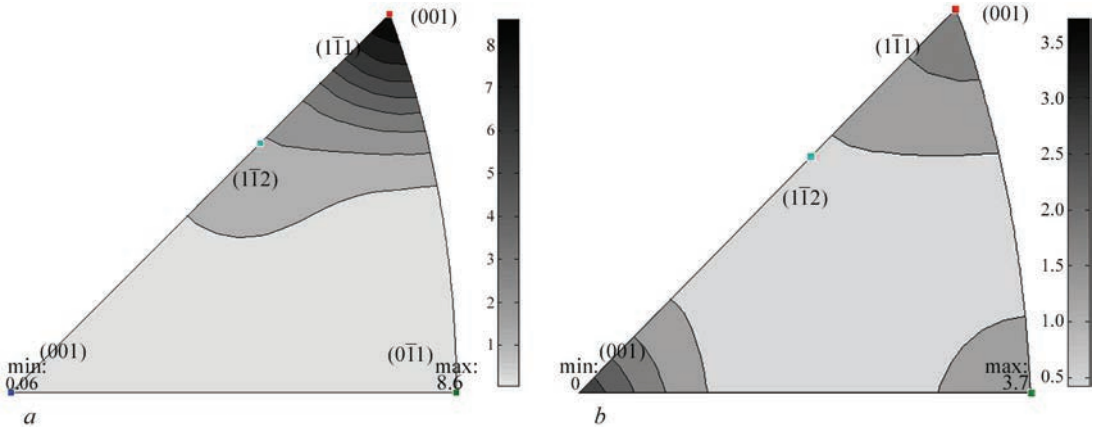

Figure 8. Inverse PF built in the direction perpendicular to the surface of Co–20 % Fe coating deposited in the stationary (*a*) and nonstationary (*b*) conditions

EFFECT OF TEXTURE ON THE DC AMPLITUDE DEPENDENCE OF COATINGS

According to the Smith–Birchak model [5], the height of the MMA maximum in the materials with BCC lattice is determined by the dependence:

$$\left(\frac{\Delta U}{U}\right)_{\max} = \frac{3KE\lambda_s}{2\Delta\sigma_i} \times \times\left\{1-\left[\left(1-\frac{\Delta\sigma_i}{\sigma_i}\right)\Big/\left(1+\frac{\Delta\sigma_i}{\sigma_i}\right)\right]^{2/3}\right\}, \quad (1)$$

where K is the constant that depends on the shape of the hysteresis loop; E is the modulus of elasticity; λ_s is the saturation magnetostriction; $\Delta\sigma_i$ is the dispersion of value of internal stresses; σ_i is the average value of internal stresses.

In [6] it was shown that the value of λ_s is determined by the type of fiber texture of the material and the direction of application of alternating deformations. Based on the obtained data on the texture of the coatings and taking into account the direction of their deformation during oscillations of flat specimens, the values of λ_s for the coatings with different texture (Table 2) were calculated, using the procedure [6] and experimental values of magnetostriction for Co–Fe alloy along the crystallographic <100> and <111> directions [15].

To evaluate the influence of the texture type, let us calculate the amplitude dependence of the energy loss coefficient ψ for the coatings with different fiber textures. According to the Smith–Birchak model, this dependence is determined by the expression:

$$\psi = (2KE\lambda_s/\sigma_i)\{[1 - \exp(-2x)\times \times(1 + 2x + 2x^2)]/x^2\}, \quad (2)$$

where $x = \sigma/\sigma_i$; σ is the amplitude of alternating stresses of the oscillating specimen.

In [2] it is shown that a satisfactory correspondence between the experimentally measured values of DC of the specimen for different oscillation amplitudes and values calculated by the formula (2) can be obtained in the condition that the value of the internal stresses is σ_i = 17.5 MPa.

In Figure 9, *a*, the amplitude dependences of the energy loss coefficient of the coating material with different types of texture are given. It is seen that when the type of fiber texture changes, the height of the DC maximum changes: the largest value is observed in the case of the fiber texture of <111> type, and the smallest value is <100>. However, the shape of the amplitude dependence of DC for the coatings with different texture remains unchanged (Figure 9, *b*).

Comparing these dependencies with the experimental results obtained for the coatings with different types of fiber texture (Figure 5), it can be assumed that a change in the type of fiber texture of the coating can only lead to a decrease in the level of DC. At the same time, the experimental amplitude dependences of the energy loss coefficient for the coatings produced under different conditions show not only a decrease in the value of the DC maximum, but also

Table 1. Characteristics of fiber textures of specimens produced in the process of deposition of Co–20 % Fe alloy on titanium substrates

Conditions of coating deposition	Volume fraction of texture components		
	<110>	<100>	<111>
Stationary	0.0	0.0	1.0
Nonstationary	0.16	0.6	0.24

Table 2. Magnitude of magnetostriction of Co–20 % Fe coating saturation with different types of fiber texture under its tension/compression

Type of fiber texture of coating	<100>	<110>	<111>
Magnitude of saturation magnetostriction, 10^{-6}	93.9	119.1	127.5

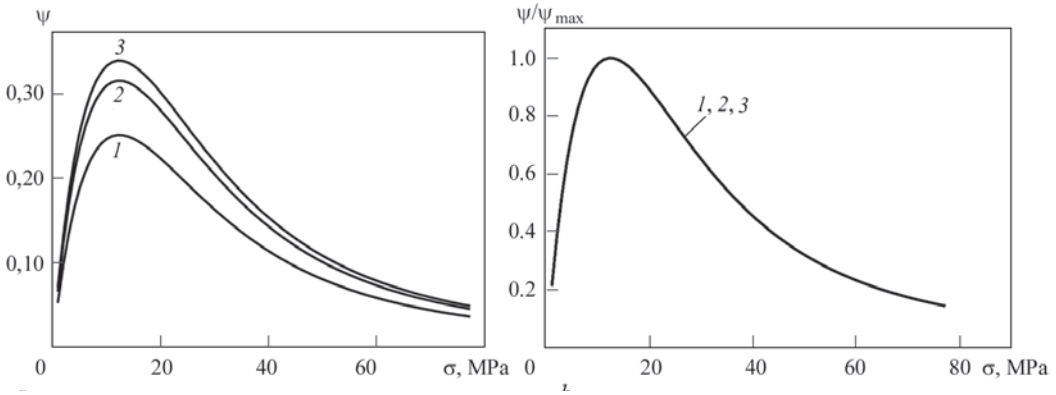

Figure 9. Amplitude dependences of energy loss coefficient of coatings with fiber textures of <100> (*1*), <110> (*2*) and <111> (*3*) type at the same level of internal stresses (*a*) and normalized to the maximum value ψ_{max} (*b*)

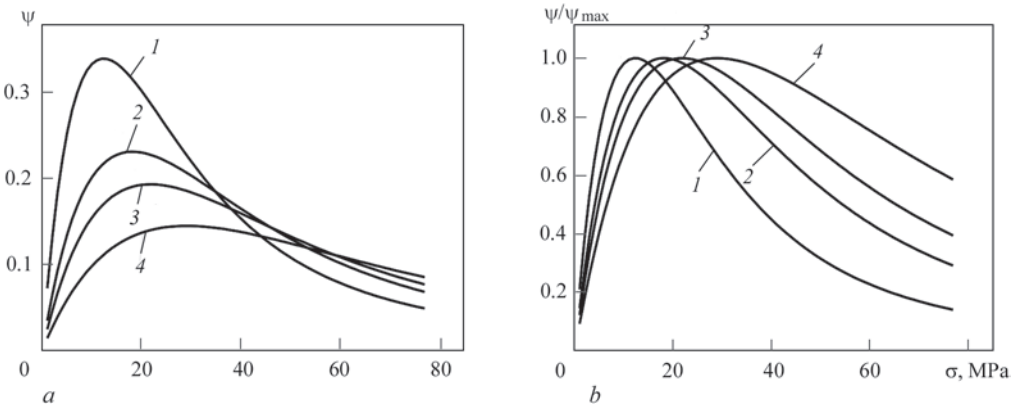

Figure 10. Amplitude dependences of the energy loss coefficient of coatings with a fiber texture of <111> type at different levels of internal stress σ_i, MPa: *1* — 17.5; *2* — 25; *3* — 30; *4* — 40 (*a*) and normalized to the maximum value ψ_{max} (*b*)

its shape (the maximum is blurred towards larger deformation amplitudes). Therefore, it was assumed that such a phenomenon may be associated with a change in internal stresses in the coatings produced under different conditions. To find out this possibility, the amplitude dependences of the energy loss coefficient of the coating material with different levels of internal stresses were calculated.

From the calculated amplitude dependences of the energy loss coefficient of the coating material with the same type of fiber texture, but with different levels of internal stresses presented in Figure 10, it is seen that when the internal stresses grow, the height of the peak decreases, shifts and expands towards larger stress amplitudes during a alternating deformation.

According to the obtained modeling results, it can be assumed that when the conditions for coating production change, variation in their amplitude dependence of DC is mainly predetermined by the change in the fiber texture of the coatings from a single-component one of <111> type, which is formed in the stationary conditions of deposition, to a multicomponent <100> + <111> + <110>, formed in the nonstationary conditions of deposition. However, since, as is seen from Figure 5, for the coatings deposited in the nonstationary conditions, not only a decrease in the height of the maximum on the amplitude dependence of DC is observed, but also its blurring, it can be assumed that such changes are predetermined by an increase in the level of internal stresses in the coatings with a multicomponent texture.

CONCLUSIONS

1. DC of titanium plates with the coatings of ferromagnetic Co–20 % Fe alloy changes depending on the conditions of coating deposition. In the stationary conditions of their deposition, the characteristics of DC of the substrate-coating system are described by a curve with a maximum, and in the nonstationary conditions, they are described by a curve with the saturation on the side of large amplitudes of oscillations.

2. Intrinsic of DC of the Co–20 % Fe coatings formed in the stationary conditions are approximately twice as large as those of the coatings produced in the nonstationary conditions.

3. It was determined that the conditions of deposition of the Co–20 % Fe coatings affect the characteristics of the coating material texture. In the stationary conditions of deposition, a fiber texture of <111> type is formed, and in the nonstationary conditions, a multicomponent texture of <100> + <111> + <110> type is formed.

4. The level of DC of the Co–20 % Fe coatings with a fiber texture of <111> type is predetermined by a high value of the magnetostriction magnitude, which is consistent with the Smith-Birchak model for magnetomechanical damping.

5. A decrease in the level of damping in the Co–20 % Fe coatings with a multicomponent fiber texture of <100> + <111> + <110> type can be a consequence of both a decrease in the average value of the magnetostriction magnitude as well as an increase in the level of internal stresses.

REFERENCES

1. Matveev, V.V. (1985) *Vibration damping of deformed bodies*. Kyiv, Naukova Dumka [in Russian].
2. Yen, H.-Y., Herman Shen, M.-H. (2001) Passive vibration suppression of beams and blades using magnetomechanical coating. *J. of Sound and Vibration*, 245(**4**), 701–714. DOI: https://doi.org/10.1006/jsvi.2001.3561
3. Torvik, J., Langley, B. (2015) Material properties of hard coatings developed for high damping. In: *Proc. of 51st AIAA/SAE/ASEE Joint Propulsion Conf. (Orlando, Florida, USA, July 29, 2015)*, 4195. DOI: https://doi.org/10.2514/6.2015-4195
4. Ustinov, A.I., Movchan, B.A., Lemke, F., Skorodzievskii, V.S. (2001) Damping capacity of Co–Ni and Co–Fe coatings produced by electron-beam deposition. *Vibr. Tekh. Tekhnol.*, **4**, 123–126 [in Russian].
5. Smith, G.W., Birchak, J.R. (1969) Internal stress distribution theory of magnetomechanical hysteresis-an extension to include effects of magnetic field and applied stress. *J. Appl. Phys.*, **40**, 5174–5178. DOI: https://doi.org/10.1063/1.1657370
6. Frank, R.C., Johnson, B.G., Schroeder, C.W. (1969) Crystal orientation and magnetomechanical damping of torsional vibrations. *J. Appl. Phys.*, **40**, 3189–3192. DOI: https://doi.org/10.1063/1.1658164
7. Movchan, B.A., Demchishin, A.V. (1969) A study of the structure and properties of thick vacuum condensates of nickel, titanium, tungsten, aluminum oxide and zirconium dioxide. *Fiz. Metall. Metalloved.*, 28(**4**), 653–660 [in Russian].
8. Ustinov, A.I., Fesyun, E.V., Melnichenko, T.V., Romanenko, S.M. (2007) Effect of substrate temperature on micro- and substructure of copper condensates deposited from a vapor phase. *Advances in Electrometallurgy*, **4**, 18–24.
9. Ustinov, A.I., Skorodzievskii, V.S., Fesiun, E.V., Taranenko, V.N. (2012) Structure and mechanical properties of nanostructured vacuum nickel condensates. *Nanosystemy, Nanomaterialy, Nanotekhnologii*, 10(**1**), 11–18 [in Russian].
10. Ustinov, A.I., Movchan, B.A., Skorodzievskii, V.S. et al. (2004) Effect of thermomechanical treatment onto damping capacity Co–20 % Fe coatings. *Vibr. Tekh. Tekhnol.*, **3**, 104–106 [in Russian].
11. *Herman* Shen, M.-H. (2008) *Free layer blade damper by magneto-mechanical materials*. United States. Pat. WO 2008/127375 A1.
12. Ustinov, A.I., Nekrasov, A.A., Perederiy, V.A. et al. (2012) Device for dissipative properties research of metallic flat samples and coatings. *Zavod. Laboratoriya*, **10**, 41–44 [in Russian].
13. Ustinov, A.I., Skorodzievskii, V.S., Kosenko, N.S. (2007) A study of the dissipative properties of homogeneous materials deposited as coatings. Pt 1. Method for the determination of the amplitude dependence of the true vibration decrement of the coating material. *Strength Mater.*, 39(**6**), 663–670. DOI: https://doi.org/10.1007/s11223-007-0076-3
14. Hielscher, R., Schaeben, H. (2008) A novel pole figure inversion method: Specification of the MTEX algorithm. *J. Appl. Cryst.*, **41**, 1024–1037. DOI: https://doi.org/10.1107/s0021889808030112
15. Noro, S., Ohtake, M., Kawai, T. et al. (2022) Magnetostrictive properties of Co–Fe alloy epitaxial thin films with Co-rich composition. *AIP Advances*, **12**, 035144. DOI: https://doi.org/10.1063/9.0000352

ORCID

O.S. Kremenchutskyi: 0000-0001-7650-0122,
S.S. Polishchuk: 0000-0002-8403-5360

CONFLICT OF INTEREST

The Authors declare no conflict of interest

CORRESPONDING AUTHOR

O.S. Kremenchutskyi
E.O. Paton Electric Welding Institute of the NASU
11 Kazymyr Malevych Str., 03150, Kyiv, Ukraine.
E-mail: kremens44@gmail.com

SUGGESTED CITATION

O.S. Kremenchutskyi, S.S. Polishchuk (2024) Effect of the texture of ferromagnetic Co–Fe coatings on their damping capacity. *The Paton Welding J.*, **1**, 36–42.

JOURNAL HOME PAGE

https://patonpublishinghouse.com/eng/journals/tpwj

Received: 14.11.2023
Received in revised form: 07.12.2023
Accepted: 22.01.2024

DOI: https://doi.org/10.37434/tpwj2024.01.07

NITROGEN ABSORPTION BY 04Cr18NI10 STEEL IN PLASMA-ARC MELTING UNDER SLAG OF $CaO–Al_2O_3$ SYSTEM

V.O. Shapovalov[1], **V.G. Mogylatenko**[1,2], **R.V. Lyutyi**[2], **R.V. Kozin**[1]

[1]E.O. Paton Electric Welding Institute of the NASU
11 Kazymyr Malevych Str., 03150, Kyiv, Ukraine
[2]National Technical University of Ukraine "Igor Sikorsky Kyiv Polytechnic Institute"
37 Prospect Beresteiskyi (former Peremohy), 03056, Kyiv, Ukraine

ABSTRACT

Nitrogen as an alloying element of steel is a strong austenitizer, and it has an essential influence on mechanical properties of steels of different grades. It is rational to use gas phases for nitrogen alloying, and the process can be intensified with the application of highly-concentrated energy sources, for instance, plasma. One of the determining factors of metal alloying is the partial pressure of nitrogen and the process temperature. It is difficult to find works, dealing with nitriding of metal melts in plasma-slag process. The paper gives experimental data on dissolution kinetics and nitrogen solubility in 04Cr18Ni10 steel. The derived mathematical models of nitrogen dissolution in plasma melting are highly significant, which is indicated by the respective determination coefficients. At less than 0.1 atm partial pressure of nitrogen above the melt, the temperature in the range of 1823–2323 K practically does not influence the content of nitrogen in steel, and at a higher partial pressure, the content of nitrogen in steel decreases with the temperature rise. The melt temperature under the experimental conditions was assessed as 2385 K. It was determined that the coefficient of nitrogen distribution between the metal and slag changes only slightly at up to 1 atm partial pressure of nitrogen and is equal to 1.1–1.2.

KEYWORDS: nitrogen-containing steels, plasma-slag melting, nitrogen, absorption kinetics, solubility, distribution coefficient

INTRODUCTION

04Cr18Ni10 steel, along with other chromium-nickel steels, is one of the most common structural austenitic steels used in industry, as its products can operate in various aggressive environments (solutions of salts, alkalis, acids) and has an operating temperature of up to 900 K under the normal conditions and up to 600 K in aggressive environments.

Any high-temperature metallurgical process of steel production is a process of interaction of several phases. As a rule, it is liquid metal, liquid slag and gas phase or vacuum. The main gases interacting with the slag and metal are oxygen, hydrogen and nitrogen. The presence of the first two gases in the gas atmosphere in the absence of melt protection inevitably leads to the formation of defects in ingots and castings: nonmetallic inclusions, gas and gas shrinkage porosity, flakes. And only nitrogen can perform both a negative and a positive function. The first one consists in the formation of strengthening inclusions in steel under certain conditions, and the second one is in the fact that nitrogen is a substitute for nickel.

Nitrogen, known for a long time [1, 2] as an alloying element of chromium-nickel and chromium-manganese steels, is a strong austenizer along with nickel. The effect of nitrogen in the γ-region of iron is several times stronger than the effect of nickel. It is known that 0.15 % of nitrogen in chromium-nickel steels is equivalent to 2–4 % Ni, and 0.25 % of nitrogen is equivalent to 2.5–6.0 % Ni. Considering the cost of nickel, substitution of its part with nitrogen significantly increases the cost-effectiveness of stainless steel production [3].

Nitrogen-containing steels with an over-equilibrium nitrogen content should be melted under the excess nitrogen pressure or by the plasma-arc remelting (PAR) method with alloying of metal with nitrogen directly from the gas phase. Arc-slag remelting (ASR) [4] allows performing alloying of metal with nitrogen from the gas phase and treatment of metal with slag. Thus, the formation of ingots of various cross-sections is provided, that have satisfactory surface, chemical and structural homogeneity. The nitrogen content in steel is determined by the composition of the slag and, depending on the method of melting, changes both in the metal and in the slag.

The process of alloying steels with nitrogen from plasma is characterized by a high rate of gas absorption by the liquid metal, which is an order of magnitude higher than in conventional metallurgical units. Therefore, plasma-slag remelting (PSR), which combines plasma as a source of metal heating and activation of nitrogen molecules, with slag treatment to refine the melt from undesired impurities and nonme-

tallic inclusions, is more promising from the point of view of obtaining an superequilibrium nitrogen content in the metal.

Taking into account that the absorption of nitrogen by liquid steel in the ternary gas–slag–metal system depends on the transfer capacity of the slag, the problem of studying the kinetics of the process of nitrogen absorption by the slag and through the slag by metal during plasma-slag melting on the example of steel 04Cr18Ni10 arises.

STATE OF THE PROBLEM

Nitrogen significantly affects the mechanical properties, phase stability, corrosion and heat-resistant properties, crack resistance and fatigue strength of ledeburite tool and high-speed steels, stainless steels of the austenitic, ferritic-austenitic, ferritic-martensitic and martensitic grades [5–8]. The effect of nitrogen on the strength of austenitic steels is stronger than the effect of carbon (Table 1).

Melting in a nitrogen-containing gas environment, especially at elevated pressure, allows alloying with nitrogen directly from the gas phase. Plasma-arc remelting (PAR) provides a higher efficiency of alloying steel with nitrogen at a low gas pressure compared to pressure melting [9]. For chromium-manganese steels scarcely alloyed with nickel, such as Cr21Mn10NNi4, plasma-arc melting at nitrogen partial pressures of 60–120 kPa allows obtaining a nitrogen content that exceeds its standard solubility. The content of nitrogen in ingots during PAR is regulated by the change in the partial pressure of nitrogen in the plasma-forming gas, the total pressure in the melting chamber of the furnace, and the rate of ingot extraction, i.e., the melt temperature [9].

Thus, the partial pressure of nitrogen in the plasma-forming gas and the process temperature are one of the determining factors of alloying metal in an superequilibrium amount with nitrogen during PAR.

SOLUBILITY OF NITROGEN IN METAL MELT

The equilibrium solubility of nitrogen in the metal melt is subjected to the Sieverts' law or the square root law:

Table 1. Influence of alloying elements (1 %) on yield strength of 04Cr18Ni10 steel [2]

Alloying element	Type of solution	Yield strength of steel, kg/mm^2
N	Penetration	70
C	–»–	40
Cr	Substitution	0.4
Mo	–»–	1.5

$$[\mathrm{N}]_{\mathrm{Me}} = K_{\mathrm{N}}\sqrt{P_{\mathrm{N_2}}},$$

where $[\mathrm{N}]_{\mathrm{Me}}$ is the equilibrium solubility of nitrogen, %; K_{N} is the Sieverts' constant, %·atm$^{-1/2}$; $P_{\mathrm{N_2}}$ is the equilibrium partial pressure of nitrogen in the gas phase, atm.

During plasma heating, the square root law for nitrogen absorption is also fulfilled, but here the proportionality factor is much higher than the Sieverts' constant. Alloying of metal with nitrogen will occur if the inequality is observed [10]:

$$p_{\mathrm{N_2}} > P_{\mathrm{N_2}} = \left([\mathrm{N}]_{\mathrm{Me}} / K_{\mathrm{N}}\right)^2,$$

where $p_{\mathrm{N_2}}$ is the partial pressure of nitrogen in the gas phase.

The temperature dependence of the nitrogen dissolution constant in a liquid iron has been studied by many researchers. The most probable results are satisfactorily described by the equation [11]:

$$\lg K_{\mathrm{N_2}} = (-293/T) - 1.16.$$

According to the specified dependence at 1600 °C, $K_{\mathrm{N_2}}$ = 0.048 %. Thus, for this temperature we can write:

$$[\mathrm{N}]_{\mathrm{Me}} = 0.048\sqrt{p_{\mathrm{N_2}}}.$$

Alloying elements and impurities in iron change the ability of iron to dissolve nitrogen [12].

In real steelmaking processes, nitrogen dissolution occurs in parallel with oxidation processes. A flow of oxygen causes a counter flow of nitrogen. It was established [13] that the behavior of nitrogen in Fe–C alloy and killed steel (0.3 % C) and 15MnAlTi steel as well as pure iron is determined by the rate of metal saturation with oxygen and when the maximum concentration of oxygen in metal is reached, the absorption of nitrogen by steels stops. The higher the rate of oxygen absorption, the sooner nitrogen absorption stops and the lower its concentration is achieved in steels.

The solubility of nitrogen in steels can be calculated theoretically having known values of interaction parameters [10]. In [14], a thermodynamic model for predicting the solubility of nitrogen in liquid stainless steels depending on the concentrations of alloying elements, temperature and pressure is given, which takes into account a new factor of the pressure effect on the coefficient of nitrogen activity. The results of the calculations, which agree well with the experiment, are subjected to the Sieverts' law. However, at a high pressure (> 1 atm) and especially at a high concentration of alloying elements, a deviation from the Sieverts' law occurs and the nitrogen pressure begins to negatively affect the solubility.

SOLUBILITY OF NITROGEN IN SLAGS

As for the sorption capacity of slag in relation to impurities, it depends on the oxidation-reduction potential of the medium, which can be determined by the equilibrium partial pressure of oxygen (P_{O_2}). Unlike the Sieverts' law for metals, in the case of slag, the following dependence is fulfilled [15]:

$$(G) = K_{(G)} p^{1/2}_{(G_2)} p^{V_G/4}_{(O_2)},$$

where V_G is the degree of oxidation or valence of G element in the slag.

Since the valence of nitrogen in the slag $V_N = -3$, then

$$(N) = K_{(N)} p^{1/2}_{(N_2)} p^{-3/4}_{(O_2)}.$$

If the slag contains carbon, the following reaction occurs:

$$C + ½\{O_2\} = \{CO\}.$$

At the same time, from 1 mole of oxygen, 2 moles of CO are formed, which reduce the partial pressure of nitrogen above the slag, which should be taken into account during calculations of the solubility. In real conditions, in the presence of nitride-forming elements due to the formation of nitrides, the maximum solubility of nitrogen in the slag usually does not exceed 2 % [15].

Unfortunately, in the scientific literature, absorption of nitrogen by slags is most often associated with the presence of carbon in the slag or in the atmosphere above the slag. Pure experiments without the influence of carbon are not available. According to [16, 17], the simultaneous increase in the concentrations of carbon and nitrogen, as well as reaching the saturation, indicate that nitrogen and carbon in the slag are combined into one compound, for example, cyanide or cyanamide. Nitrogen at different content of CaO dissolves in the form of free nitrogen N^{3-} and binds to Ca^{2+} (Ca_3N_2) or Al^{3+} (AlN) ions. The mechanism of nitrogen dissolution is very complex, because, as is known, it reacts and substitutes all three types of slag oxygen: free (O^{2-}), final type (O^-) and bridging or one which combines (O°).

When carbon and nitrogen are dissolved simultaneously in molten slags [17] or there is carbon in the slag, they can be dissolved in the form of cyanide CN^-. In [17], analysis of literature data on the relationship between the solubility of nitrogen, cyanide,

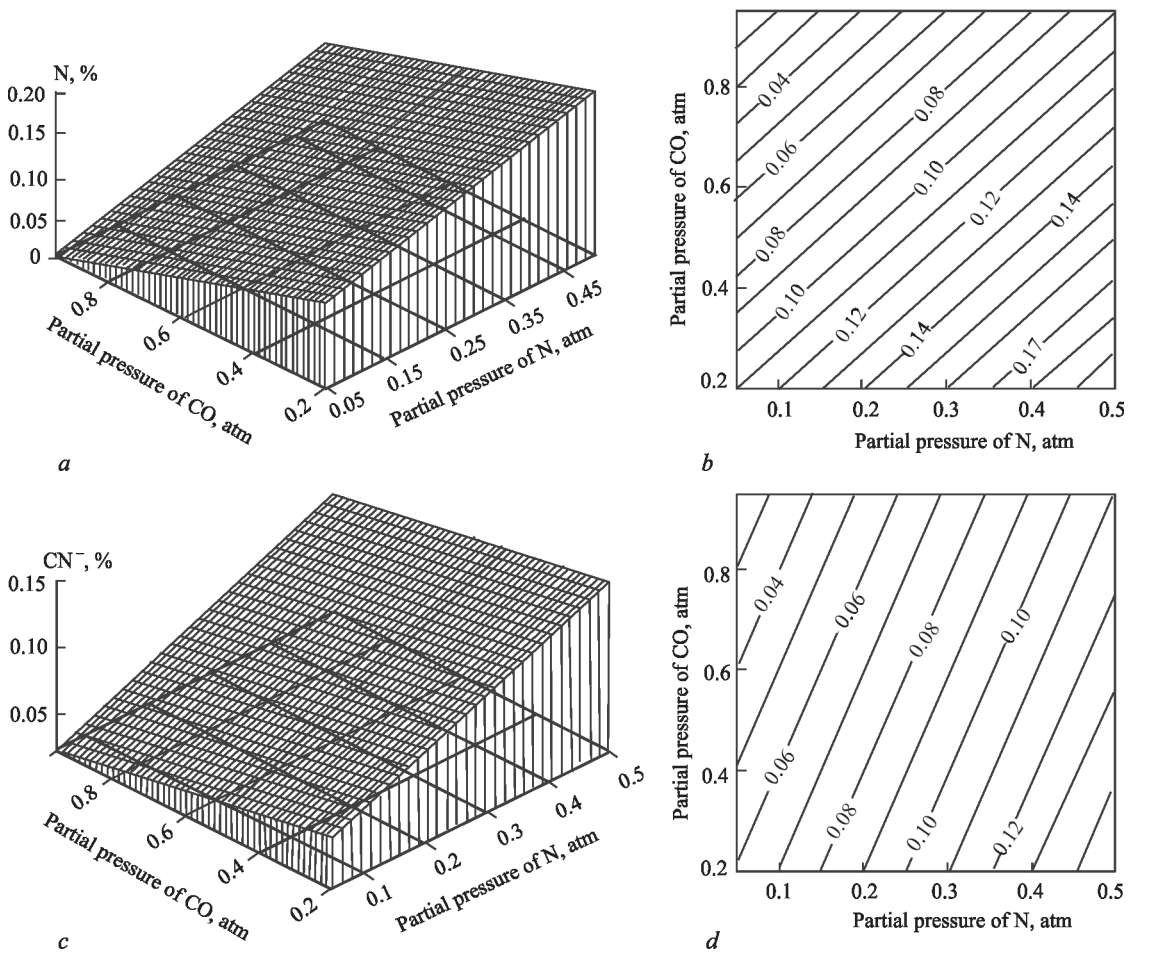

Figure 1. Dependence of total nitrogen content in the slag (*a*, *b*) and CN^- (*c*, *d*) on the partial pressure of nitrogen and CO above the slag 50 % CaO–50 % Al_2O_3 [17]: *a*, *c* — volume image; *b*, *d* — surface topography

and carbon in $CaO–Al_2O_3$ slag with the partial pressures of nitrogen, CO and argon in the system was performed, and model calculations of the solubility of nitrogen in various forms of existence in the slag were performed. Figure 1 shows the graphical dependences built based on the results of this work for 50 % CaO–50 % Al_2O_3 slag.

The main conclusions from these graphical dependencies are the following:

- both an increase in the partial pressure of nitrogen and a decrease in the partial pressure of CO above the slag lead to an increase in the content of nitrogen and cyanide CN^- in it;
- the partial pressures of nitrogen and CO have a stronger effect on the total nitrogen content than on the cyanide content;
- the higher partial pressure of CO, the higher the oxygen content and lower nitrogen content in the slag.

It is known that aluminium-oxygen anions of (AlO_2^-, AlO_3^{3-}, AlO_4^{5-}) slag as well as silicon-oxygen ones are able to associate with each other and form complex anions of large sizes [10]. During dissolution of nitrogen, it can be embedded in the complex anions instead of oxygen [18].

The solubility of nitrogen in the main slags two to three times exceeds the solubility of nitrogen in iron. In acidic slags with an increase in temperature, nitrogen dissolves almost three times faster [16] than in iron, which may be associated with the formation of complex anions. Studying the dependence between nitrogen and carbon content in ANF-7 (80 % CaF_2 + 20 % CaO) flux showed that the concentration of nitrogen in the initial flux is much lower than the equilibrium one and this slag not only cannot be a source for enrichment of metal with nitrogen, but can even facilitate the removal of this gas from it.

NITROGEN IN THE GAS–SLAG–METAL SYSTEM

The interaction in the nitrogen–slag–metal system consists of the following links: convection and diffusion transfer of nitrogen to the slag surface in the gas phase; adsorption, dissociation, transition of nitrogen atoms through the gas–slag interface; diffusion, convection and again diffusion transfer of nitrogen in the slag to the slag-metal interface; transition through the slag-metal interface; distribution of nitrogen over the volume of metal until equalizing the chemical potential of nitrogen in the metal phase (dissolution).

Depending on the speed of elementary links, one or the other link can determine the overall speed of the process.

The largest amount of information in the scientific literature concerns the interaction of nitrogen with melts based on iron, and at the second place — interaction with slags. A little attention is paid to the processes of saturation of melts with nitrogen from the gas phase through the slag. It was established [19] that nitriding from the gas phase is possible when the slag is deoxidized by metallic calcium and aluminium, but a clear dependence of the nitrogen content in Cr6WV steel on the content of oxygen in metal was not detected by the authors (Figure 2). Moreover, it can be said that the oxygen content in steel does not affect the content of nitrogen in it.

The content of nitrogen in Cr6WV steel, which is melted under $CaO–Al_2O_3$–15 % TiO_2 slag, is 0.035 %, and under Al-295 slag, it is 0.026 %. These values are lower than the equilibrium content (0.17 %) calculated for the conditions of interaction of liquid metal with nitrogen [19].

The amount of nitrogen dissolved in metal is directly proportional to the amount of slag nitrogen and inversely proportional to the distribution factor $L = \frac{(N)}{[N]}$. Taking into account the practical permanency of the dependencies shown in Figure 2, in the conditions of the experimentat, the coefficient of nitrogen distribution between the slag and metal does not change.

Nitriding of metal under the slag occurs at a lower rate, than in the case of contact of the metal melt directly with the gas phase [20]. The highest rate of nitriding is fixed in arc melting conditions ($2.6 \cdot 10^{-5}$–$1.55 \cdot 10^{-4}$ m/s), and the lowest is in melting in a resistance furnace ($(1.5–3.0) \cdot 10^{-6}$ m/s).

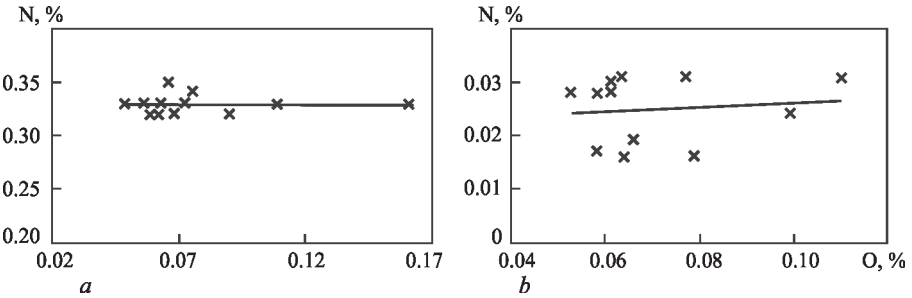

Figure 2. Effect of oxygen content in Cr6WV steel, melted under the deoxidated slag, on the content of nitrogen in it: *a* — ANF-1P + 7 % Ca slag; *b* — ANF-1P + 7 % Al [19]

Today, it is very difficult to find works that would combine kinetic dependences of the slag and steel saturation with nitrogen in a one process. Therefore, it was the aim of this work.

RESEARCH PROCEDURE

As a slag composition, binary slag of the composition of 50 % Al_2O_3 and 50 % CaO was selected. In the area of this concentration, there are low-melting slags with eutectic at a temperature of 1658–1668 K. To prepare slag, calcium oxide CaO powders and aluminium oxide Al_2O_3 of fine grade (clean for analysis) were used. The slags were preliminary melted in a graphite crucible in an induction furnace with a protective atmosphere. As a protective atmosphere, argon of the first grade was used: 0.002 % O_2; 0.01 % N_2; 0.03 g/m^3 of pair H_2O. The carbon content in the slag was 0.29 %, CaO — 49.3, Al_2O_3 — 50.

As a metal specimen, 04Cr18Ni10 steel of the following composition was used, %: 0.04 C, 18.1 Cr, 10.65 Ni, 0.8 Si, 1 Mn. This steel does not contain nitride-forming elements, that allows detecting nitrogen in the dissolved state.

The determination of nitrogen content in the slag and steel specimens was carried out in the equipment by the Kjeldahl procedure, which was updated in relation to the determination of nitrogen in slags, and its detailed description is given in [21].

The study of the kinetics of nitrogen absorption was carried out in the UPI installation [22], which allows studying the absorption of gas from plasma by the melt in the conditions, where its entire surface is covered with a plasma plume and active gas contacts with liquid pool.

After melting a weighted specimen of steel with the slag and its necessary holding in nitrogen-argon plasma, the plasmatron was switched off with simultaneous opening of the wedge mould for quenching the melt from liquid state and fixing the amount of nitrogen in it.

EXPERIMENTAL RESULTS AND THEIR DISCUSSION

The initial experiments were carried out with steel in contact with the gas atmosphere in the absence of a slag. The results are shown in Figure 3.

The main results of the statistical processing of the obtained results are as follows. Polynomial regression (dependence 1) has the following appearance:

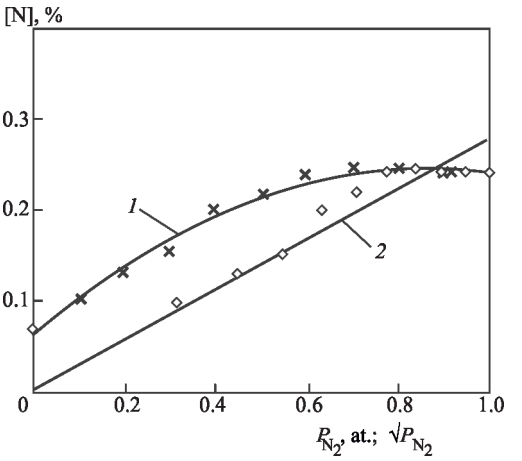

Figure 3. Content of nitrogen in 04Cr18Ni10 steel depending on the partial pressure of nitrogen above the metal (*1*) and the square root from this pressure (*2*)

$$[\%\ \mathrm{N}] = 0.0604545 + 0.0436667P_{N_2} - 0.257576P^2_{N_2}.$$

The coefficients of determination (R^2) are equal to 0.845973 and 0.982467 for degrees 0, 1 and 2, respectively. Zero value means that the first coefficient is a constant.

The dependence 2 in Figure 3 indicates that the content of nitrogen in the melt of 04Cr18Ni10 steel is subjected to the Sieverts' law. The Siverts constant for the conditions of the experiment amounts to 0.277674, and the obtained dependence is the following:

$$[\%\ \mathrm{N}] = 0.27764\sqrt{P_{N_2}}. \quad (1)$$

The coefficient of determination (R^2) is 0.979081, and the mean square deviation is 0.00091. The proximity of the coefficient of determination to 1 indicates that the model has a high significance.

The theoretical calculations were carried out to determine the solubility of nitrogen in the investigated steel. To do this, the Chipman–Corrigan equation was used [23]. The solubility of nitrogen in iron is described by the equation

$$\lg K_N = -\frac{850}{T} - 0.905 + \frac{1}{2}\lg p_{N_2}. \quad (2)$$

The interaction parameters [14, 23] of the first and second order required for the calculation are given in Table 2.

The equilibrium constant of nitrogen dissolution in liquid iron at a temperature (T) amounts to:

Table 2. Parameters of interaction of elements in iron at a temperature of 1873 K

Alloying element (*j*)	Cr	Ni	Mn	Si	C	Cr–Ni
1st order interaction parameter (e^j_N)	–0.047	0.0063	–0.02	0.047	0.118	–
2nd order interaction parameter (r^j_N)	0.00032	0.00007	0.000032	–	–	–0.00008

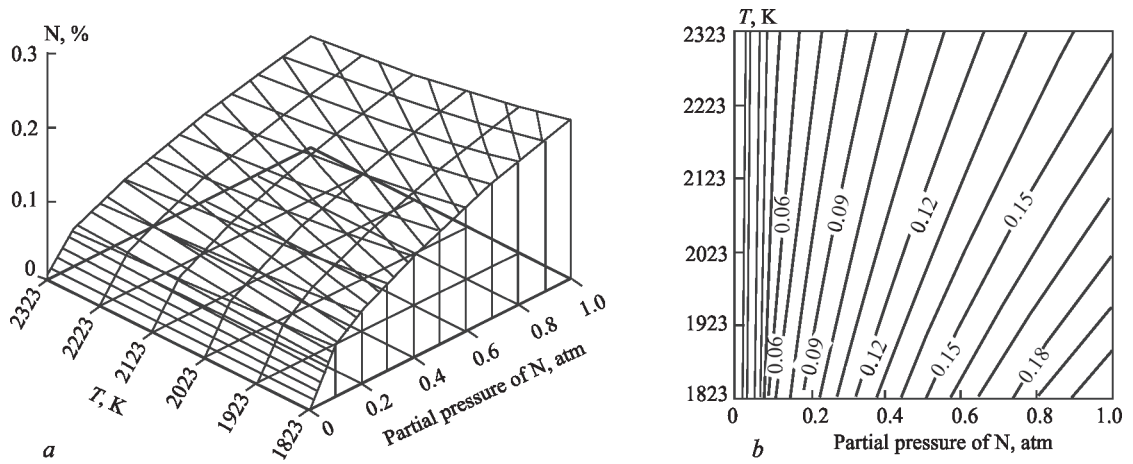

Figure 4. Effect of temperature and pressure of nitrogen on its content in 04Cr18Ni10 steel (*a*) and surface topography (*b*)

$$K_{\mathrm{N}} = \frac{f_{\mathrm{N}(T)}[\%\,\mathrm{N}]}{p_{\mathrm{N}_2}^{1/2}}. \qquad (3)$$

Tacking of the logarithm we have:

$$\lg[\%\,\mathrm{N}] = \frac{1}{2}\lg p_{\mathrm{N}_2} + \lg K_{\mathrm{N}} - \lg f_{\mathrm{N}(T)}. \qquad (4)$$

The activity coefficients at a certain temperature can be determined by the known data at a temperature of 1873 K and by the equation

$$\lg f_{\mathrm{N}(T)} = \left(\frac{3280}{T} - 0{,}75\right) \times \times \left\{\sum_j \left(e^j_{\mathrm{N}(1873)}[j]\right) + \sum_j \left(r^j_{\mathrm{N}(1873)}[j]^2\right) + \sum_j \sum_k \left(r^{j,k}_{\mathrm{N}}[j][k]\right)\right\}. \qquad (5)$$

Then after substitution of the equations (2) and (5) into the equation (4) we obtain:

$$\lg[\%\,\mathrm{N}] = \frac{1}{2}\lg p_{\mathrm{N}_2} - \frac{850}{T} - 0.905 - \left[\left(\frac{3280}{T} - 0.75\right)\left\{\sum_j \left(e^j_{\mathrm{N}(1873)}[j]\right) + \sum_j \left(r^j_{\mathrm{N}(1873)}[j]^2\right) + \sum_j \sum_k \left(r^{j,k}_{\mathrm{N}}[j][k]\right)\right\}\right]. \qquad (6)$$

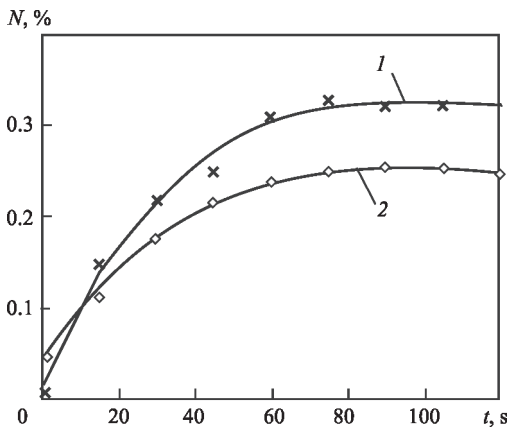

Figure 5. Kinetic dependence of nitrogen absorption at PSR (p_{N_2} = 0.7 atm): *1* — for slag; *2* — for steel

After the data is substituted, we obtain the equation:

$$[\%\,\mathrm{N}]_{\mathrm{04Kh18N10}} = \sqrt{p_{\mathrm{N}_2}}\, 10^{\left(\frac{1328}{T} - 1.4029\right)}. \qquad (7)$$

During plasma melting, the distribution of temperatures over the surface of the melt is very nonuniform. The region of the highest temperatures is concentrated inside the plasma plume and can reach 18000–19000 K [24]. On the axis of the nozzle section, depending on the electrical mode of melting, pressure and composition of the gas atmosphere, the temperature usually exceeds 12000 K, and the surface of the metal pool is not lower than 2000 K in the areas adjacent to the anode spot.

The obtained dependence (7) made it possible to evaluate the melt temperature at PSR. The experimental dependence of the nitrogen content in 04Cr18Ni10 steel is described by the dependence (1), and the dependence (7) shows the calculated change in the solubility of nitrogen in steel from the temperature.

It can be written that experimental and calculated values with the consideration of temperature are equal to each other:

$$[\%\,\mathrm{N}] = [\%\,\mathrm{N}]_{\mathrm{04Kh18N10}},$$

$$0.277674\sqrt{P_{\mathrm{N}_2}} = \sqrt{p_{\mathrm{N}_2}}\, 10^{\left(\frac{1328}{T} - 1.4029\right)},$$

from which the temperature of the steel melt is about 2385 K.

The results of the calculation by the formula (7) in graphical form are shown in Figure 4.

The obtained data showed that in the conditions of melting without the use of plasma at small partial pressures of nitrogen, of approximately up to 0.1 atm, the temperature within 1823–2323 K has practically no effect on the content of nitrogen in steel; at higher partial pressures with an increase in temperature,

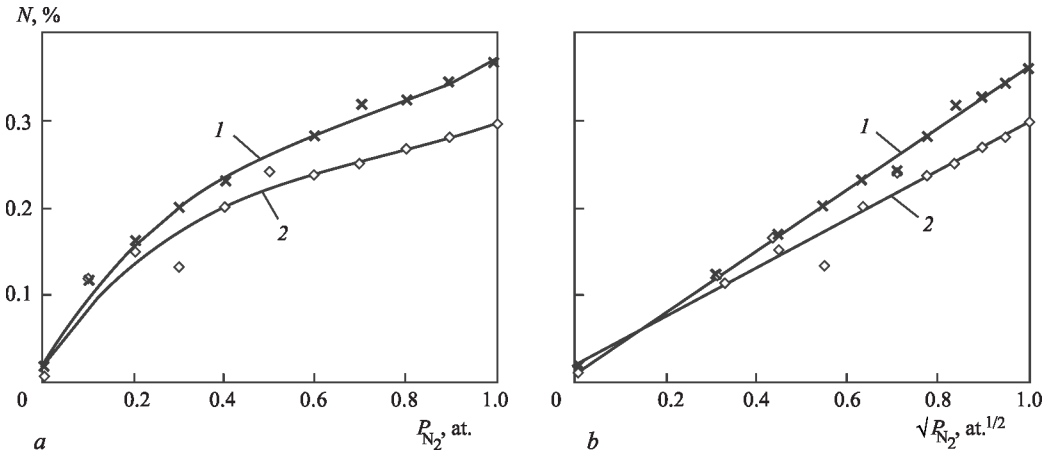

Figure 6. Effect of nitrogen pressure on the nitrogen content in the slag and 04Cr18Ni10 steel in PSR: *1* — slag; *2* — metal

the nitrogen content in the melt of 04Cr18Ni10 steel decreases; the maximum nitrogen content that can be achieved at a nitrogen pressure of 1 atm and a temperature of 2323 K is 0.145 %, and at a temperature of 1823 K and the same pressure it is 0.21 %.

The comparison of calculated and experimental data shows that the obtained calculated data are lower than the experimental, which may be associated with an increase in the energy of molecules in the plasma plume and the appearance of active nitrogen atoms and ions. It affects the intensity of gas absorption by the melt.

An example of a kinetic dependence of simultaneous nitrogen absorption by a liquid 04Cr18Ni10 steel and a slag at a partial nitrogen pressure of 0.7 atm in the furnace atmosphere is shown in Figure 5.

On all kinetic dependencies at pressures lower than 1 atm, the content of nitrogen in steel is lower than in the slag and not higher than in the steel produced at a direct contact of liquid metal with plasma.

The derived dependencies of changing the nitrogen content in the molten PSR steel on the partial pressure of nitrogen and the square root from this pressure are shown in Figure 6.

In the conditions of plasma-slag melting, the content of nitrogen in steel grows with an increase in the nitrogen pressure in the atmosphere above the melt (Figure 6, *a*) and is subjected to the Sieverts' law (Figure 6, *b*).

The linear dependence of the nitrogen content in the slag is described by the equation

$$(\%\,\mathrm{N}) = 0.360025\sqrt{p_{\mathrm{N}_2}} + 0.00336233 \qquad (8)$$

with the coefficient of determination R^2 = 0.995207 and the mean square deviation of $6.31644\cdot10^{-5}$, which indicates a high significance of the model. The free member of the last equation indicates the initial (residual) content of nitrogen in the slag.

The same can be said about the dependence of the nitrogen content in steel under the slag. The linear dependence is as follows:

$$[\%\,\mathrm{N}] = 0.286549\sqrt{p_{\mathrm{N}_2}} + 0.0129405, \qquad (9)$$

the coefficient of determination is 0.964987, and the mean square deviation is $3.01468\cdot10^{-4}$. The comparison of the Sieverts' constant of steel in PSR (1) with the constant in PAR (9) shows the proximity of their values. The difference amounts to 0.008875, which corresponds to 3.2 % of the error.

The coefficient of the nitrogen distribution between the slag and metal $\left(L = \frac{(\mathrm{N})}{[\mathrm{N}]}\right)$ determined according to the obtained data at a partial nitrogen pressure of not more than 1 atm changes slightly and is equal to 1.1–1.2.

CONCLUSIONS

1. The kinetic dependences of nitrogen absorption by a liquid 04Cr18Ni10 steel from nitrogen-argon plasma were obtained in the range of nitrogen partial pressure from 0.05 to 1.0 atm. In all cases, the nitrogen content in the slag exceeded its content in steel. It was determined that in plasma-slag melting, the absorption of nitrogen by the slag and 04Cr18Ni10 steel occurs in accordance with the Sieverts' law. The obtained mathematical models of nitrogen dissolution in plasma melting have a high significance and their coefficients of determination are close to 1. The value of the Sieverts' constant in the conditions of both plasma-slag melting, as well as by the calculation way in the equilibrium conditions for 04Cr18Ni10 steel was experimentally determined.

2. It was determined that at a partial nitrogen pressures of up to 0.1 atm and a temperature within 1823–2323 K, the content of nitrogen in steel is practically independent of the temperature unlike higher partial pressures. With an increase in temperature, the amount of equilibrium nitrogen dissolved in steel decreases.

3. It was established that in the conditions of the experiments, i.e., when the plasma plume complete-

ly covers the molten specimen, the melt temperature reaches 2385 K. In the conditions of PSR, the coefficient of nitrogen distribution between the slag and metal is 1.1–1.2.

REFERENCES

1. Houdremont, E. (1966) *Special steels*. Moscow, Metallurgiya [in Russian].
2. Lakomsky, V.I., Lakomsky, V.V. (2012) *Nitrogen in liquid steels and slags.* Kyiv, Naukova Dumka [in Russian].
3. Koroliov, M.L. (1961) *Nitrogen as an alloying element in steel.* Moscow, Metallurgizdat [in Russian].
4. Paton, B.E., Saenko, V.Ya., Pomarin, Yu.M. et al. (2004) Arc slag remelting for high strength steel & various alloys. *J. Mater. Sci*., **39**, 7269–7274. DOI: https://doi.org/10.1023/B:JMSC.0000048741.47509.b3
5. Cieśla, M., Ducki, K.J. (2008) Effect of increased nitrogen content on the structure and properties of tool steels. *J. of Achievements in Materials and Manufacturing Engineering*, 29(**1**), July. https://www.researchgate.net/publication/26872202
6. Cieśla, M., Ducki, K.J. (2008) Influence of increased nitrogen content on tool steels structure and selected properties. *J. of Achievements in Materials and Manufacturing Engineering*, 27(**2**), July. https://www.researchgate.net/publication/26872252
7. Saeed Nabil Ghali, Mamdouh Eissa, Hoda El-Faramawy et al. (2013) Production and application of advanced high nitrogen steel. In: *Proc. of Int. Conf. on Science and Technology of Ironmaking and Steelmaking (November 2013, Jamshedpur, India*). 1. https://www.researchgate.net/publication/262698868_Production_and_Application_of_Advanced_High_Nitrogen_steel
8. Grigorenko, G.M., Pomarin, Yu.M., Lakomsky, V.V. (2010) Properties of steels of X13 type, alloyed with nitrogen. *Sovrem. Elektrometal.,* **4**, 26–29 [in Russian].
9. Burnashev, V.P., Nikitenko, Yu.O., Yakusha, V.V. et al. (2020) Some aspects of melting high-nitrogen steel Kh21G17AN2 in plasma arc furnace. *Suchasna Elektrometall.,* **2**, 23–26 [in Ukrainian]. DOI: https://doi.org/10.37434/sem2020.02.04
10. Shurkhal, V.Ya., Larin, V.K., Chernega, D.F. et al. (2000) *Physical chemistry of metallurgical systems and processes:* Manual. Kyiv, Vyshcha Shkola [in Ukrainian].
11. Pomarin, Yu.M., Byalik, O.M., Grygorenko, G.M. (2007) *Influence of gases on structure and properties of metals and alloys.* Kyiv, NTUU KPI [in Ukrainian].
12. Shapovalov, V.O., Biktagirov, F.K., Mogylatenko, V.G. (2023) *Out-of-furnace processing of steel: Methods, processes, technologies*: Manual. Ed. by I.V. Krivtsun. Kyiv, Khimjest [in Ukrainian].
13. Enders, V.V. (2002) Nitrogen in steelmaking processes. *Lityo i Metallurgiya,* **1**, 95–100 [in Russian].
14. Zhouhua Jiang, Huabing Li, Zhaoping Chen et al. (2005). The nitrogen solubility in molten stainless steel. *Steel Research Int*., 76(**10**), 730–735. https://www.researchgate.net/publication/281642445
15. Grigoryan, V.A., Belyanchikov, L.N., Stomakhin, A.Ya. (1987) *Theoretical fundamentals of electric steelmaking processes.* Moscow, Metallurgiya [in Russian].
16. Grigorenko, G.M., Kozin, R.V. (2018) Nitrogen solubility in fluxes for electroslag technologies. *Suchasna Elektrometal.,* **2**, 37–40 [in Russian]. DOI: http://dx.doi.org/10.15407/sem2018.02.04
17. In-Ho Jung (2006) Thermodynamic modeling of gas solubility in molten slags (I)–carbon and nitrogen. *ISIJ International*, 46(**11**), 1577–1586.
18. Eloy Martinez, R., Victor Espejo, O., Francisco, Manjarrez (1993) The solubility of nitrogen in the CaO–CaF–Al_2O_3 system and its relationship with basicity. *ISIJ International*, 33(**1**), 48–52.
19. Lakomsky, V.V., Pomarin, Yu.M., Ryabtsev, A.D., Grigorenko, G.M. (2006) Metal nitriding from gas phase in ESR. *Sovrem. Elektrometall.*, **4**, 3–5 [in Russian].
20. Lakomsky, V.V., Grigorenko, G.M. (2012) Kinetics of gas phase nitrogen interaction with metal covered with molten slag. *Sovrem. Elektrometall.,* **3**, 35–37 [in Russian].
21. Kozin, R.V., Kuznetsova, L.V., Gulyanytska, N.E., Mossokovska, I.A. (2019) Determination of nitrogen content in CaO–Al_2O_3 systems by Kjeldahl method. *Metrologiya ta Prylady,* **3**, 55–60 [in Ukrainian].
22. Zabarilo, O.S., Lakomsky, V.I. (1968) Carbon behavior in plasma-arc remelting of alloy 50N and Armco iron. *Spec. Elektrometallurgiya,* **4**, 78–85 [in Russian].
23. Grigoryan, V.A., Stomakhin, A.Ya., Utochkin, Yu.I. et al. (2007) *Physical-chemical calculations of electric steelmaking processes:* Coll. of Problems with Solutions. 2nd Ed. Moscow, MISiS [in Russian].
24. Grigorenko, G.M., Pomarin, Yu.M. (1989) Hydrogen and nitrogen in metals during plasma melting. Kyiv, Naukova Dumka [in Russian].

ORCID

V.O. Shapovalov: 0000-0003-1339-3088,
V.G. Mogylatenko: 0000-0002-6550-2058,
R.V. Lyutyi: 0000-0001-6655-6499,
R.V. Kozin: 0000-0002-8501-0827

CONFLICT OF INTEREST

The Authors declare no conflict of interest

CORRESPONDING AUTHOR

V.G. Mogylatenko
E.O. Paton Electric Welding Institute of the NASU
11 Kazymyr Malevych Str., 03150, Kyiv, Ukraine.
E-mail: vmogilatenko@gmail.com

SUGGESTED CITATION

V.O. Shapovalov, V.G. Mogylatenko,
R.V. Lyutyi, R.V. Kozin (2024) Nitrogen absorption by 04Cr18Ni10 steel in plasma-arc melting under slag of CaO–Al_2O_3 system. *The Paton Welding J*., **1**, 43–50.

JOURNAL HOME PAGE

https://patonpublishinghouse.com/eng/journals/tpwj

Received: 31.08.2023
Received in revised form: 18.10.2023
Accepted: 15.01.2024

DOI: https://doi.org/10.37434/tpwj2024.01.08

NONDESTRUCTIVE METHOD OF RESIDUAL STRESS DETERMINATION IN WELDED JOINTS BASED ON APPLICATION OF HIGH-DENSITY CURRENT PULSES AND SPECKLE-INTERFEROMETRY

L.M. Lobanov, V.V. Savitsky, O.P. Shutkevych, K.V. Shyian, I.V. Kyianets

E.O. Paton Electric Welding Institute of the NASU
11 Kazymyr Malevych Str., 03150, Kyiv, Ukraine

ABSTRACT

A procedure was developed for nondestructive evaluation of residual stresses in welded joints based on application of high-density current pulses and laser speckle-interferometry. Comparison of the results of residual stress measurement in welded joints, obtained by the developed method and by hole-drilling method, was performed.

KEYWORDS: residual stresses, welded joints, high-density current pulse, speckle-interferometry, electroplastic effect, hole-drilling method

INTRODUCTION

One of the important tasks in manufacturing, designing and operation of welded structures is testing their stressed state, since residual stresses significantly affect the life of structures. To determine residual stresses, such nondestructive methods as X-ray, ultrasonic, magnetic, etc., and mechanical ones based on the principle of stress relaxation are widespread [1–3]. During determination of residual stresses in elements and assemblies of structures for their elastic unloading, different methods are used, such as thermal effect [4], plastic ball indentation [5], hole drilling, etc. The method of drilling small non-through holes (with a diameter of 1.0–3.0 mm and a depth of 0.5–3.0 mm) became the most widespread for elastic unloading of residual stresses. Measurements of deformations and displacements around the zone of elastic unloading (around the drilled hole) are performed using different methods of experimental mechanics, as for example, electric strain gauging, mechanical strain gauges and optical methods, including laser interferometry methods [6–13].

However, despite the widespread use of the hole drilling method, it is still destructive. This imposes a number of restrictions on its application. For example, the method has limited use in the diagnostics of real structures in the process of their operation. In this regard, the determination of residual stresses is often performed on individual mock-ups of elements and assemblies of real structures. Therefore, the development and creation of nondestructive methods for elastic unloading of residual stresses of full-scale structures is a relevant task.

The aim of this study is to create a nondestructive method for residual stress determination, which has high accuracy and reliability inherent in destructive relaxation methods. For this aim, it is proposed to replace the process of drilling holes for stress relaxation, which violates the structural surface integrity, with a nondestructive method of local stress relaxation based on the use of high density current pulses of 10^7–10^{10} A/m^2 (Figure 1) [14–16]. It is believed that upon introduction of a current pulse, a zone with a hemispherical appearance is formed, in which an electroplastic effect arises and stress relaxation around the place of pulse introduction occurs. At the same time, the integrity of the tested area of the material is not violated. Since the size of the area, in which the stress relaxation occurs is unknown in advance and depends on the electrode system parameters, it is necessary to evaluate the effectiveness of residual stress relaxation upon the introduction of a current pulse.

PULSE CURRENT SOURCE

A pulse current source (PCS) was created at the Institute of Electrodynamics of NASU, and two types of shock-pulse and pulse effect electrode systems were developed at the PWI of NASU, which are used to introduce a pulse current into the studied area of the ob-

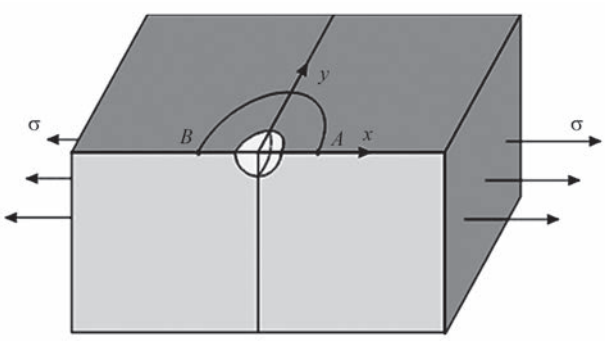

Figure 1. Scheme of residual stress relaxation after introduction of a current pulse

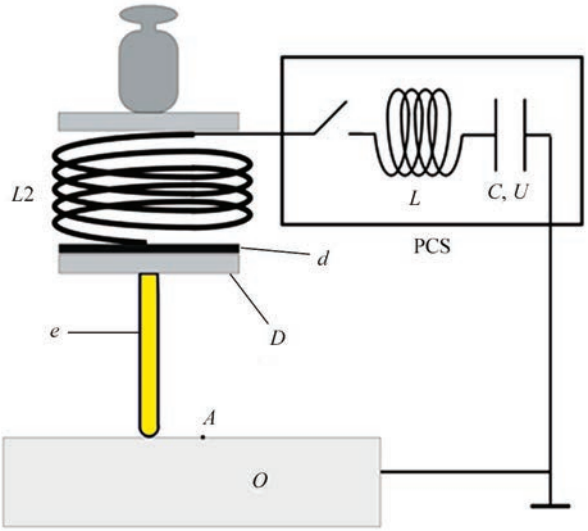

Figure 2. Scheme of the electrode system with a shock-pulse type of action: *L* — inductance coil; *C* — capacitor battery with a charging voltage *U*; *e* — electrode; *D* — disc; *O* — object into which a current pulse is introduced; *d* — dielectric gasket; PCS — pulse current source

ject. The power source has wide capabilities for regulation of the basic electrical parameters of the system, which provide the required shape of current pulses.

The electrode system of a pulse action includes electrode *e*, load *P*, which ensures the necessary contact between the electrode and the point of current introduction and the pulse current source (Figure 2). In the electrode system of pulse action, the inductance *L* of the coil varies in the range of 4700–1900 μH, the capacity *C* of the capacitor battery is 3400–17000 μF, the charging voltage is 50–186 V.

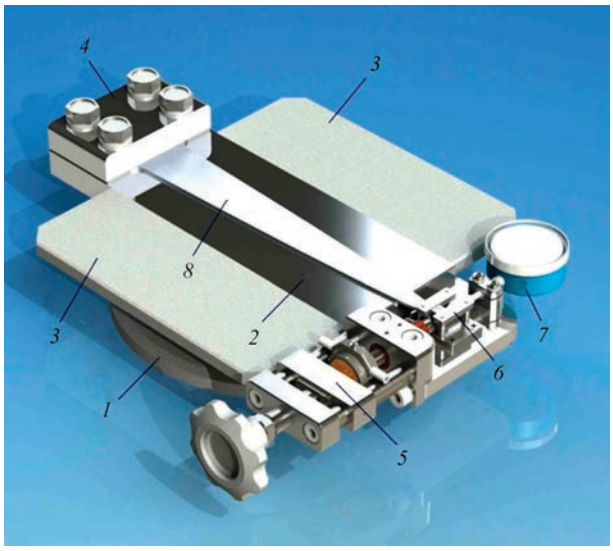

Figure 3. Device for loading test specimens: *1* — round plate, on which a base plate is placed for positioning specimen on the device; *2* — polished plate, on which test specimen is located; *3* — plate for placing speckle-interferometer; *4* — clamping element for fixing test specimen; *5*, *6* — units for loading test specimen; *7* — device for testing beam (test specimen) displacements; *8* — beam of equal bending resistance (test specimen)

The created electrode system provides introduction of a pulsed current into the studied material, the effect of which leads to arising displacements around the point of introduction. The values of displacements depend on the stress state at the point of pulse introduction, as well as on such parameters of the electrode system as charging voltage on the capacitor storage *U*, inductance *L*, etc. In order to determine the effective parameters of the electrode system, it is necessary to assess the degree of stress relaxation upon introduction of a current pulse into the tested area of the studied element.

INFLUENCE OF THE ELECTRODE SYSTEM PARAMETERS ON STRESS RELAXATION

To determine the influence of the electrode system parameters on stress relaxation, a mechanical device for loading test specimens was designed and manufactured (Figures 3, 4). A beam of equal bending resistance is used as a test specimen, as far as stresses in all cross-sections will not exceed the preset ones.

The speckle-interferometry device designed at the PWI [11–13] allows registering displacements of surface points in the range of 0.03–3 μm. Figure 5 presents patterns of interference fringes, that contain information about the displacements u_x obtained after the introduction of a local current pulse into the test specimen under loading (Figure 4). The interference patterns show that with an increase in the values of stresses σ_{xx}, the disturbance area around the point of pulse introduction also grows.

A current pulse was introduced into the area of the specimen being tested at the points n_i with the level of stresses σ_{xx} from –100 to 100 MPa (Figure 4). As a result of the local stress relaxation in the vicinity of the point of pulse introduction, displacements appeared, which were registered by the noncontact method of electron speckle-interferometry.

Figure 6 shows a diagram of dependence of the displacements u_x on the specified stresses σ_{xx}. This diagram shows that the measured displacements u_x at the points *A*, located at a distance of 1.25 mm from the place of the current pulse introduction (Figure 1), depend linearly on the stress state at the place of measurements.

However, the use of data on the displacements only at a point *A* is insufficient for calculating stresses σ_{xx} in real structures, since displacements will also arise at these points due to the action of stresses σ_{xx}.

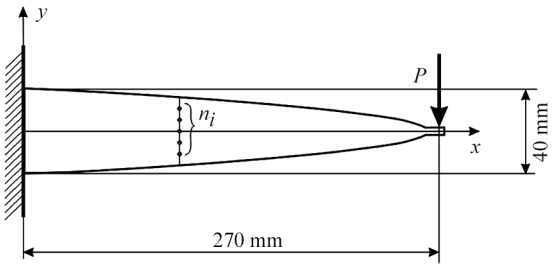

Figure 4. Scheme of specimen with equal bending resistance: n_i — points where a current pulse was introduced

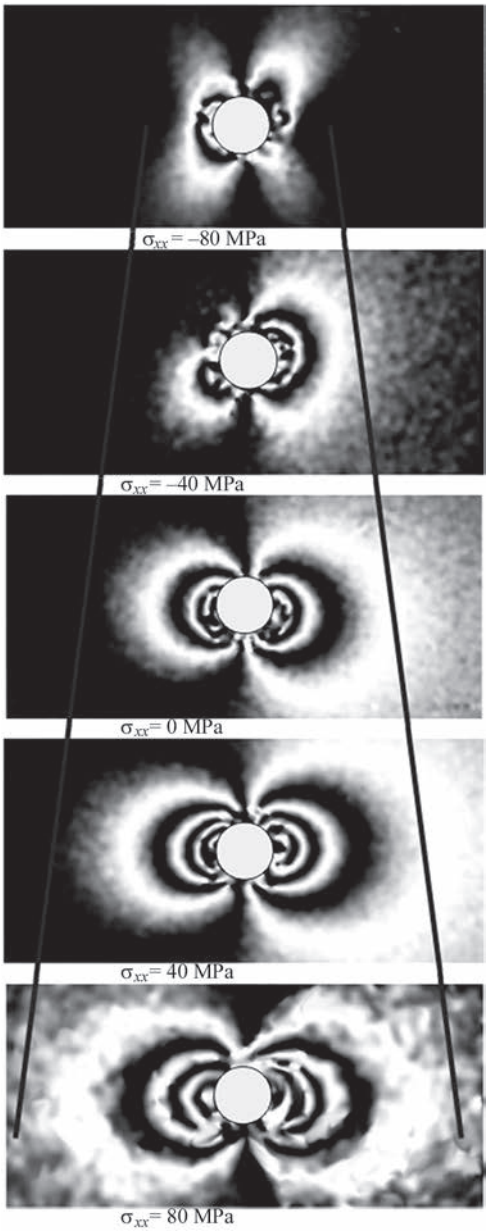

Figure 5. Interference patterns obtained after the introduction of a current pulse in the areas with a residual stress level. Electrode system parameters: L = 3.26 μH, U = 150 V, s = 0.5 mm. The lines indicate an increase in the zone of stress relaxation effect on the displacements with an increase in the stress state

Therefore, it is necessary to introduce a new parameter, that depends linearly on residual stresses and displacements and does not depend on the location of the main coordinate axes and the type of stress state.

NUMERICAL CALCULATIONS

We assume that upon the current pulse introduction, stress relaxation occurs in the region with the axis of *OZ* symmetry, as when drilling a hole. In this case, the dependence of the displacements u_r and u_θ, arising as a result of unloading the stresses σ_{xx}, σ_{yy} and σ_{xy} on the angle θ at some distance from the center of the hole r in polar coordinates, is expressed by the following formulas [11–13, 17]:

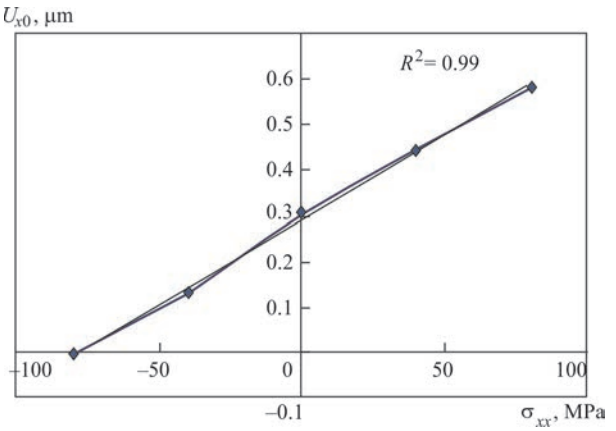

Figure 6. Dependence of displacements u_{x0} measured by the method of electron speckle-interferometry at a distance of 1.25 mm from the point of introduction of a high-density current pulse, on the level of specified stresses σ_{xx} (value of the approximation probability R^2 = 0.99)

$$u_r(r,\theta) = A\sigma_{xx} + B\sigma_{xx}\cos 2\theta; \quad (1)$$

$$u_\theta(r,\theta) = C\sigma_{xx}\sin 2\theta, \quad (2)$$

where the coefficients A, B and C depend on the boundary conditions, sizes of stress relaxation area, etc.

Considering that upon the introduction of a current pulse, complete stress relaxation does not occur, and also an initial effect (displacements arise after the introduction of a current pulse in a material without stresses) takes place, we introduce the following notations:

$$\sigma_{xx}^{im} = b_{xx} + k\sigma_{xx}; \quad (3)$$

$$\sigma_{yy}^{im} = b_{yy} + k_{yy}\sigma_{yy}; \quad (4)$$

$$\tau_{xy}^{im} = k_{xy} + \tau_{xy}, \quad (5)$$

where b_{xx}, b_{yy} i k_{xx}, k_{yy}, k_{xy} are the constants that characterize, respectively, the initial effect and the degree of stress relaxation compared to the drilled hole with a diameter and depth of 1 mm.

For a plane stressed state, using the principle of stress superposition and axisymmetric problem, after transforming the equations (1)–(2), we obtain:

$$u_r(r,\theta) = A(\sigma_{xx}^{im} + \sigma_{yy}^{im}) + \\ + B\left[(\sigma_{xx}^{im} - \sigma_{yy}^{im})\cos 2\theta + 2\tau_{xy}^{im}\sin 2\theta\right]; \quad (6)$$

$$u_\theta(r,\theta) = C\left[(\sigma_{xx}^{im} - \sigma_{yy}^{im})\sin 2\theta - 2\tau_{xy}^{im}\cos 2\theta\right]. \quad (7)$$

An important advantage of the electron speckle-interferometry method in registering displacements is the possibility of simultaneous determination of displacements in a large number of points. This makes it possible to obtain data on the displacements u_x at points located around a circle with a radius r with the center at the place of the current pulse introduction (Figure 7).

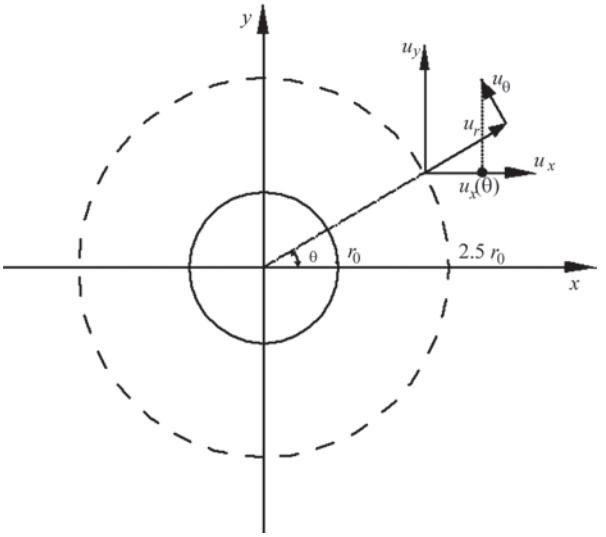

Figure 7. Scheme of displacement measurement in the vicinity of the point (place) of introduction of a high-density current pulse

As a result of preliminary studies, it was established that with the introduction of a current pulse when using different parameters of the electrode system, an electrode imprint with a diameter of 0.4–1.0 mm appears on the object. Therefore, the minimum radius of the circle is selected, in which the ratio "speckle pattern quality – displacement value" is optimal. It is known that when measuring displacements in the vicinity of a drilled hole by the method of electron speckle interferometry, it is optimal to use the distance r, which is equal to 2.5 of the hole radius r_0. Therefore, in the further studies, data on displacements at points located on a circle with a radius of 1.25 mm were used.

To simplify the calculations from the equations (6) and (7), let us separate the multiplier components $F(\theta)$, $G(\theta)$ and $H(\theta)$ before σ_{xx}^{im}, σ_{yy}^{im} and τ_{xy}^{im}, which depend on the angle θ and the coefficients A, B and C, we obtain the following dependence:

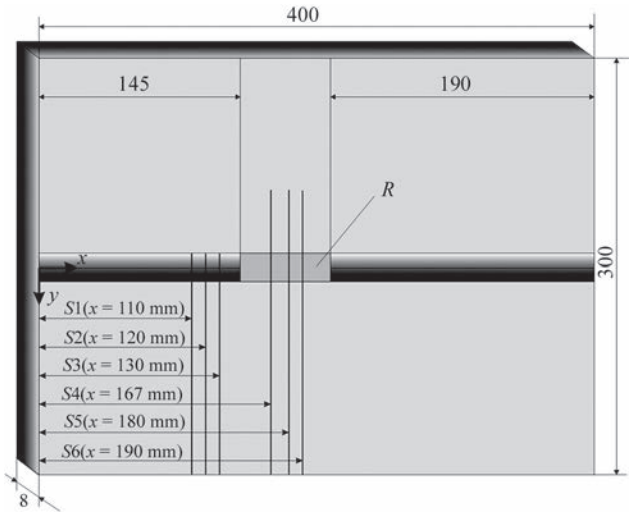

Figure 8. Scheme of welded specimen from AMg5 alloy: *S*1–*S*6 — sections, in which residual stresses were determined; *R* — area, in which the weld reinforcement was removed

$$u_x(r,\theta) = u_r(r,\theta)\cos\theta - u_\theta(r,\theta)\sin\theta; \quad (8)$$

$$u_x(\theta)\big|_\tau = 1.25\ \text{mm} = F(\theta)\sigma_{xx}^{im} + G(\theta)\sigma_{yy}^{im} + H(\theta)\tau_{xy}^{im}. \quad (9)$$

Measuring their displacements u_x at the points of the circle (more than three points) allows calculating the values σ_{xx}^{im}, σ_{yy}^{im} and τ_{xy}^{im} by the method of least squares using a system of equations:

$$\begin{bmatrix} F(\theta_1) & G(\theta_1) & H(\theta_1) \\ F(\theta_2) & G(\theta_2) & H(\theta_2) \\ F(\theta_3) & G(\theta_3) & H(\theta_3) \end{bmatrix} \begin{Bmatrix} \sigma_{xx}^{im} \\ \sigma_{yy}^{im} \\ \tau_{xy}^{im} \end{Bmatrix} = \begin{Bmatrix} u_x(\theta_1) \\ u_x(\theta_2) \\ u_x(\theta_3) \end{Bmatrix}. \quad (10)$$

In order to evaluate the possibility of applying the proposed algorithm and using σ_{xx}^{im}, σ_{yy}^{im} and τ_{xy}^{im} in determination of residual stresses, let us build the diagram of dependence of σ_{xx}^{im} on the specified stress state σ_{xx} on the basis of the data on their displacements u_x presented in Figure 6. As in the case of the data on the displacements u_x (Figure 6), the dependence between σ_{xx}^{im} and σ_{xx} has a linear character (value of the approximation probability $R^2 = 0.99$). This diagram is characterized by the angle of inclination relative to the *OX* axis, as well as by the value at the point with zero stresses. From the diagram, it is possible to determine the values k_{xx} and b_{xx}, which correspond to the set parameters of the electrode system, and calculate the value of residual stresses at the point of the current pulse introduction by the formula (3).

Thus, in order to determine residual stresses in full-scale objects, it is necessary to perform preliminary calibration of the electrode system on the test specimen in order to obtain the dependence of σ_{xx}^{im} on σ_{xx} (3). To do this, stresses σ_{xx} are specified on a beam of equal bending resistance and a current pulse is introduced in the observation area of the speckle-interferometer. Based on the data obtained by the speckle-interferometry method on displacements of the surface points after the introduction of a current pulse into the metal being under the effect of mechanical stresses, the value σ_{xx}^{im} is calculated from the system

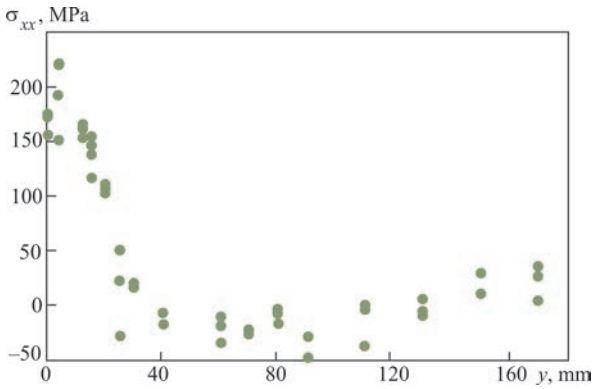

Figure 9. Results of residual stress determination by the method of electron speckle-interferometry based on the use of high-density current pulses for their relaxation

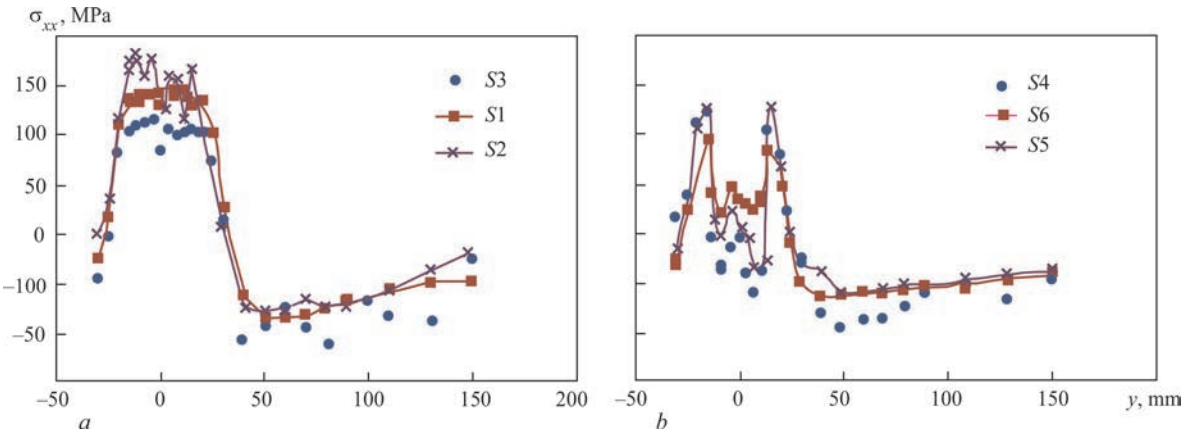

Figure 10. Distribution of stresses σ_{xx} passing through the weld reinforcement in the sections *S*1–*S*3 (*a*) and after its removal in the sections *S*4–*S*6 (*b*)

of linear equations (10). Based on the data of certain values σ_{xx}^{im} at five points, a diagram of dependence of σ_{xx}^{im} on σ_{xx} is constructed, according to which the values k_{xx} and b_{xx} corresponding to the parameters of this electrode system are determined.

Therefore, using the value σ_{xx}^{im} calculated on the basis of the data on the displacements registered by the method of electron speckle-interferometry, and the values k_{xx} and b_{xx} determined from the diagram and by the formula (3), it is possible to determine the stress state at the point of the current pulse introduction.

The use of functions σ_{xx}^{im}, σ_{yy}^{im} and τ_{xy}^{im} is better compared to the data on the displacements u_x at the points *A* and *B* (Figure 1), because in this case the use of information about the displacements u_x at the points along the entire length of the circle reduces the relative error and increases the reliability of determination of residual stresses.

EXPERIMENTAL STUDIES

With the help of the developed technology, the residual stresses in butt-welded joints of AMg5 alloy were determined based on the use of high-density current pulses. The results of stress measurements obtained using current pulses were compared with the data obtained with the use of the equipment of the PWI based on the use of the hole drilling method in combination with speckle-interferometry. The effectiveness and accuracy of residual stress measurement with this device is confirmed by the results of the Round Robin test, which was conducted by the International Institute of Welding [18, 19]. Figure 8 shows a diagram of the welded specimen with the specified cross-sections, along which measurements were made.

Figure 9 shows the results of residual stress determination using high-density current pulses along the section *S*3. In the experiment, data on the displacements were registered after the introduction of current pulses at the points located at the same distance from the center of the weld. The diagram shows that there is a scatter of the obtained experimental data and, therefore, to increase the accuracy of stress determination, it is suggested to use stress values averaged over three points.

Stresses were determined by two methods in the sections passing both through the weld reinforcement (*S*1, *S*2 and *S*3) as well as after its removal (*S*4, *S*5 and *S*6) (Figure 8). The results of residual stress determination obtained based on the use of the pulse method (sections *S*3 and *S*4) were compared with the data obtained by the method of drilling holes with a diameter and depth of 1.0 mm, respectively (sections *S*1 and *S*6) and 0.5 mm (sections *S*2 and *S*5) (Figure 10).

It is important that the results of stress determination in the area of the weld and the near-weld zone using the created nondestructive method are significantly closer to the data obtained by the hole drilling method (drilling holes with a diameter and depth of 0.5 mm), and differ from the data obtained when using holes with a diameter and depth of 1.0 mm (Figure 10.) This indicates that in the welded specimen there is a stress gradient over the thickness of the plates.

The stress curves show the coincidence of the results of residual stress determination obtained by the proposed approach and the hole drilling method, which indicates that the developed nondestructive method for residual stress determination based on the use of high-density current pulses for their relaxation allows obtaining reliable data on the distribution of stresses along the selected section, at the same time not violating the integrity of the studied material. The maximum deviation of the results of stress determination by the nondestructive method compared to the hole drilling method (drilled holes with a diameter of 0.5 mm) does not exceed 20 MPa.

CONCLUSIONS

A new nondestructive method for residual stress determination in welded joints has been developed, which is based on the use of high-density current pulses for local stress relaxation and subsequent registration of displacements by the laser speckle-interferometry method. It is shown that as a result of the introduc-

tion of current pulses, a partial relaxation of residual stresses occurs, and the value of measured displacements depends on the level of stresses at the place of pulse introduction. It was experimentally confirmed that the developed method allows determining residual stresses with an error of up to 20 MPa compared to the destructive method of drilling holes.

The proposed approach allows determination of residual stresses directly on real structures during their operation, without violating the material integrity. This opens up wide prospects to use the method for monitoring the stress-strain state of critical welded assemblies and structures in the power, aircraft and space rocket industries, shipbuilding, etc. The use of the proposed approach will increase the reliability and safety of the operation of technical objects due to the timely detection and elimination of dangerous stresses.

REFERENCES

1. Kandil, F.A., Lord J.D., Fry, A.T., Grant P.V. (2001) *A review of residual stress measurement methods a guide to technique selection.* National Physical Laboratory, Teddington Middlesex, TWll OLW, UK.
2. Vasudevan, M., Shanmugasundaram, P., Baksha Arivazhagan et al. (2014) Nondestructive assessment of residual stresses and distortion in austenitic stainless steel weld joints. *Materials Evaluation*, 72(**12**), 1509–1518.
3. Lasseigne, A.N., Olson, D.L. (2008) Development of nondestructive techniques for characterization of residual stresses in advanced materials. *Materials Evaluation*, 66(**10**), 1077–1083.
4. Robinson, A.F., Dulieu-Barton, Quinn S., R.L., Burguete, J.M. (2009) A review of residual stress analysis using thermoelastic techniques. *J. of Physics: Conference Series*, **181**, 012029. DOI: https://doi.org/0.1088/1742- 6596/181/1/012029
5. Hernandez, L.C., Ponce, L., Fundora, A. et al. (2012) Residual stress mapping in TiN coatings by nanoindentation technique. *Materials Evaluation*, 70(**11**), 1320–1325.
6. ASTM E837-20: *Standard test method for determining residual stresses by the hole-drilling strain-gages*. https://www.astm.org/e0837-20.html
7. (2010) *Measurement of residual stresses by the hole drilling strain gage method.* Technical Note TN- 503-6, Revision: 01-Nov-2010, Vishay Micro Measurements, Pennsylvania.
8. Makino, A., Nelson, D. (1994) Residual-stress determination by single-axis holographic interferometry and hole-drilling — Pt I. *Theory. Exp. Mech.*, **34**, 66–78. DOI: https://doi.org/10.1007/BF02328443
9. Viotti, M.R., Kapp, W., Albertazzi, Jr.A. (2009) Achromatic digital speckle pattern interferometer with constant radial in-plane sensitivity by using a diffractive optical element. *Applied Optics*, 48(**12**), 2275–2281. DOI: https://opg.optica.org/ao/abstract.cfm?URI=ao-48-12-2275
10. Schajer, G.S. (1981) Application of finite element calculations to residual stress measurements. *J. of Engineering Materials and Technology*, 103(**2**), 157–163. DOI: https://doi.org/10.1115/1.3224988
11. Lobanov, L.M., Pivtorak, V.A., Savitsky, V.V. et al. (2005) Express control of quality and stressed state of welded structures using methods of electron shearography and speckle-interferometry. *The Paton Welding J.*, **8**, 35–40.
12. Lobanov, L., Pivtorak, V., Savitsky, V., Tkachuk, G. (2013) Technology and equipment for determination of residual stresses in welded structures based on the application of electron speckle-interferometry. *Mat. Sci. Forum*, **768–769**, 166–173. DOI: https://doi.org/10.4028/www.scientific. net/MSF.768-769.166
13. Lobanov, L.M., Pivtorak, V.A., Savitsky, V.V., Tkachuk, G.I. (2006) Procedure for determination of residual stresses in welded joints and structural elements using electron speckle-interferometry. *The Paton Welding J.*, **1**, 24–29.
14. Lobanov, L.M., Pashchin, N.A., Loginov, V.P., Loginova Yu.V. (2005) Application of electric pulse treatment of structural elements to extend their service life. *The Paton Welding J.*, **11**, 19–23.
15. Stepanov, G.V., Babutsky, A.I., Mameev, I.A. (2004) Nonstationary stress-strain state in long rod produced by pulses of high-density electric current. *Problemy Prochnosti,* **4**, 60–67 [in Russian].
16. Lobanov, L.M., Pashchin, N.A., Mikhodui, O.L. (2012) Efficiency of electrodynamic treatment of welded joints of AMg6 alloy of different thickness. *The Paton Welding J.*, **3**, 6–10.
17. Timoshenko, S.P. (1972) *Course of theory of elasticity*. Kyiv, Naukova Dumka [in Russian].
18. Wohlfahrt, H., Dilger, K. (2008) *New results of the IIW Round Robin residual stress measurements*. Report on the experimental Round Robin Tests on residual stresses 2008, IIW Doc. XIII-2241-08/XV-1283-08.
19. Wohlfahrt, H., Nitschke-Pagel, T., Dilger, K. et al. (2012) Residual stress calculations and measurements — review and assessment of the IIW Round Robin results. *Weld World*, 56(**9–10**), 120–140. DOI: https://doi.org/10.1007/BF03321387

ORCID

L.M. Lobanov: 0000-0001-9296-2335,
V.V. Savitsky: 0000-0002-2615-1793,
O.P. Shutkevych: 0000-0001-5758-2396,
K.V. Shyian: 0000-0001-9198-6554,
I.V. Kyianets: 0000-0002-2559-8200

CONFLICT OF INTEREST

The Authors declare no conflict of interest

CORRESPONDING AUTHOR

O.P. Shutkevych
E.O. Paton Electric Welding Institute of the NASU
11 Kazymyr Malevych Str., 03150, Kyiv, Ukraine.
E-mail: shutkevich1996@gmail.com

SUGGESTED CITATION

L.M. Lobanov, V.V. Savitsky, O.P. Shutkevych, K.V. Shyian, I.V. Kyianets (2024) Nondestructive method of residual stress determination in welded joints based on application of high-density current pulses and speckle-interferometry. *The Paton Welding J.*, **1**, 51–56.

JOURNAL HOME PAGE

https://patonpublishinghouse.com/eng/journals/tpwj

Received: 04.10.2023
Received in revised form: 11.12.2023
Accepted: 25.01.2024